

SANDIA REPORT

SAND2004-4778

Unlimited Release

Printed September 2004

A Robust, Coupled Approach for Atomistic-Continuum Simulation

S. Aubry, D.J. Bammann, J.J. Hoyt, R.E. Jones, C.J. Kimmer,
P.A. Klein, G.J. Wagner, E.B. Webb III, J.A. Zimmerman

Prepared by Sandia National Laboratories
Albuquerque, New Mexico 87185 and Livermore, California 94550

Sandia is a multiprogram laboratory operated by Sandia Corporation,
a Lockheed Martin Company, for the United States Department of Energy's
National Nuclear Security Administration under Contract DE-AC04-94AL85000.

Approved for public release; further dissemination unlimited.



Issued by Sandia National Laboratories, operated for the United States Department of Energy by Sandia Corporation.

NOTICE: This report was prepared as an account of work sponsored by an agency of the United States Government. Neither the United States Government, nor any agency thereof, nor any of their employees, nor any of their contractors, subcontractors, or their employees, make any warranty, express or implied, or assume any legal liability or responsibility for the accuracy, completeness, or usefulness of any information, apparatus, product, or process disclosed, or represent that its use would not infringe privately owned rights. Reference herein to any specific commercial product, process, or service by trade name, trademark, manufacturer, or otherwise, does not necessarily constitute or imply its endorsement, recommendation, or favoring by the United States Government, any agency thereof, or any of their contractors or subcontractors. The views and opinions expressed herein do not necessarily state or reflect those of the United States Government, any agency thereof, or any of their contractors.

Printed in the United States of America. This report has been reproduced directly from the best available copy.

Available to DOE and DOE contractors from

U.S. Department of Energy
Office of Scientific and Technical Information
P.O. Box 62
Oak Ridge, TN 37831

Telephone: (865)576-8401
Facsimile: (865)576-5728
E-Mail: reports@adonis.osti.gov
Online ordering: <http://www.osti.gov/bridge>

Available to the public from

U.S. Department of Commerce
National Technical Information Service
5285 Port Royal Rd
Springfield, VA 22161

Telephone: (800)553-6847
Facsimile: (703)605-6900
E-Mail: orders@ntis.fedworld.gov
Online order: <http://www.ntis.gov/help/ordermethods.asp?loc=7-4-0#online>



SAND2004-4778
Unlimited Release
Printed September 2004

A Robust, Coupled Approach for Atomistic-Continuum Simulation

S. Aubry[†] D.J. Bammann[†] J.J. Hoyt[‡] R.E. Jones[†] C.J. Kimmer[†]
P.A. Klein[†] G.J. Wagner* E.B. Webb III[‡] J.A. Zimmerman[†]

[†]Science-Based Materials Modeling Department

*Fluid and Thermal Science Department

Sandia National Laboratories

P.O. Box 969

Livermore, CA 94551

[‡]Materials & Process Modeling Department

Sandia National Laboratories

P.O. Box 5800

Albuquerque, NM 87158

Abstract

This report is a collection of documents written by the group members of the Engineering Sciences Research Foundation (ESRF), Laboratory Directed Research and Development (LDRD) project titled “A Robust, Coupled Approach to Atomistic-Continuum Simulation”. Presented in this document is the development of a formulation for performing quasistatic, coupled, atomistic-continuum simulation that includes cross terms in the equilibrium equations that arise due to kinematic coupling and corrections used for the calculation of system potential energy to account for continuum elements that overlap regions containing atomic bonds, evaluations of thermo-mechanical continuum quantities calculated within atomistic simulations including measures of stress, temperature and heat flux, calculation used to determine the appropriate spatial and time averaging necessary to enable these atomistically-defined expressions to have the same physical meaning as their continuum counterparts, and a formulation to quantify a continuum “temperature field”, the first step towards constructing a coupled atomistic-continuum approach capable of finite temperature and dynamic analyses.

Keywords: atomistic simulation; continuum mechanics; stress; temperature; thermal transport; coupling .

This page intentionally left blank.

Contents

1	Introduction	15
2	Coupled, Atomistic-Continuum Simulation using Arbitrary Overlapping Domains	19
2.1	Introduction	19
2.2	Kinematics of quasistatic coupling	23
2.3	Coupled equilibrium equations	27
2.4	Projection using moving least squares	29
2.5	Correction to the Cauchy-Born rule in the overlap region	33
2.6	Implications of the overlap correction	42
2.7	One-dimensional examples	43
2.8	Two-dimensional examples	47
2.9	Three-dimensional examples	50
2.10	Summary	53
3	Evaluation of Stress in Atomistic Simulation	57
3.1	Introduction	57

3.2	Hardy's Formalism for Atomistic-Continuum Equivalence	60
3.3	Results and Discussion	63
3.3.1	Stress in a crystal at zero temperature	63
3.3.2	Stress in a crystal at finite temperature	66
3.3.3	Stress in a crystal with a free surface	69
3.4	Conclusions and Discussion	70
3.5	Appendix: Invariance of Atomic Bond Energies	72
4	Statistical Mechanics and Multiscale Processes	73
4.1	Equilibrium Statistical Mechanics	74
4.1.1	Overview of Phase Space and Ensembles	74
4.1.2	Statistical Mechanics of a Harmonic Crystal	77
4.2	Nonequilibrium Statistical Mechanics	80
4.2.1	Overview	80
4.2.2	Ensemble Equations of Motion	81
4.2.3	Microscopic balance laws and hydrodynamics	83
4.2.4	Linear Response	86
4.2.5	Local Equilibrium	87
4.2.6	Extended Irreversible Thermodynamics	89
4.2.7	Kinetic Theory	90
4.3	Relevance to the Coupling Problem	90
4.3.1	Numerical Examples	95

4.4	Conclusions	103
5	Models of Heat Transfer	105
5.1	The Physics of Heat Transfer	105
5.2	Models of Heat Transfer	107
5.2.1	The Boltzmann Transport Equation	107
5.2.2	The Maxwell-Cattaneo Equation	109
5.2.3	Fourier's Law	110
5.3	Conclusions	110
6	Evaluation of Temperature and Heat in Atomistic Simulation	113
6.1	Introduction	113
6.2	Hardy's Formalism Revisited	114
6.3	Equilibrium Temperature Simulations	116
6.4	Transient and Steady-State Heat Flow Simulations	117
6.5	Conclusions	124
6.6	Appendix: Constant Heat Flux Algorithm	124
7	Thermo-mechanical Coupling of Atomistic and Continuum Systems	127
7.1	The Continuum Initial-Boundary Value Problem	127
7.1.1	Examples	130
7.2	The Atomistic Initial-Boundary Value Problem	132
7.3	Coupling Molecular Dynamics with Continuum Finite Elements	133

7.4	A Model Problem	134
7.5	Coarse-graining and fine-scale energy	136
8	Publications	141
9	Distribution	151

List of Figures

2.1	Patch of a coupled atomistic-continuum system. The set of finite element nodes \mathcal{N} is shown as open squares \square . The set of nodes $\hat{\mathcal{N}}$ is shown as solid squares \blacksquare . The set of atoms \mathcal{A} is shown as open circles \circ , and the set of atoms $\hat{\mathcal{A}}$ is shown as solid circles \bullet	24
2.2	Bond between atoms near element boundaries.	37
2.3	The support of node $a \in \tilde{\mathcal{N}}_{(i)}$	38
2.4	Patch from a one-dimensional coupled system.	44
2.5	Homogeneous displacements of the 1-dimensional coupled system for both the corrected bond density of $\rho(X) = \frac{3}{4}$ and the uncorrected bond density of $\rho(X) = 1$. Atom and element numbers are given within the figure by the digit shown above or below, respectively, the corresponding part.	45
2.6	Displacements of a coupled system using a diagonal approximation in the L_2 projection.	46
2.7	$\rho_{(i)}(\mathbf{X})$ for a 1-D atomic chain using a 5 th nearest neighbor Lennard-Jones potential.	47
2.8	Displacements for the relaxation of a free, 1-D atomic chain using a 5 th nearest neighbor Lennard-Jones potential. Each curve represents a different number of layers of free atoms used at the chain's surfaces. The ratio of element size to atomic spacing is (a) 2:1 and (b) 6:1.	48

2.9	(a) The 2-dimensional coupled system consisting of a rectangular mesh of square elements and a portion of a hexagonal lattice. Atoms are colored according to whether they are free (red) or ghost (green and blue). (b) The 2-d system homogeneously stretched in the horizontal direction. Color denotes the magnitude of stretch from zero (blue) to the highest value (red).	49
2.10	(a) A 2-D, hexagonal lattice with free surfaces composed of free (green) and ghost (blue) atoms. The overlapping square FE mesh is shown in red. (b) The relaxed configuraton of (a) for the coupled system (red) and a system treated purely with atomistics (green). Displacements are magnified by a factor of 200.	50
2.11	(a) A 2-D, hexagonal lattice with free surfaces composed of free (green) and ghost (blue) atoms. The overlapping triangular FE mesh is shown in red. (b) The relaxed configuraton of (a) for the coupled system (red) and a system treated purely with atomistics (green). Displacements are magnified by a factor of 200.	51
2.12	One-half of a 3-D cube modeled with (a) pure atomistics, (b) coupled atomistics-continuum using a hexahedral element mesh, and (c) coupled atomistics-continuum using a tetrahedral element mesh. Displacements are magnified by a factor of 200.	52
2.13	Hydrostatic stress for nodes along a line passing through the middle of the relaxed cube. The legend refers to the number of layers of free atoms used for the outer surface of the crystal.	53
2.14	The same curves as in Figure 2.13 for a system coupled only through kinematics and use of the Cauchy-Born rule (no force coupling mechanisms used).	54
3.1	Virial and Hardy stress for an atomic system at zero temperature and pressure.	63
3.2	Hardy stresses within a Cu crystal at zero temperature and pressure. Spatial position is varied across 2.5 unit cells of lattice parameter equal to 3.615 Å. .	64
3.3	Mean of the Hardy stress averaged over many spatial points.	65
3.4	Virial and Hardy stress for an atomic system at zero temperature and 2% uniaxial strain.	66

3.5	Virial and Hardy stress for an atomic system at 300 K temperature at (a) zero pressure and (b) 2% uniaxial strain. The heavy horizontal line in (b) is the system value of stress as determined from the virial theorem. Two sets of lines are shown for each stress to signify the two spatial points, A and B. . .	67
3.6	Hardy stress for an atomic system at 300 K temperature at (a) zero pressure and (b) 2% uniaxial strain. The dotted horizontal line in (b) is the system value of stress as determined from the virial theorem. Each point plotted is actually the value of stress averaged over 1, 10, 100 or 1000 MD time steps ($\Delta t = 2$ fs), as denoted by the legend.	68
3.7	Virial and Hardy stress for an atomic system at zero temperature and pressure with a free surface. The dashed line denotes the position of the top layer of atoms while the solid line denotes the effective position of the free surface of the crystal. (a), (b) The normal stress for the direction perpendicular to the free surface for $R_c = 6, 10 \text{ \AA}$. (c),(d) The normal stress for directions parallel to the free surface for $R_c = 6, 10 \text{ \AA}$	69
4.1	Schematic of the system used to evaluate the statistics of coarse-grained quantities. The atoms are black points while the finite-element nodes and edges are in blue. The axes are in units of the lattice constant a , and periodic, stress-free boundary conditions are applied in all three coordinate directions. The actual system dimensions were $8 \times 8 \times 8a$, $a = 3.63 \text{ \AA}$ with a varying element size l_{FE}	96
4.2	The nodal fluctuations $\delta \bar{\mathbf{u}}_i^2(t)$ calculated as averages over the time interval dt . Although all values of dt shown here reproduce the average $\langle \delta \bar{\mathbf{u}}_i^2 \rangle$ acceptably, computing a nodal quantity over a longer time interval produces a more smoothly varying quantity. To obtain a nodal quantity that is temporally this smooth, the averaging time is over a minimum of 1000 MD timesteps—considerably larger than the FE to MD timestep ratio that could be used in a coupled simulation.	97
4.3	Time-averaged nodal displacement fluctuations $\sqrt{\langle \delta \bar{\mathbf{u}}_i^2(t) \rangle}$ plotted against $1/\sqrt{N_s}$. The dotted line shows a linear least-squares fit.	98
4.4	The nodal temperature $\langle T_i \rangle$ plotted against element size l_{FE} . For the largest elements, virtually all of the thermal vibrations are included in the nodal temperature which approaches the atomic temperature 300K.	98

4.5	The N_s -dependence of the nodal temperature fluctuations $\sqrt{\langle \delta T_i^2 \rangle}$. The different values of l_{FE} with the same N_s also illustrate the stronger dependence on l_{FE} at small l_{FE}	99
4.6	Schematic geometry for the nonequilibrium system. A uniform temperature gradient of 100 K is established between the cold end (blue) and the hot end (red). The axes are in units of $a = 3.63 \text{ \AA}$ while the actual system used was $40 \times 8 \times 8a$. The finite element connectivity is demonstrated by the colored edges. Cubes of side l_{FE} are placed along the x direction, and the number of elements in the overlaid finite-element system depends on l_{FE} since the MD system size is fixed.	100
4.7	The time-averaged nodal temperature $\langle T_i \rangle$ for a smaller sampling interval. The time-averages are computed by sampling every 2 fs for a total time interval of 500 fs—two orders of magnitude smaller than those in the other plots. This small interval is clearly inadequate to resolve ∇T . For comparison, the time-averaged temperature $\langle T_\alpha \rangle$ computed from all atoms is also shown. . .	100
4.8	The fine scale fluctuations $\langle \delta(\mathbf{u}'_i)^2 \rangle$ for a smaller sampling interval.	101
4.9	The time-averaged nodal temperature $\langle T_i \rangle$ for a larger sampling interval. Compare to Fig. 4.7. Although the smallest element sizes consistently underestimate the temperature, they do generally get ∇T correct.	101
4.10	The coarse-scale fluctuations $\langle \delta \bar{\mathbf{u}}_i^2 \rangle$ decrease with increasing l_{FE} . Except for boundary effects attributable to the constant heat flux boundary conditions, they are independent of the local temperature along the strip.	102
4.11	Nodal projection of the fine scale fluctuations for different element sizes reveals that they may be used as a temperature measure in this steady-state simulation. This is essentially a computation of a coarse-grained Debye-Waller factor for the system as a function of the local temperature along the length of the system.	103
6.1	Average atomic temperature for an NVT ensemble as a function of analysis volume radius. Curves are shown for averaging times of 0.1 ps (dashed), 1 ps (dotted) and 5 ps (solid).	116
6.2	Hardy (solid curve) and atomic (broken) temperature as a function of sampling time for an NVT ensemble equilibrated to 300 K. The analysis volume is of size $R_c = 10 \text{ \AA}$	117

6.3	Temperature (T) as a function of length along the simulation cell. Data are shown at 10, 50, and 200 ps into the simulation. A least squares fit to the data at 200 ps is shown as the black line.	118
6.4	Temperature (T) as a function of time for constant heat flux simulations. The curves show T in successive analysis regions going from the heat injection region (top) to the heat extraction region (bottom). Vertical lines correspond to times at which T gradient data are presented in Figure 6.3	118
6.5	Hardy temperature (in units of K) for a random selection of spatial points. Frames correspond to the simulation times shown over which the transient heat flow evolves to steady-state.	119
6.6	Distribution of temperature (in units of K) for binned regions along the length of the crystal shown in Figure 6.5. Each frame is labeled with the corresponding simulation time, and the black curve denotes the instantaneous distribution while the red curve denotes a time average of the distribution over a period of the 40 ps leading up to the time shown.	120
6.7	Distribution of heat flux component q_x (in units of $\text{nW}/\text{\AA}^2$) for binned regions along the length of the crystal shown in Figure 6.5. Each frame is labeled with the corresponding simulation time, and the black curve denotes the instantaneous distribution while the red curve denotes a time average of the distribution over a period of the 40 ps leading up to the time shown. . .	121
6.8	Distribution of heat flux component q_y (in units of $\text{nW}/\text{\AA}^2$) for binned regions along the length of the crystal shown in Figure 6.5. Each frame is labeled with the corresponding simulation time, and the black curve denotes the instantaneous distribution while the red curve denotes a time average of the distribution over a period of the 40 ps leading up to the time shown. . .	122
6.9	Heat flux (\mathbf{q}) given by the standard atomistic expression as a function of time for constant heat flux simulations. The curves show \mathbf{q} in the x (solid), y (dashed), and z (dotted) directions within one analysis bin used in Figure 6.7. A horizontal solid line shows the expectation value for q_x for the system. . .	123
7.1	Generic dispersion curves for MD and FE	133
7.2	Empirical Temperature versus Kinetic Temperature	135



This page intentionally left blank.

Chapter 1

Introduction

Principle Author: J.A. Zimmerman

This report is a collection of documents written by the group members of the Engineering Sciences Research Foundation (ESRF), Laboratory Directed Research and Development (LDRD) project titled “A Robust, Coupled Approach to Atomistic-Continuum Simulation”. With the growing focus on predictive modeling and simulation, Sandia must develop the capability to model deformation and failure in multiple scale settings. This project’s goal was to develop a robust approach for coupled atomistic-continuum simulation, thereby constructing methodologies for both quasistatic and finite temperature/dynamic analyses. The plan for this project evolved into efforts by sub-groups in the following areas:

- Improve the fidelity of a coupled approach for quasistatic analysis by including cross terms in the equilibrium equations that arise due to kinematic coupling and by correcting the contributions to the potential energy of the system so that no double counting of energy occurs by the inclusion of both atomic bond energies and continuum strain energies.
- Investigate and evaluate expressions found in the literature for calculating continuum variables such as stress, temperature and heat flux within atomistic simulation. Determine the appropriate spatial and time averaging necessary to enable these expressions to have the same physical meaning as their continuum counterparts.
- Combine the advancements achieved in these two areas to formulate a coupled atomistic-continuum approach capable of performing finite temperature and dynamic analyses. This formulation would necessarily include additional variables to quantify a continuum “temperature field”, and energy would be properly transferred from vibrations in the atomistic region to the separate modes of a scalar temperature field and long elastic waves in the continuum.

Although further verification work exists, we have successfully accomplished the first two tasks listed above. A formulation for a quasistatic, coupled approach has been developed and verified through comparison of simulations of homogeneous deformation and inhomogeneous surface relaxation with pure atomistic systems. This work is documented in Chapter 2, which has been written as a journal-ready publication to be submitted before the conclusion of the 2004 fiscal year. In addition, this work was recently presented as a proceedings paper at the 2004 Mesomechanics conference held in June of 2004 in Patras, Greece [1].

With regard to defining and evaluating definitions for continuum quantities that can be evaluated locally within an atomistic region, much of the background research in this area was accomplished in the first two years of the project's life. During the course of the 2002 fiscal year, several articles pertaining to definitions of stress were reviewed, and the key ones were identified and summarized via internal documents. By the conclusion of the 2002 calendar year, these documents were collected and published as a SAND report [2]. One of the key products of this background research was the identification and preliminary evaluation of the formulation by R.J. Hardy. Hardy's approach was unique in the fact that it permits the analyst to designate a characteristic size on the atomic scale to be used to define a continuum material point. The choice of this characteristic size enables one to "fine tune" the degree of smoothness that the calculated stress field will possess, and for specific selections, Hardy's expressions degenerate into other expressions presented within the literature. More advanced evaluation of Hardy's expression for stress, and a comparison with volume averages of the standard expression used by atomistic simulation practitioners is provided in Chapter 3, and was previously presented in both a proceedings paper for the 2nd MIT Conference on Computational Fluid and Solid Mechanics held in Cambridge, Massachusetts in June of 2003 [3] and in a recent special issue of *Modelling and Simulation in Materials Science and Engineering* [4]. Hardy's formulation also includes the derivation of an expression to calculate heat flux in an atomistic simulation. In addition, Hardy has separately put forth an expression for calculating a scalar temperature field. Both of these expressions are reviewed and evaluated in Chapter 6, which was presented in-part as a proceedings paper at the 2004 Mesomechanics conference held in June of 2004 in Patras, Greece [5]. The work discussed in this chapter has been instrumental in determining minimum spatial and time averaging limits necessary to properly transfer energy and information from the atomistic to the continuum.

Chapter 4 reviews concepts relevant to equilibrium and non-equilibrium statistical mechanics. A thorough understanding of these concepts was necessary to analyze the thermo-mechanical behavior of atomic crystals with regard to fundamental balance equations and variables used within continuum mechanics. Chapter 5 then goes on to review the essential elements regarding heat transport in materials via phonons. For most conventional atomistic simulation methods, phonons are the sole means by which energy is transferred between particles in a dynamic fashion; most techniques do not include contributions to energy transport due to the movement of electrons as the electrons themselves are not explicitly modeled. It will

be important to quantify how heat transport occurs within atomistic systems, under both transient and steady-state conditions (examined in some detail in Chapter 6), in order to construct the constitutive model for the continuum which has been coupled to that atomistic system. Some of the rudimentary ideas developed by the group will be presented in Chapter 7, including an expression for a continuum temperature field that is derived by projecting the fine-scale portion of the atomic kinetic energies onto the coarse-scale grid of the overlapping continuum.

This page intentionally left blank.

Chapter 2

Coupled, Atomistic-Continuum Simulation using Arbitrary Overlapping Domains

Principle Authors: P.A. Klein and J.A. Zimmerman

We present a formulation for coupling atomistic and continuum simulation methods for quasistatic analysis. In our formulation, a coarse-scale continuum discretization is assumed to cover all parts of the computational domain with atomistic crystals introduced only in regions of interest. The geometry of the discretization and crystal are allowed to overlap arbitrarily. Our approach uses interpolation and projection operators to link the kinematics of each region, which are then used to formulate a system potential energy from which we derive coupled equilibrium equations. A hyperelastic constitutive formulation is used to compute the stress response of the defect-free continuum with constitutive properties derived from the Cauchy-Born rule. A correction to the Cauchy-Born rule is introduced in the overlap region to minimize fictitious boundary effects. Features of our approach will be demonstrated with simulations in 1, 2 and 3 dimensions.

2.1 Introduction

The primary objective of modern materials modeling is to predict the material response and failure governed by deformation mechanisms, and to assess the mechanical reliability of components. These material deformation mechanisms operate at specific length scales, which vary from nanometers to microns. Multi-scale materials simulations have been the focus of many studies [6] using techniques such as atomistic simulation, phase-field calculations, and finite element (FE) analysis. Continuum mechanical modeling efforts have evolved beyond

using ad-hoc failure criteria to include cohesive approaches for surface separation and damage accumulation models for bulk material degradation. However, these techniques only capture anticipated deformation phenomena. Atomistic simulation procedures, such as molecular statics (MS) and dynamics (MD), use simple interatomic potentials as the underlying constitutive relation between material particles and allow the derived forces to govern the basic physics of the system's response to an applied load. These potentials use parameters fitted from ab-initio calculations and physical measurements of material properties. Atomistic simulation uses the smallest length scale intrinsic to all materials, that of crystal lattice spacing, and has the ability to display competing mechanisms of material deformation, such as fracture, dislocation nucleation and propagation, and void nucleation, growth and coalescence. However, limits of computational power prohibit analysis of micro-scale systems using only atomistic simulation, even in large-scale, parallel calculations. Methods to circumvent this size limitation also introduce fictitious boundary effects in simulations that degrade the fidelity of the results.

It is clear that some coupled methodology must be established to combine the strengths of both atomistic and continuum modeling. Although this field has acquired a substantial history, it remains an active area of research. Early work by Kohlhoff and collaborators [7, 8] created a methodology that combined finite element analysis with atomistic modeling, named FEAt. The FEAt model uses an atomic lattice surrounded by an FE mesh with a limited overlap region that enforces boundary conditions on both atomistic and continuum domains. Consistency is achieved by requiring the strains in the overlap region to be equal for both the atoms and the continuum, and by matching the elastic constants of the continuum constitutive model to those derived from the governing interatomic potential. In [8], non-linear elasticity is used via a Taylor series expansion of elastic energy about strain that contains first, second and third order elastic constants. The FEAt model works well for static simulations, but displays some anomalous behavior for dynamics. However, it has the inherent disadvantage that the FE mesh within the overlap region must be refined so that nodal spacing is at the atomic scale with node position dictated by the crystal lattice structure.

More recently, several methods have been introduced that attempt to improve upon the original efforts by Kohlhoff *et al.* These include the Quasicontinuum (QC) method by Tadmor, Ortiz and Phillips [9], Coarse-Grained Molecular Dynamics (CGMD) by Rudd and Broughton [10], Molecular-Atomistic-Ab Initio Dynamics (MAAD) by Broughton, Abraham, Bernstein and Kaxiras [11], and the Bridging Scale Decomposition (BSD) by Wagner and Liu [12]. The QC method uses an FE representation of the displacement field over the entire domain, requiring mesh refinement to the atomic scale in regions of severe deformation. The strain energy within an element is determined from a single representative atom embedded in a locally constructed crystallite. At lower levels of deformation, elements may be much larger than the atomistic length scale, and the lattice is assumed to deform homogeneously as described by the continuum deformation gradient. Deformation of increasing severity triggers

mesh refinement until the element size is reduced to the atomic scale. Under these conditions, the local crystallite spans multiple elements, leading to a non-local calculation of the strain energy. Consistency between refined and coarse areas is achieved by using finite deformation elasticity [13] and the Cauchy-Born rule [14, 15] that equates interatomic bond energy to continuum potential energy in order to develop a non-linear continuum constitutive model based on the interatomic potential used for atomistic simulation. While the QC approach allows a blending between atomistic and continuum regions, it possesses the disadvantages of a reliance on adaptive mesh refinement to the atomic scale, a computationally intensive task, and an inability to eliminate fictitious boundary effects at the local/non-local boundary.

Coarse-Grained Molecular Dynamics consists of replacing the underlying atomic lattice with nodes representing either individual atoms or a weighted average collection of atoms. The total energy of the system is calculated from the potential and kinetic energies of the nodes plus a thermal energy term for the missing degrees of freedom assumed to be at a uniform temperature. CGMD produces phonon spectra with wavelength dependencies similar to those for pure atomistics; however, CGMD does possess wavelength-dependent limitations on energy transmission. Newer versions of CGMD include implementation of a Generalized Langevin equation (GLE) to dissipate high frequency motions not representable in the coarser-scaled regions [16] and development of CGMD is ongoing.

More similar to Kohlkoff *et al.*'s methodology, the MAAD approach separates the physical system into distinct MD and FE regions. The system's total Hamiltonian consists of contributions from each individual region as well as a contribution from "hand-shaking" between regions. The FE mesh in this hand-shaking zone is refined to the atomic scale and nodes occupy positions that atoms would occupy if the atomic region was extended into the FE domain. Kinetic energy is attributed to both nodes and atoms in the hand-shaking zone, while away from this zone uniform temperature terms are added for the missing degrees of freedom, just as for CGMD. MAAD has successfully exhibited smooth and non-reflective transmission of elastic waves between MD and FE regions, but it does suffer from the same limitations as CGMD. At the hand-shaking zone, kinetic motion of atoms is transferred into dynamic motion of nodes. While this allows temperature to be represented as motion in the continuum region, nodes, unlike atoms, have no physical meaning and are introduced only as part of the numerical discretization. The deformation solution should be independent of nodal positions, which is certainly not the case for atomistic simulation and atomic positions.

Most recently, Wagner and Liu [12] have developed the Bridging Scale Decomposition approach for doing both static and dynamic atomistic-continuum coupling. Their approach uses a continuous FE mesh for the entire domain with smaller regions of atoms placed in regions where high fidelity modeling is needed. Atomistic simulation, either MS or MD, is performed in the usual manner and the FE displacement solution for the overlying mesh is determined from projection of the atomic displacements using FE shape functions. This projection is known as the "bridging scale"; it is the portion of the atomistic simulation

solution that must be subtracted from the total in order to separate the displacements into a coarse scale, resolvable onto the FE mesh, and a fine scale. For the FE domain that does not contain underlying atoms, the FE solution is solved for in the usual manner. Coupling between the two regions is accomplished by the expressions for forces on atoms and nodes and by using “ghost” atoms that interact with free atoms at the atomic-FE boundary and whose displacements are determined by interpolation of the FE displacement field. For dynamic problems, Wagner and Liu have minimized reflections at the atomic-FE boundary by using GLEs to account for the effect of the missing fine scale degrees of freedom in the isolated FE mesh. Park *et al.* [17] have extended the BSD method to 2-dimensional systems by numerically computing the resulting impedance force that needs to be eliminated in order to represent the missing fine scale degrees of freedom. They have used this extension to simulate elastic wave propagation and dynamic crack growth. The BSD approach possesses many advantages; however, neither [12] nor [17] specify how to partition potential energy consistently in the overlapping elements that are defined by both free and projected nodes and contain bonds between free and ghost atoms. This partitioning is the crucial factor in minimizing fictitious forces within the overlap region, as will be shown.

The coupling methods listed above have been used successfully to simulate materials deformation such as crack-grain boundary interactions, dislocation nucleation from nanoindentation and the dynamic fracture of silicon. However, the weaknesses of these methods show that more consideration is needed in developing a coupled atomistic-continuum approach. Specifically, methods such as FEAt, MAAD and BSD do not provide a rigorous treatment on how to partition potential energy between atomistic bonds and continuum strain energy within the overlap regions. The MAAD methodology overlaps atomistics and continuum within an extremely small region, and arbitrarily combines $\frac{1}{2}$ of the energy from the atomic bonds and $\frac{1}{2}$ of the continuum strain energy to arrive at the full Hamiltonian for the coupled system. For the BSD approach, the overlap region is wider and uses the mechanism of ghost atoms; however, ghosts are introduced in an ad-hoc manner and the existence of ghosts is not included in the equilibrium equations. In addition, the authors do not specify either how to count bonds between free and ghost atoms or how the density of such bonds should affect contribution of strain energy within overlapping elements. The problem of proper partitioning of potential energy terms has largely been overlooked, and is often simplified in many overlaying grid methodologies such as the bridging domain method by Xiao and Belytschko [18]. In that article, the authors analyzed coupling for a 1-dimensional chain and used a simple ratio of distance from a point to the boundary of the continuum region over the total projected length of the atomic/continuum overlap region to scale the atomistic and continuum contributions to the system energy from material within the overlap region. It was found that this simple ratio is insufficient to eliminate spurious wave reflection in 2-dimensional systems, and was then modified in an ad-hoc manner. The issue of how to partition energy within an atomistic-continuum overlap region clearly needs to be properly addressed in order to maintain the integrity of the two views of material deformation, atomistic and continuum. Our goal for this work is to develop a formulation that preserves the

integrity of the MS and FE methods for separate regions, but adapt each method to partition potential energy consistently in the overlap region.

In this paper, we describe this formulation and the implementation of an atomistic-to-finite element coupling method for quasistatic analysis. The formulation assumes a finite element mesh covers all parts of the computational domain, while regions of interest in the domain are also covered with an atomistic crystal. This approach was selected because it allows the domain covered by the crystal to be changed by adding or removing atoms while not requiring any changes to the finite element mesh. A hyperelastic formulation is used to compute the stress response of the continuum using a Cauchy-Born constitutive model, which can be shown to reproduce the response of the crystal exactly for the case of an infinite, defect-free crystal subject to homogeneous deformations. For the quasistatic case, the coupling approach is essentially concerned with coupling the displacement fields, with additional issues arising to avoid fictitious boundary effects for both the atomistic and continuum regions and to account for overlap between the continuum and underlying crystal. This overlap is treated by the inclusion of specific cross terms that naturally appear in the equilibrium equations, and by the use of a correction to the Cauchy-Born rule for elements within the overlap region. Our approach will be validated through examination of homogeneous deformation and free surface relaxation in 1, 2, and 3 dimensional crystals .

2.2 Kinematics of quasistatic coupling

Consider a coupled atomistic-continuum system as shown in Figure 2.1. It is assumed that a finite element mesh covers all parts of the computational domain, while only limited regions of interest are also covered with an atomic crystal. For example, such a region may be the volume of material immediately surrounding a crack tip, or the material at the free surface of a solid that will be mechanically loaded by a nanoindenter. Let the atomistic displacements in the system be written as

$$\check{\mathbf{Q}} = [\mathbf{q}^{(\alpha)}, \mathbf{q}^{(\beta)}, \dots, \mathbf{q}^{(\gamma)}]^T \quad \alpha, \beta, \dots, \gamma \in \check{\mathcal{A}}, \quad (2.1)$$

where $\mathbf{q}^{(\alpha)}$ is the displacement of atom (α) and $\check{\mathcal{A}}$ is the set of all atoms. Likewise, let the nodal displacements be written as

$$\check{\mathbf{U}} = [\mathbf{u}^{(a)}, \mathbf{u}^{(b)}, \dots, \mathbf{u}^{(c)}]^T \quad a, b, \dots, c \in \check{\mathcal{N}}, \quad (2.2)$$

where $\mathbf{u}^{(a)}$ is the displacement of node (a) and $\check{\mathcal{N}}$ is the set of all finite element nodes. In this paper, lower case Greek symbols are used for atom indices, while lower case Roman symbols are used for node indices. In order to satisfy boundary conditions for both regions, the motion of some of the atoms is prescribed by the continuum displacement field. This

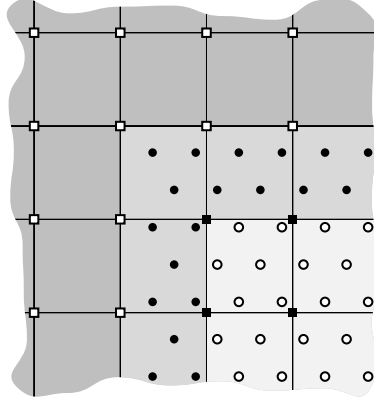


Figure 2.1: Patch of a coupled atomistic-continuum system. The set of finite element nodes \mathcal{N} is shown as open squares \square . The set of nodes $\check{\mathcal{N}}$ is shown as solid squares \blacksquare . The set of atoms \mathcal{A} is shown as open circles \circ , and the set of atoms $\hat{\mathcal{A}}$ is shown as solid circles \bullet .

subset of atomistic displacements is denoted by

$$\hat{\mathbf{Q}} = [\mathbf{q}^{(\alpha)}, \mathbf{q}^{(\beta)}, \dots, \mathbf{q}^{(\gamma)}]^T \quad \alpha, \beta, \dots, \gamma \in \hat{\mathcal{A}}, \quad (2.3)$$

while the complement which contains the unprescribed atomistic displacements is denoted by

$$\mathbf{Q} = [\mathbf{q}^{(\delta)}, \mathbf{q}^{(\epsilon)}, \dots, \mathbf{q}^{(\eta)}]^T \quad \delta, \epsilon, \dots, \eta \in \mathcal{A}, \quad (2.4)$$

where

$$\hat{\mathcal{A}} \cup \mathcal{A} = \check{\mathcal{A}} \quad \text{and} \quad \hat{\mathcal{A}} \cap \mathcal{A} = \emptyset. \quad (2.5)$$

Similar to the BSD approach found in [12], atoms that belong to the set $\hat{\mathcal{A}}$ are sometimes referred to as ghost atoms, while atoms that belong to the set \mathcal{A} are sometimes referred to as free atoms. Analogously, the motion of some finite element nodes is prescribed by the underlying lattice. These displacements are denoted by

$$\hat{\mathbf{U}} = [\mathbf{u}^{(a)}, \mathbf{u}^{(b)}, \dots, \mathbf{u}^{(c)}]^T \quad a, b, \dots, c \in \hat{\mathcal{N}}, \quad (2.6)$$

while the unprescribed nodal displacements are denoted by

$$\mathbf{U} = [\mathbf{u}^{(m)}, \mathbf{u}^{(n)}, \dots, \mathbf{u}^{(s)}]^T \quad m, n, \dots, s \in \mathcal{N}, \quad (2.7)$$

where likewise

$$\hat{\mathcal{N}} \cup \mathcal{N} = \check{\mathcal{N}} \quad \text{and} \quad \hat{\mathcal{N}} \cap \mathcal{N} = \emptyset. \quad (2.8)$$

One can interpolate the continuum displacement field to the location of any atom as

$$\mathbf{u}(\mathbf{X}^{(\alpha)}) = \sum_{a \in \check{\mathcal{N}}} N^{(a)}(\mathbf{X}^{(\alpha)}) \mathbf{u}^{(a)}, \quad (2.9)$$

where $\mathbf{X}^{(\alpha)}$ is the undeformed position of atom (α) and $N^{(a)}$ is the finite element shape function associated with node (a). The finite element shape functions typically have compact support, so the sum in (2.9) involves only the nodes whose support includes $\mathbf{X}^{(\alpha)}$. Generally, one can consider the atomistic and continuum displacement fields to be related as

$$\begin{Bmatrix} \mathbf{Q} \\ \hat{\mathbf{Q}} \end{Bmatrix} = \mathbf{N} \begin{Bmatrix} \mathbf{U} \\ \hat{\mathbf{U}} \end{Bmatrix} + \begin{Bmatrix} \mathbf{Q}' \\ 0 \end{Bmatrix}, \quad (2.10)$$

where

$$\mathbf{N} = \begin{bmatrix} \mathbf{N}_{\mathbf{Q}\mathbf{U}} & \mathbf{N}_{\mathbf{Q}\hat{\mathbf{U}}} \\ \mathbf{N}_{\hat{\mathbf{Q}}\mathbf{U}} & \mathbf{N}_{\hat{\mathbf{Q}}\hat{\mathbf{U}}} \end{bmatrix}. \quad (2.11)$$

The sub-matrices of \mathbf{N} contain shape functions as defined by the interpolation given in (2.9). By definition,

$$\mathbf{N}_{\mathbf{Q}\mathbf{U}} = 0, \quad (2.12)$$

since \mathbf{Q} and \mathbf{U} are independent. The component of the atomistic displacements

$$\mathbf{Q}' = [\mathbf{q}'^{(\alpha)}, \mathbf{q}'^{(\beta)}, \dots, \mathbf{q}'^{(\gamma)}]^T \quad \alpha \in \mathcal{A}, \quad (2.13)$$

where $\mathbf{q}'^{(\alpha)} = \mathbf{q}^{(\alpha)} - \bar{\mathbf{q}}^{(\alpha)}$ for $\alpha \in \mathcal{A}$ and

$$\bar{\mathbf{q}}^{(\alpha)} = \sum_{a \in \hat{\mathcal{N}}} N^{(a)}(\mathbf{X}^{(\alpha)}) \mathbf{u}^{(a)} \quad \alpha \in \mathcal{A}, \quad (2.14)$$

is introduced since the finite element shape functions in $\mathbf{N}_{\mathbf{Q}\hat{\mathbf{U}}}$ are generally too coarse to represent the atomistic displacements exactly. It will be the convention in this paper to display the portion of any quantity \mathbf{S} that can be represented at a coarse scale using the finite element shape functions with the overbar symbol, $\bar{\mathbf{S}}$, while any portion of \mathbf{S} that cannot be represented by the finite element shape functions is deemed “fine scale” and is displayed using the accent symbol, \mathbf{S}' . This is similar to the convention used in [12]. Indeed, much of the kinematic description presented thus far closely resembles the BSD methodology as given in [12]. However, in this paper the symbols \mathbf{Q} and \mathbf{q} strictly refer to the displacements of atoms and the symbol \mathbf{U} only refers to the displacements of finite element nodes. The symbol \mathbf{u} refers to the continuum displacement field as dictated by the finite element solution. It can be evaluated at points that coincide with atoms $\mathbf{u}(\mathbf{X}^{(\alpha)})$, nodes $\mathbf{u}^{(a)}$, or any point contained within the finite element mesh $\mathbf{u}(\mathbf{X})$.

Since \mathbf{Q} and $\hat{\mathbf{U}}$ may have arbitrary dimensions, where we expect the number of atoms represented in \mathbf{Q} to be larger than the number of finite elements nodes represented in $\hat{\mathbf{U}}$, $\mathbf{N}_{\hat{\mathbf{Q}}\hat{\mathbf{U}}}^{-1}$ will not be defined, and so the prescribed nodal displacements $\hat{\mathbf{U}}$ are chosen to minimize the error

$$e = \mathbf{Q}' \cdot \mathbf{Q}' = \sum_{\alpha \in \mathcal{A}} \left[\mathbf{q}^{(\alpha)} - \sum_{a \in \hat{\mathcal{N}}} N^{(a)}(\mathbf{X}^{(\alpha)}) \mathbf{u}^{(a)} \right]^2. \quad (2.15)$$

The nodal displacements $\mathbf{u}^{(a)}$ for $a \in \hat{\mathcal{N}}$ are determined by solving

$$\sum_{\alpha \in \mathcal{A}} \mathbf{q}^{(\alpha)} N^{(b)}(\mathbf{X}^{(\alpha)}) = \sum_{\alpha \in \mathcal{A}} \sum_{a \in \hat{\mathcal{N}}} N^{(a)}(\mathbf{X}^{(\alpha)}) \mathbf{u}^{(a)} N^{(b)}(\mathbf{X}^{(\alpha)}) \quad b \in \hat{\mathcal{N}}, \quad (2.16)$$

which is the discretized L_2 projection of the atomistic displacements onto the finite element space containing $N^{(a)}$ for $a \in \hat{\mathcal{N}}$ using the atomistic positions $\mathbf{X}^{(\alpha)}$ for $\alpha \in \mathcal{A}$ as integration points. Here, the fine scale part of atomistic displacements \mathbf{Q}' is used only as an error estimation, and can be used to guide the addition or removal of atoms from the crystal. In the work by Wagner and Liu [12], this fine scale part is used in conjunction with a bridging scale formulation to develop a method for dynamic coupling.

The solution to (2.16) can be expressed in matrix notation by first rewriting (2.15) as

$$e = \left[\mathbf{Q} - \mathbf{N}_{\mathbf{Q}\hat{\mathbf{U}}} \hat{\mathbf{U}} \right] \cdot \left[\mathbf{Q} - \mathbf{N}_{\mathbf{Q}\hat{\mathbf{U}}} \hat{\mathbf{U}} \right], \quad (2.17)$$

which is minimized for

$$\hat{\mathbf{U}} = \mathbf{M}_{\hat{\mathbf{U}}\hat{\mathbf{U}}}^{-1} \mathbf{N}_{\mathbf{Q}\hat{\mathbf{U}}}^T \mathbf{Q}, \quad (2.18)$$

where

$$\mathbf{M}_{\hat{\mathbf{U}}\hat{\mathbf{U}}} = \mathbf{N}_{\mathbf{Q}\hat{\mathbf{U}}}^T \mathbf{N}_{\mathbf{Q}\hat{\mathbf{U}}}. \quad (2.19)$$

From (2.10) and (2.18), we can express the prescribed atomistic displacements entirely in terms of the free atomistic and nodal displacements as

$$\hat{\mathbf{Q}} = \mathbf{N}_{\mathbf{Q}\mathbf{U}} \mathbf{U} + \mathbf{N}_{\mathbf{Q}\hat{\mathbf{U}}} \mathbf{M}_{\hat{\mathbf{U}}\hat{\mathbf{U}}}^{-1} \mathbf{N}_{\mathbf{Q}\hat{\mathbf{U}}}^T \mathbf{Q}, \quad (2.20)$$

which shows the prescribed atomistic displacements depend not only on the displacements of the free finite element nodes, but also on the displacements of the free atoms through the projection of those displacements onto the overlapping part of the finite element mesh.

Note that $\mathbf{M}_{\hat{\mathbf{U}}\hat{\mathbf{U}}}$ has the structure (although not the dimensional units) of the finite element mass matrix, evaluated using the atomistic coordinates as integration points. Immediately, we recognize that this matrix will be rank deficient if an insufficient number of atoms lie in the support of every node $A \in \hat{\mathcal{N}}$. This number of atoms will depend on the element topology. One can propose conditions for the stability of the projection. First, it is necessary there be at least as many atoms in \mathcal{A} as there are nodes in $\hat{\mathcal{N}}$; however, this is not sufficient to insure the stability of the projection. The number of atoms in the supports of the nodes in $\hat{\mathcal{N}}$ can be considered on an element-by-element basis. For instance, the mass matrix for a bilinear quad requires four integration points to avoid rank deficiency, a sufficient but not necessary condition to avoid rank deficiency of the assembled matrix. Combined, the necessary and sufficient conditions ensure the stability of the projection. The cost of the projection can be reduced by using a diagonal, or ‘‘lumped’’, approximation to the mass matrix. With this projection matrix, the nodal displacements will not be optimal

for minimizing the error (2.15), so less of the atomistic displacement information will be transferred to the nodes and more will remain as error. Moreover, the lumped approximation does not allow linearly varying fields to be projected explicitly, a condition that will be required in the subsequent formulation.

2.3 Coupled equilibrium equations

Equations (2.18) and (2.20) provide us the means to express the displacements of both projected nodes $\hat{\mathbf{U}}$ and interpolated atoms $\hat{\mathbf{Q}}$ as functions of the unprescribed atomic \mathbf{Q} and nodal \mathbf{U} displacements. To solve for these unprescribed displacements, we must develop equilibrium equations that are derived by formulating the total potential energy of the entire coupled atomistic-continuum system. We express the potential energy of the coupled system as

$$\Pi(\mathbf{Q}, \mathbf{U}) = \Pi_{\mathbf{Q}} + \Pi_{\mathbf{U}} - \mathbf{F}_{\mathbf{Q}} \cdot \mathbf{Q} - \mathbf{F}_{\mathbf{U}} \cdot \mathbf{U}, \quad (2.21)$$

where $\Pi_{\mathbf{Q}}$ represents the potential energy in the bonds of the crystal, $\Pi_{\mathbf{U}}$ is the strain energy density integrated over the continuum, and $\mathbf{F}_{\mathbf{Q}}$ and $\mathbf{F}_{\mathbf{U}}$ are external forces acting on the atoms and finite element nodes, respectively. To include the structure of the coupling between the atomistic and continuum displacement fields from (2.18) and (2.20), we rewrite the contributions to the total potential as

$$\Pi_{\mathbf{Q}} = \Pi_{\mathbf{Q}}(\mathbf{Q}, \mathbf{U}) = \Pi_{\mathbf{Q}}\left(\mathbf{Q}, \hat{\mathbf{Q}}(\mathbf{Q}, \mathbf{U})\right), \quad (2.22)$$

$$\Pi_{\mathbf{U}} = \Pi_{\mathbf{U}}(\mathbf{Q}, \mathbf{U}) = \Pi_{\mathbf{U}}\left(\mathbf{U}, \hat{\mathbf{U}}(\mathbf{Q})\right). \quad (2.23)$$

Incorporating the coupling relationships directly in the total potential insures that the coupled system will also remain conservative if a hyperelastic formulation is used for calculating the continuum response. The equations of static equilibrium are derived from total potential as

$$\mathbf{R}_{\mathbf{Q}} = \frac{\partial \Pi_{\mathbf{Q}}}{\partial \mathbf{Q}} + \frac{\partial \Pi_{\mathbf{Q}}}{\partial \hat{\mathbf{Q}}} \frac{\partial \hat{\mathbf{Q}}}{\partial \mathbf{Q}} + \frac{\partial \Pi_{\mathbf{U}}}{\partial \hat{\mathbf{U}}} \frac{\partial \hat{\mathbf{U}}}{\partial \mathbf{Q}} - \mathbf{F}_{\mathbf{Q}} = 0, \quad (2.24)$$

$$\mathbf{R}_{\mathbf{U}} = \frac{\partial \Pi_{\mathbf{U}}}{\partial \mathbf{U}} + \frac{\partial \Pi_{\mathbf{Q}}}{\partial \hat{\mathbf{Q}}} \frac{\partial \hat{\mathbf{Q}}}{\partial \mathbf{U}} - \mathbf{F}_{\mathbf{U}} = 0. \quad (2.25)$$

Using (2.18) and (2.20), the equilibrium equations can be expressed as

$$\mathbf{R}_{\mathbf{Q}} = \frac{\partial \Pi_{\mathbf{Q}}}{\partial \mathbf{Q}} + \mathbf{R}_{\hat{\mathbf{U}}\mathbf{N}_{\mathbf{Q}\hat{\mathbf{U}}}}^{\mathbf{T}} - \mathbf{F}_{\mathbf{Q}} = 0, \quad (2.26)$$

$$\mathbf{R}_{\mathbf{U}} = \frac{\partial \Pi_{\mathbf{U}}}{\partial \mathbf{U}} + \frac{\partial \Pi_{\mathbf{Q}}}{\partial \hat{\mathbf{Q}}} \mathbf{N}_{\hat{\mathbf{Q}}\mathbf{U}} - \mathbf{F}_{\mathbf{U}} = 0, \quad (2.27)$$

where

$$\mathbf{R}_{\hat{\mathbf{U}}} = \left[\frac{\partial \Pi_{\mathbf{U}}}{\partial \hat{\mathbf{U}}} + \frac{\partial \Pi_{\mathbf{Q}}}{\partial \hat{\mathbf{Q}}} \mathbf{N}_{\hat{\mathbf{Q}}\hat{\mathbf{U}}} \right] \mathbf{M}_{\hat{\mathbf{U}}\hat{\mathbf{U}}}^{-1}. \quad (2.28)$$

It is important to note the similarity between the internal force portion of (2.27) and the term within the square brackets in (2.28). These terms represent the net force on free and prescribed nodes, respectively, exerted by free nodes both directly, as a result of element-level forces, and indirectly, as a result of kinematic coupling to ghost atoms.

For the analyses presented in this paper, we used a preconditioned conjugate gradient algorithm [19] to solve equations (2.26) and (2.27). Alternatively, one could use a Newton solution scheme to derive the general procedure for solving the coupled system of equations, though some approximations to the procedure will be introduced later to make the solution tractable for larger systems. Linearizing the equilibrium equations about the \mathbf{Q} and \mathbf{U} yields

$$\mathbf{R}_{\mathbf{Q}}(\mathbf{Q}, \mathbf{U}) + \frac{\partial \mathbf{R}_{\mathbf{Q}}}{\partial \mathbf{Q}} \delta \mathbf{Q} + \frac{\partial \mathbf{R}_{\mathbf{Q}}}{\partial \mathbf{U}} \delta \mathbf{U} = 0, \quad (2.29)$$

$$\mathbf{R}_{\mathbf{U}}(\mathbf{Q}, \mathbf{U}) + \frac{\partial \mathbf{R}_{\mathbf{U}}}{\partial \mathbf{Q}} \delta \mathbf{Q} + \frac{\partial \mathbf{R}_{\mathbf{U}}}{\partial \mathbf{U}} \delta \mathbf{U} = 0, \quad (2.30)$$

which may be written in matrix form as

$$\begin{bmatrix} \mathbf{K}_{\mathbf{Q}\mathbf{Q}} & \mathbf{K}_{\mathbf{Q}\mathbf{U}} \\ \mathbf{K}_{\mathbf{U}\mathbf{Q}} & \mathbf{K}_{\mathbf{U}\mathbf{U}} \end{bmatrix} \begin{Bmatrix} \delta \mathbf{Q} \\ \delta \mathbf{U} \end{Bmatrix} = - \begin{Bmatrix} \mathbf{R}_{\mathbf{Q}} \\ \mathbf{R}_{\mathbf{U}} \end{Bmatrix}, \quad (2.31)$$

where the components of the symmetric tangent matrix are

$$\mathbf{K}_{\mathbf{Q}\mathbf{Q}} = \frac{\partial^2 \Pi_{\mathbf{Q}}}{\partial \mathbf{Q} \partial \mathbf{Q}} + \mathbf{J}_{\mathbf{Q}\hat{\mathbf{Q}}} \frac{\partial^2 \Pi_{\mathbf{Q}}}{\partial \hat{\mathbf{Q}} \partial \mathbf{Q}} + \frac{\partial^2 \Pi_{\mathbf{Q}}}{\partial \mathbf{Q} \partial \hat{\mathbf{Q}}} \mathbf{J}_{\mathbf{Q}\hat{\mathbf{Q}}}^{\mathbf{T}} + \mathbf{J}_{\mathbf{Q}\hat{\mathbf{Q}}} \frac{\partial^2 \Pi_{\mathbf{Q}}}{\partial \hat{\mathbf{Q}} \partial \hat{\mathbf{Q}}} \mathbf{J}_{\mathbf{Q}\hat{\mathbf{Q}}}^{\mathbf{T}} + \mathbf{L}_{\mathbf{Q}\hat{\mathbf{U}}} \frac{\partial^2 \Pi_{\mathbf{U}}}{\partial \hat{\mathbf{U}} \partial \hat{\mathbf{U}}} \mathbf{L}_{\mathbf{Q}\hat{\mathbf{U}}}^{\mathbf{T}}, \quad (2.32)$$

$$\mathbf{K}_{\mathbf{Q}\mathbf{U}} = \mathbf{K}_{\mathbf{U}\mathbf{Q}}^{\mathbf{T}} = \frac{\partial^2 \Pi_{\mathbf{Q}}}{\partial \mathbf{Q} \partial \hat{\mathbf{Q}}} \mathbf{N}_{\hat{\mathbf{Q}}\hat{\mathbf{U}}} + \mathbf{J}_{\mathbf{Q}\hat{\mathbf{Q}}} \frac{\partial^2 \Pi_{\mathbf{Q}}}{\partial \hat{\mathbf{Q}} \partial \hat{\mathbf{Q}}} \mathbf{N}_{\hat{\mathbf{Q}}\hat{\mathbf{U}}} + \mathbf{L}_{\mathbf{Q}\hat{\mathbf{U}}} \frac{\partial^2 \Pi_{\mathbf{U}}}{\partial \hat{\mathbf{U}} \partial \hat{\mathbf{U}}}, \quad (2.33)$$

$$\mathbf{K}_{\mathbf{U}\mathbf{U}} = \frac{\partial^2 \Pi_{\mathbf{U}}}{\partial \mathbf{U} \partial \mathbf{U}} + \mathbf{N}_{\hat{\mathbf{Q}}\hat{\mathbf{U}}}^{\mathbf{T}} \frac{\partial^2 \Pi_{\mathbf{Q}}}{\partial \hat{\mathbf{Q}} \partial \hat{\mathbf{Q}}} \mathbf{N}_{\hat{\mathbf{Q}}\hat{\mathbf{U}}}, \quad (2.34)$$

and

$$\mathbf{L}_{\mathbf{Q}\hat{\mathbf{U}}} = \mathbf{N}_{\hat{\mathbf{Q}}\hat{\mathbf{U}}} \mathbf{M}_{\hat{\mathbf{U}}\hat{\mathbf{U}}}^{-1}. \quad (2.35)$$

$$\mathbf{J}_{\mathbf{Q}\hat{\mathbf{Q}}} = \mathbf{L}_{\mathbf{Q}\hat{\mathbf{U}}} \mathbf{N}_{\hat{\mathbf{Q}}\hat{\mathbf{U}}}^{\mathbf{T}} \quad (2.36)$$

The solution of (2.31) could then be determined either monolithically or by staggering calculation of the updates $\delta \mathbf{Q}$ and $\delta \mathbf{U}$ during the iteration i as

$$\delta \mathbf{Q}^{(i)} = - \left[\mathbf{K}_{\mathbf{Q}\mathbf{Q}}^{(i)} \right]^{-1} \left[\mathbf{R}_{\mathbf{Q}}^{(i)} + \mathbf{K}_{\mathbf{Q}\mathbf{U}}^{(i)} \delta \mathbf{U}^{(i-1)} \right], \quad (2.37)$$

$$\delta \mathbf{U}^{(i)} = - \left[\mathbf{K}_{\mathbf{U}\mathbf{U}}^{(i+\frac{1}{2})} \right]^{-1} \left[\mathbf{R}_{\mathbf{U}}^{(i+\frac{1}{2})} + \mathbf{K}_{\mathbf{U}\mathbf{Q}}^{(i+\frac{1}{2})} \delta \mathbf{Q}^{(i)} \right], \quad (2.38)$$

where state i is defined by $\{\mathbf{Q}^{(i)}, \mathbf{U}^{(i)}\}$, while the state $i + \frac{1}{2}$ is defined by $\{\mathbf{Q}^{(i)} + \delta\mathbf{Q}^{(i)}, \mathbf{U}^{(i)}\}$. The numerical solution of (2.37) and (2.38) each involve the solution of a linear system. For atomistic calculations, this linear solution is generally not tractable due to the size and bandwidth of $\mathbf{K}_{\mathbf{Q}\mathbf{Q}}$. Typically, a nonlinear conjugate gradient algorithm is used, employing some approximation to $\mathbf{K}_{\mathbf{Q}\mathbf{Q}}^{-1}$ as a preconditioner. The matrix $\mathbf{M}_{\hat{\mathbf{U}}\hat{\mathbf{U}}}^{-1}$ is also not generally available and could be replaced by a diagonal approximation here, as well as in the projection. Due to these approximations, it may not be worthwhile to calculate $\mathbf{K}_{\mathbf{U}\mathbf{Q}}^{(i+\frac{1}{2})}$ in (2.38), and acceptable rates of convergence may be preserved by substitution of $\mathbf{K}_{\mathbf{Q}\mathbf{U}}^{(i)T}$. The effects of these approximations on the convergence rate and computational cost of the procedure need to be assessed with some sample calculations.

2.4 Projection using moving least squares

One of the principal drawbacks with the L_2 projection is calculation of $\mathbf{M}_{\hat{\mathbf{U}}\hat{\mathbf{U}}}^{-1}$, both effectively in the form of the solution of a linear system in evaluating the residual as given by (2.28) and explicitly as it appears in (2.32) and (2.33) of the tangent matrix through the expression for $\mathbf{L}_{\mathbf{Q}\hat{\mathbf{U}}}$ given in (2.35). An approximation to $\mathbf{M}_{\hat{\mathbf{U}}\hat{\mathbf{U}}}^{-1}$ can be used for the tangent stiffness, but approximations to the linear solution (2.28) required for evaluation of the residual will directly affect the accuracy of the solution. Evaluation of $\mathbf{M}_{\hat{\mathbf{U}}\hat{\mathbf{U}}}^{-1}$ becomes especially problematic with the application of the coupling scheme to dynamic problems when the residual will need to be evaluated a very large number of times.

Of course, the discretized L_2 projection (2.16) is not the only option for transferring the atomistic displacements to the finite element nodes. Rather than employing a global least squares approach, we can make use of a local, or so-called moving least squares (MLS), method to project atomistic information to the finite element nodes. The interpolants developed for the reproducing kernel particle method (RKPM) [20] possess a number of properties that make them well-suited for use in a coupling scheme. Among these properties are that the interpolants can be constructed to reproduce any desired function exactly. In particular, we will show that the interpolants must be able to reproduce a linear displacement field exactly in order for the coupled method to solve homogeneous deformations exactly. A number of additional useful properties of the interpolants is derived from the connection between RKPM and wavelets. This connection lends the interpretation of interpolating displacements from the atoms to the finite element nodes as a low pass filtering operation with a well-characterized spectral behavior. Moreover, the wavelet formalism furnishes a method wherein a series of these filters can be constructed to produce a hierarchical decomposition of the atomistic field into components possessing different scales of information.

RKPM belongs to a class of methods for which the approximation, or “image”, of a signal is

given by a kernel expression. In the transfer of displacements from the atoms to the nodes, the atomic information serves as the signal while the nodal information is the image. Without loss of generality, we can consider the expression for the approximation in one dimension

$$u^{R_\varepsilon}(x) = \int_{-\infty}^{+\infty} \phi_\varepsilon(x-y) u(y) dy, \quad (2.39)$$

where ϕ_ε is alternately called a weight, kernel, or smoothing function. From the analogy to signal processing, ϕ_ε may be viewed as a customizable low pass filter between the original signal, or data, $u(y)$ and its reproduced image. This function is positive, even, and has compact support characterized by the dilation parameter ε . Liu and Chen[21] improved the accuracy of the method by modifying the window function with a correction to yield a reproducing condition as

$$u^{R_\varepsilon}(x) = \int_{-\infty}^{+\infty} \bar{\phi}_\varepsilon(x-y) u(y) dy, \quad (2.40)$$

where the modified window function

$$\bar{\phi}_\varepsilon(x-y) = C(x; x-y) \phi_\varepsilon(x-y) \quad (2.41)$$

incorporates the polynomial

$$C(x; x-y) = b_0(x) + b_1(x) (x-y) + b_2(x) (x-y)^2 + \dots + b_m(x) (x-y)^m \quad (2.42)$$

which ensures that the approximation can exactly represent polynomials of order m . In general, we may express the correction function as

$$C(\mathbf{x}; \mathbf{x}-\mathbf{y}) = \mathbf{b}(\mathbf{x}) \cdot \mathbb{P}(\mathbf{x}-\mathbf{y}) \quad (2.43)$$

where \mathbb{P} is a basis of polynomials that possess the desired degree of completeness and $\mathbf{b}(\mathbf{x})$ is a vector of unknown coefficients determined from the reproducing condition (2.40). The requirement that each member of the basis be reproduced follows from (2.40) as

$$\mathbb{P}(\mathbf{0}) = \int_{-\infty}^{+\infty} \mathbf{b}(\mathbf{x}) \cdot \mathbb{P}(\mathbf{x}-\mathbf{y}) \phi_\varepsilon(\mathbf{x}-\mathbf{y}) \mathbb{P}(\mathbf{x}-\mathbf{y}) dy. \quad (2.44)$$

The vector of coefficients follows as

$$\mathbf{b}(\mathbf{x}) = \mathbb{M}_\varepsilon^{-1}(\mathbf{x}) \mathbb{P}(\mathbf{0}), \quad (2.45)$$

where

$$\mathbb{M}_\varepsilon(\mathbf{x}) = \int_{-\infty}^{+\infty} \mathbb{P}(\mathbf{x}-\mathbf{y}) \otimes \mathbb{P}(\mathbf{x}-\mathbf{y}) \phi_\varepsilon(\mathbf{x}-\mathbf{y}) dy \quad (2.46)$$

is known as the moment matrix. Using the result from (2.45), the reproducing condition (2.40) can be written as

$$\mathbf{u}^{R_\varepsilon}(\mathbf{x}) = \int_{-\infty}^{+\infty} \mathbf{b}(\mathbf{x}) \cdot \mathbb{P}(\mathbf{x} - \mathbf{y}) \phi_\varepsilon(\mathbf{x} - \mathbf{y}) \mathbf{u}(\mathbf{y}) d\mathbf{y}. \quad (2.47)$$

First and higher order gradients of the field representation follow from (2.45)–(2.47) through simple differentiation. For clarity, we present the expressions for derivatives. We note that these derivatives may be evaluated exactly though some early work in the MLS field advocated approximate expressions for these derivatives[22]. The gradient of the field may be expressed as

$$\begin{aligned} \frac{\partial \mathbf{u}^{R_\varepsilon}(\mathbf{x})}{\partial \mathbf{x}} = \int_{-\infty}^{+\infty} \mathbf{u}(\mathbf{y}) \otimes & \left[\frac{\partial \mathbf{b}(\mathbf{x})}{\partial \mathbf{x}} \mathbb{P}(\mathbf{x} - \mathbf{y}) \phi_\varepsilon(\mathbf{x} - \mathbf{y}) + \right. \\ & \mathbf{b}(\mathbf{x}) \frac{\partial \mathbb{P}(\mathbf{x} - \mathbf{y})}{\partial \mathbf{x}} \phi_\varepsilon(\mathbf{x} - \mathbf{y}) + \\ & \left. \mathbf{b}(\mathbf{x}) \cdot \mathbb{P}(\mathbf{x} - \mathbf{y}) \frac{\partial \phi_\varepsilon(\mathbf{x} - \mathbf{y})}{\partial \mathbf{x}} \right] d\mathbf{y}, \end{aligned} \quad (2.48)$$

where the gradient of the coefficient vector

$$\frac{\partial \mathbf{b}(\mathbf{x})}{\partial \mathbf{x}} = -\mathbb{M}_\varepsilon^{-1}(\mathbf{x}) \frac{\partial \mathbb{M}_\varepsilon(\mathbf{x})}{\partial \mathbf{x}} \mathbf{b}(\mathbf{x}) \quad (2.49)$$

follows from (2.45) making use of the relation

$$\frac{\partial [\mathbb{M}_\varepsilon^{-1}]_{ij}}{\partial x_k} = -[\mathbb{M}_\varepsilon^{-1}]_{ir} \frac{\partial [\mathbb{M}_\varepsilon]_{rs}}{\partial x_k} [\mathbb{M}_\varepsilon^{-1}]_{sj}. \quad (2.50)$$

Higher-order gradients may be calculated by further differentiation of (2.48)–(2.50). Notably, the expressions for the representation of the unknown field variables are general for an arbitrary number of field and spatial dimensions, including the expressions for the first and higher order gradients of the field.

In evaluating the representations for the nodal field from the atomistic information, we discretize the integrals in the previous expressions. The discrete reproducing condition follows from (2.47) as

$$\mathbf{u}(\mathbf{X}) = \sum_{\beta=1}^{N_p} \mathbf{b}(\mathbf{X}) \cdot \mathbb{P}(\mathbf{X} - \mathbf{X}^{(\beta)}) \phi_\varepsilon(\mathbf{X} - \mathbf{X}^{(\beta)}) \mathbf{q}^{(\beta)} \Delta V^{(\beta)}, \quad (2.51)$$

where N_p is the number of sampling atoms under consideration, and $\mathbf{X}^{(\beta)}$ and $\Delta V^{(\beta)}$ are the coordinates and integration weight (volume) associated with atom β , respectively. From (2.51),

we can identify the RKPM nodal shape functions as

$$\mathbf{u}^{(a)} = \sum_{\beta=1}^{N_p} \tilde{N}^{(\beta)}(\mathbf{X}^{(a)}) \mathbf{q}^{(\beta)}, \quad (2.52)$$

where

$$\tilde{N}^{(\beta)}(\mathbf{X}) = \mathbf{b}(\mathbf{X}) \cdot \mathbb{P}(\mathbf{X} - \mathbf{X}^{(\beta)}) \phi_\varepsilon(\mathbf{X} - \mathbf{X}^{(\beta)}) \Delta V^{(\beta)}, \quad (2.53)$$

$a \in \hat{\mathcal{N}}$ and $\beta \in \mathcal{A}$.

With these interpolants, we can express the prescribed continuum and atomic displacements respectively as

$$\hat{\mathbf{U}} = \tilde{\mathbf{N}}_{\hat{\mathbf{U}}\mathbf{Q}} \mathbf{Q}, \quad (2.54)$$

$$\hat{\mathbf{Q}} = \mathbf{N}_{\hat{\mathbf{Q}}\mathbf{U}} \mathbf{U} + \mathbf{N}_{\hat{\mathbf{Q}}\hat{\mathbf{U}}} \tilde{\mathbf{N}}_{\hat{\mathbf{U}}\mathbf{Q}} \mathbf{Q}, \quad (2.55)$$

where $\tilde{\mathbf{N}}_{\hat{\mathbf{U}}\mathbf{Q}}$ is the matrix of RKPM shape functions defined by the expansion (2.52). Using (2.54) and (2.55), the equilibrium equations can be expressed as

$$\mathbf{R}_{\mathbf{Q}} = \frac{\partial \Pi_{\mathbf{Q}}}{\partial \mathbf{Q}} + \left[\frac{\partial \Pi_{\mathbf{U}}}{\partial \hat{\mathbf{U}}} + \frac{\partial \Pi_{\mathbf{Q}}}{\partial \hat{\mathbf{Q}}} \mathbf{N}_{\hat{\mathbf{Q}}\hat{\mathbf{U}}} \right] \tilde{\mathbf{N}}_{\hat{\mathbf{U}}\mathbf{Q}} - \mathbf{F}_{\mathbf{Q}} = 0, \quad (2.56)$$

$$\mathbf{R}_{\mathbf{U}} = \frac{\partial \Pi_{\mathbf{U}}}{\partial \mathbf{U}} + \frac{\partial \Pi_{\mathbf{Q}}}{\partial \hat{\mathbf{Q}}} \mathbf{N}_{\hat{\mathbf{Q}}\mathbf{U}} - \mathbf{F}_{\mathbf{U}} = 0, \quad (2.57)$$

which yield the components of the tangent matrix

$$\mathbf{K}_{\mathbf{Q}\mathbf{Q}} = \frac{\partial^2 \Pi_{\mathbf{Q}}}{\partial \mathbf{Q} \partial \mathbf{Q}} + \tilde{\mathbf{J}}_{\mathbf{Q}\hat{\mathbf{Q}}} \frac{\partial^2 \Pi_{\mathbf{Q}}}{\partial \hat{\mathbf{Q}} \partial \mathbf{Q}} + \frac{\partial^2 \Pi_{\mathbf{Q}}}{\partial \mathbf{Q} \partial \hat{\mathbf{Q}}} \tilde{\mathbf{J}}_{\mathbf{Q}\hat{\mathbf{Q}}}^T + \tilde{\mathbf{J}}_{\mathbf{Q}\hat{\mathbf{Q}}} \frac{\partial^2 \Pi_{\mathbf{Q}}}{\partial \hat{\mathbf{Q}} \partial \hat{\mathbf{Q}}} \tilde{\mathbf{J}}_{\mathbf{Q}\hat{\mathbf{Q}}}^T + \tilde{\mathbf{N}}_{\hat{\mathbf{U}}\mathbf{Q}}^T \frac{\partial^2 \Pi_{\mathbf{U}}}{\partial \hat{\mathbf{U}} \partial \hat{\mathbf{U}}} \tilde{\mathbf{N}}_{\hat{\mathbf{U}}\mathbf{Q}}, \quad (2.58)$$

$$\mathbf{K}_{\mathbf{Q}\mathbf{U}} = \mathbf{K}_{\mathbf{U}\mathbf{Q}}^T = \frac{\partial^2 \Pi_{\mathbf{Q}}}{\partial \mathbf{Q} \partial \hat{\mathbf{Q}}} \mathbf{N}_{\hat{\mathbf{Q}}\mathbf{U}} + \tilde{\mathbf{J}}_{\mathbf{Q}\hat{\mathbf{Q}}} \frac{\partial^2 \Pi_{\mathbf{Q}}}{\partial \hat{\mathbf{Q}} \partial \hat{\mathbf{Q}}} \mathbf{N}_{\hat{\mathbf{Q}}\mathbf{U}} + \tilde{\mathbf{N}}_{\hat{\mathbf{U}}\mathbf{Q}}^T \frac{\partial^2 \Pi_{\mathbf{U}}}{\partial \hat{\mathbf{U}} \partial \mathbf{U}}, \quad (2.59)$$

$$\mathbf{K}_{\mathbf{U}\mathbf{U}} = \frac{\partial^2 \Pi_{\mathbf{U}}}{\partial \mathbf{U} \partial \mathbf{U}} + \mathbf{N}_{\hat{\mathbf{Q}}\mathbf{U}}^T \frac{\partial^2 \Pi_{\mathbf{Q}}}{\partial \hat{\mathbf{Q}} \partial \hat{\mathbf{Q}}} \mathbf{N}_{\hat{\mathbf{Q}}\mathbf{U}}. \quad (2.60)$$

where

$$\tilde{\mathbf{J}}_{\mathbf{Q}\hat{\mathbf{Q}}} = \tilde{\mathbf{N}}_{\hat{\mathbf{U}}\mathbf{Q}}^T \mathbf{N}_{\hat{\mathbf{Q}}\hat{\mathbf{U}}}^T. \quad (2.61)$$

The choice of projection/interpolation method, L_2 or MLS, combined with the designation of atoms being free or ghost, determines whether nodes are classified as free or prescribed. For example, we consider the case of an overlap element that contains both ghost and free atoms and we assume that the relative size of the element is sufficiently large to contain many atoms. Using the L_2 method, we note that if the element contains any free atoms, all nodes that bound that element must be prescribed in order to preserve the orthogonality of

the shape functions. This is true even for situations in which very few of the atoms have been designated as free atoms, and these free atoms are very distant from the node under consideration. For such nodes, the resulting projection becomes overly sensitive to gradients in the atomistic displacements at the crystal edge. However, a MLS method would only require free atoms within a limited-sized support region surrounding the prescribed node. If the free atoms are too far away, and an insufficient density of free atoms exists in the vicinity of the node, the node can be designated as free. It is important to note that the designation of the atoms as free or ghost and their distribution with regard to the underlying mesh dictates which projection method would be best suited and what the resulting designation of the nodes should be. Hence, atomistic character drives nodal character.

2.5 Correction to the Cauchy-Born rule in the overlap region

The previous sections describe how atomistic and continuum degrees of freedom are coupled; however, the specific form of the total potential has not yet been given. Naturally, atomistic contribution to the potential energy is computed from a sum of bond energies in the crystal. The continuum strain energy is computed using the Cauchy-Born rule [14, 15], which accurately describes the long wavelength behavior of the lattice. A critical detail to address is how one corrects for the overlap of the continuum and the underlying crystal. The proposed coupling method covers the entire domain with finite elements, but prescribes the motion of select portions of the mesh using an underlying atomistic crystal. Around the edges of the embedded crystals, there will be some region over which there is overlap between the bonds between free and ghost atoms and finite elements containing nodes with both free and prescribed displacements. In this overlap region, the weighting of the contributions to potential energy from the bonds and finite elements needs to be determined in such a way that the total energy for the coupled system is consistent with the result one would obtain from a pure atomistic system, regardless of the location and orientation of the embedded crystals with respect to the overlaying finite element mesh.

We can determine immediately that the weighting of the bonds between free and ghost atoms must always be 1 to preserve the energy per atom among free atoms, while the weighting of contributions from elements containing both active nodes and ghost atoms must be compensated to maintain the correct strain energy density. An initial attempt to quantify this weighting factor can be made by considering elements with uniform strain energy density, and by expressing the total strain energy in the continuum as

$$\Pi_{\mathbf{U}} = \sum_e^{N_e} w_e \Phi_e V_e, \quad (2.62)$$

where Φ_e and V_e are the strain energy density and volume, respectively, of element e and all elements $e \in N_e$ contribute energy according to a weighting factor w_e . For elements with no underlying atomic lattice, $w_e = 1$, while for elements that are bounded only by nodes with displacements projected from the underlying atomic lattice, $w_e = 0$. For overlap elements that contain ghost atoms and are bounded by both free and prescribed nodes, $0 \leq w_e \leq 1$. Note that the problem of finding these weights is underdetermined if one only considers the total energy of the system. That is, any number of combinations of weights can be found that reproduce the same total energy for the coupled system under homogeneous deformations. However, only one combination maintains the homogeneously deformed state as the lowest energy configuration. For simple one-dimensional examples, one can deduce the weights w_e . For the case of pair interactions, the weighing for these elements, assuming homogeneous stretching over the entire system, is

$$w_e = 1 - \frac{\sum_{\alpha\beta} \hat{r}_e^{(\alpha\beta)} \varphi^{(\alpha\beta)}}{V_e \Phi_e}, \quad (2.63)$$

where $\hat{r}_e^{(\alpha\beta)}$ is the fraction of the bond between atoms α and β that lies within the element and $\varphi^{(\alpha\beta)}$ is bond energy. Given that Φ_e is calculated for the continuum using the same bond potentials as for the crystal subject to the Cauchy-Born rule, it may be possible to express the weight w_e in a way that is independent of the state of deformation. That is, w_e must be expressed strictly in terms of the geometric parameters $\hat{r}_e^{(\alpha\beta)}$ and V_e , independent of Φ_e and $\varphi^{(\alpha\beta)}$; otherwise, the weighting factor would appear to be a function of the deformation even for the case of homogeneous deformation. If one uses elements with dimensions that are multiples of the crystal's unit cell, elements completely covering the underlying crystal have $w_e = 0$ since the strain energy density following the Cauchy-Born rule dictates

$$\Phi_e = \frac{1}{V_e} \sum_{\alpha\beta} \varphi^{(\alpha\beta)}. \quad (2.64)$$

For the extension to multiple dimensions and nonuniform strain energy density within elements, a general approach for introducing weighting into the total potential must be developed as well as a method for determining the optimal weighting, where optimality is associated with maintaining the homogeneously deformed state as the lowest energy configuration. The approach for introducing weighting into the total potential follows directly from the Cauchy-Born rule. A generalized form of the Cauchy-Born rule for particles interacting with pair potentials was introduced by Gao and Klein in their Virtual Internal Bond model (VIB) [23, 24]. The VIB form of the strain energy density function is

$$\Phi = \frac{1}{V_0} \int_{V_0^*} U(r) D dV, \quad (2.65)$$

where V_0 is the undeformed representative volume, r is the deformed virtual bond length, $U(r)$ is the bonding potential, D is the volumetric bond density function, and V_0^* is the integration volume defined by the range of influence of U . Depending on the range of influence of the bond potential function, the integration volume V_0^* may not correspond with the representative volume V_0 . This difference may be illustrated for crystalline materials whenever the bond potentials extend beyond the lattice unit cell. The precise definition of $D(R, \theta, \phi)$ is that $D(R, \theta, \phi) R^2 \sin \theta dR d\theta d\phi$ represents the number of bonds in the undeformed solid with length between R and $R + dR$ and orientation between $\{\theta, \phi\}$ and $\{\theta + d\theta, \phi + d\phi\}$. The case

$$D(R, \theta, \phi) = \delta_D(R - R_0) D_{\theta\phi}(\theta, \phi) \quad (2.66)$$

corresponds to a network of identical bonds of undeformed length R_0 . The Dirac delta function is denoted here with δ_D . A crystal lattice such as face-centered cubic with interactions limited to only first nearest neighbors can be represented as

$$D(R, \theta, \phi) = D_0 \delta_D(R - R_0) \sum_{m=1}^M \sum_{n=1}^N \frac{1}{\sin \theta} \delta_D(\theta - \theta_m) \delta_D(\phi - \phi_n), \quad (2.67)$$

where D_0 is a scaling constant and θ_m and ϕ_n are the orientation angles for the neighboring atoms. Each bond in $D(R, \theta, \phi)$ is representative of all bonds in the crystal with the same orientation and length.

For the coupled system, the bond density function needs to be modified as

$$D(R, \theta, \phi, \mathbf{X}) = D_0 \delta_D(R - R_0) \sum_{m=1}^M \sum_{n=1}^N \frac{1}{\sin \theta} \delta_D(\theta - \theta_m) \delta_D(\phi - \phi_n) \rho_{mn}(\mathbf{X}), \quad (2.68)$$

where the spatially varying $0 \leq \rho_{mn}(\mathbf{X}) \leq 1$ is introduced because the energy contained by bonds between atoms that are explicitly represented, such as between free atoms and other free atoms or free atoms and ghost atoms, is already contributing to $\Pi_{\mathbf{Q}}$. Hence, that energy does not need to be accounted for in $\Pi_{\mathbf{U}}$. In regions of the domain superposed by a complete underlying crystal, $\rho_{mn}(\mathbf{X}) = 0$ since all bonds are represented at the density of the crystal. Conversely, $\rho_{mn}(\mathbf{X}) = 1$ over the parts of the domain without any underlying crystal since the Cauchy-Born strain energy density must account for all of the potential energy. In general, the strain energy for a crystal subject to pair interactions can be expressed as the sum

$$\Phi(\mathbf{C}, \mathbf{X}) = \frac{1}{V_0} \sum_i^{n_b} \rho_{(i)}(\mathbf{X}) \varphi(r_{(i)}), \quad (2.69)$$

where φ is the interaction potential,

$$r_{(i)} = \sqrt{\mathbf{R}_{(i)} \cdot \mathbf{C} \mathbf{R}_{(i)}}, \quad \mathbf{C} = \mathbf{F}^T \mathbf{F}, \quad (2.70)$$

$\mathbf{R}_{(i)}$ is the vector representing bond (i) in the undeformed configuration and \mathbf{F} is the deformation gradient. In this paper, (i) refers to not just a single bond, but rather all bonds of

the same type, *i.e.* having the same orientation and length in the reference configuration. Hence, n_b is the total number of bond types.

With this generalization of the Cauchy-Born, we decompose the contribution to the total energy from the continuum (2.23) as

$$\Pi_{\mathbf{U}} = \sum_i^{n_b} [\Pi_{\mathbf{U}}]_{(i)} \quad (2.71)$$

where

$$[\Pi_{\mathbf{U}}]_{(i)} = [\Pi'_{\mathbf{U}}]_{(i)} + [\tilde{\Pi}_{\mathbf{U}}]_{(i)} + [\bar{\Pi}_{\mathbf{U}}]_{(i)}. \quad (2.72)$$

$[\Pi'_{\mathbf{U}}]_{(i)}$ represents the contribution over the domain where $\rho_{(i)} = 0$, which in the undeformed configuration will be denoted $\Omega'_{0(i)}$, $[\tilde{\Pi}_{\mathbf{U}}]_{(i)}$ represents the contribution over the domain where $0 < \rho_{(i)} < 1$, which in the undeformed configuration will be denoted $\tilde{\Omega}_{0(i)}$, and $[\bar{\Pi}_{\mathbf{U}}]_{(i)}$ represents the contribution over the domain where $\rho_{(i)} = 1$, which in the undeformed configuration will be denoted $\bar{\Omega}_{0(i)}$. Clearly, $[\Pi'_{\mathbf{U}}]_{(i)} = 0$. However, for completeness the decomposed domain in the undeformed configuration is defined as

$$\Omega_0 = \Omega'_{0(i)} \cup \tilde{\Omega}_{0(i)} \cup \bar{\Omega}_{0(i)}, \quad (2.73)$$

where

$$\Omega'_{0(i)} \cap \tilde{\Omega}_{0(i)} = \emptyset \quad \tilde{\Omega}_{0(i)} \cap \bar{\Omega}_{0(i)} = \emptyset \quad \bar{\Omega}_{0(i)} \cap \Omega'_{0(i)} = \emptyset. \quad (2.74)$$

Notice in (2.73) that while each of the decomposed domain sub-regions depends on the bond (i) being considered, the total domain Ω_0 refers to the entire volume of the system and no bond designation is necessary. The contribution to the strain energy from the bonds of type (i) represented in the continuum is given by

$$[\tilde{\Pi}_{\mathbf{U}}]_{(i)} = \frac{1}{V_0} \int_{\tilde{\Omega}_{0(i)}} \rho_{(i)}(\mathbf{X}) \varphi(r_{(i)}) d\Omega \quad (2.75)$$

$$[\bar{\Pi}_{\mathbf{U}}]_{(i)} = \frac{1}{V_0} \int_{\bar{\Omega}_{0(i)}} \varphi(r_{(i)}) d\Omega. \quad (2.76)$$

In (2.75), the spatially varying bond density is introduced to account for the overlap between the continuum domain and the underlying crystal. We must still define how these bond densities are determined. For bonds $\mathbf{r}^{(\alpha\beta)}$ with atoms α and β both within given volume, such as a finite element, the contribution of $\mathbf{r}^{(\alpha\beta)}$ to the bond density of the volume is clear; however, if either α or β lies outside the volume, the fraction of the bond to attribute to this volume is not clear. Considering fractions of the bond length is an arbitrary construction that is only defined unambiguously in 1-dimensional systems. However, in multiple dimensions bond fractions may lie outside the elements containing either α or β , as illustrated

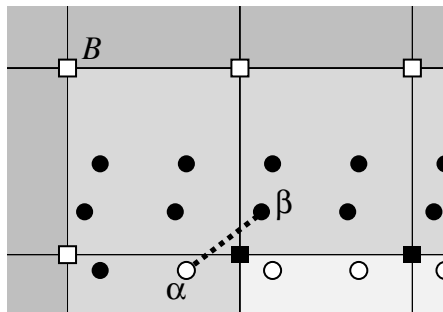


Figure 2.2: Bond between atoms near element boundaries.

in Figure 2.2, even when the atomic spacing is much smaller than the element dimensions. In Figure 2.2, the bond between atoms α and β is shown to overlap an element bounded by node B . However, it is unclear whether this bond should exert forces on node B since neither atom α nor atom β lie within that element. For multi-body interactions, the division of the bond energy in space is even more difficult to define unambiguously.

To avoid the ambiguity associated with partitioning a bond, we determine the bond densities in (2.75) based on a consistency condition. The coupled system should produce homogeneous deformations given the appropriate boundary conditions. This concept is analogous to the "patch test" for assessing the convergence of the FE method [25]. One could consider the unstressed system, but in general we would like to satisfy this consistency condition for any homogeneous state of deformation which the atomistic or continuum system would produce individually. For the atoms $\alpha \in \mathcal{A}$ which are not located near surfaces or other crystal defects, this condition is satisfied automatically. These atoms only interact with other atoms in \mathcal{A} or with the ghost atoms in $\hat{\mathcal{A}}$ which have been introduced to provide a complete surrounding. For nodes whose support lies entirely in $\bar{\Omega}_{0(i)}$, the homogeneous solution will be reproduced as long as the element formulation satisfies the patch test. However, for nodes $a \in \check{\mathcal{N}}$ whose support intersects $\tilde{\Omega}_{0(i)}$, this consistency condition is not guaranteed. Let $\Omega_0^{(a)}$ denote the support of node a in the undeformed configuration, as illustrated in Figure 2.3. We define $\tilde{\mathcal{N}}_{(i)}$ as the subset of $\check{\mathcal{N}}$ containing all nodes satisfying

$$\Omega_0^{(a)} \cap \tilde{\Omega}_{0(i)} \equiv \tilde{\Omega}_{0(i)}^{(a)} \neq \emptyset. \quad (2.77)$$

We begin the derivation of this consistency condition by considering a general state of homogeneous deformation, which may be expressed as

$$\mathbf{u}(\mathbf{X}, t) = \mathbf{c}(t) + \mathbf{Q}(t) \mathbf{F}^* \mathbf{X}, \quad (2.78)$$

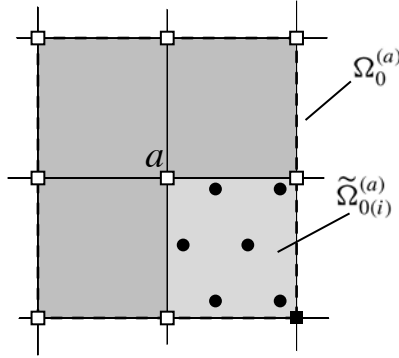


Figure 2.3: The support of node $a \in \tilde{\mathcal{N}}_{(i)}$.

where $\mathbf{c}(t)$ is a rigid body translation, $\mathbf{Q}(t)$ is a rigid body rotation, and \mathbf{F}^* is the homogeneous deformation gradient over the entire domain. Since all contributions to the total potential are frame invariant, we can consider the following state of homogeneous deformation

$$\mathbf{x} = \mathbf{F}^* \mathbf{X} \quad \text{and} \quad \mathbf{u} = (\mathbf{F}^* - \mathbf{1}) \mathbf{X} \quad (2.79)$$

without loss of generality. In determining the total internal force on a node in $\tilde{\mathcal{N}}_{(i)}$, we find three types of contributions. There are continuum contributions from $[\tilde{\Pi}_{\mathbf{U}}]_{(i)}$ and $[\bar{\Pi}_{\mathbf{U}}]_{(i)}$, and a third contribution from bonds between free atoms in either $\Omega'_{0(i)}$ or $\tilde{\Omega}_{0(i)}^{(a)}$ and ghost atoms in $\tilde{\Omega}_{0(i)}^{(a)}$, represented by the terms $\frac{\partial \Pi_{\mathbf{Q}}}{\partial \mathbf{Q}} \mathbf{N}_{\hat{\mathbf{Q}}\mathbf{U}}$ in (2.27) and $\frac{\partial \Pi_{\mathbf{Q}}}{\partial \mathbf{Q}} \mathbf{N}_{\hat{\mathbf{Q}}\hat{\mathbf{U}}}$ in (2.28).

First, we consider the atomistic contribution. The potential energy in the bonds is given by

$$\Pi_{\mathbf{Q}} = \sum_{\alpha} \sum_{\beta \neq \alpha} \varphi(r^{(\alpha\beta)}). \quad (2.80)$$

The atomistic contribution to the force on a node in $\tilde{\mathcal{N}}_{(i)}$ is given by

$$\mathbf{f}_{\mathbf{Q}}^{(a)} = -\frac{\partial \Pi_{\mathbf{Q}}}{\partial \mathbf{u}^{(a)}} \quad a \in \tilde{\mathcal{N}}_{(i)}. \quad (2.81)$$

For this analysis, we examine the total force on node (a) which includes contributions from all bond types $i = 1, 2, \dots, n_b$ as long as there is at least a single bond type for which $a \in \tilde{\mathcal{N}}_{(i)}$. We shall show later that for those bonds for which $a \notin \tilde{\mathcal{N}}_{(i)}$, the expression for total force evaluates to zero. The only bonds contributing to $\mathbf{f}_{\mathbf{Q}}^{(a)}$ are those between free atom (α) , which resides in either $\Omega'_{0(i)}$ or $\tilde{\Omega}_{0(i)}^{(a)}$, and ghost atom (β) , which resides in $\tilde{\Omega}_{0(i)}^{(a)}$.

The bond vector may be expressed as

$$\begin{aligned}
 \mathbf{r}^{(\alpha\beta)} &= \mathbf{x}^{(\beta)} - \mathbf{x}^{(\alpha)} \\
 &= [\mathbf{X}^{(\beta)} + \mathbf{u}(\mathbf{X}^{(\beta)})] - [\mathbf{X}^{(\alpha)} + \mathbf{q}^{(\alpha)}] \\
 &= \mathbf{X}^{(\beta)} + \sum_{a \in \tilde{\mathcal{N}}(i)} N^{(a)}(\mathbf{X}^{(\beta)}) \mathbf{u}^{(a)} - \mathbf{X}^{(\alpha)} - \mathbf{q}^{(\alpha)}, \\
 &= \sum_{a \in \tilde{\mathcal{N}}(i)} N^{(a)}(\mathbf{X}^{(\beta)}) \mathbf{u}^{(a)} - \mathbf{q}^{(\alpha)} + \mathbf{R}^{(\alpha\beta)},
 \end{aligned} \tag{2.82}$$

and

$$\frac{\partial \mathbf{r}^{(\alpha\beta)}}{\partial \mathbf{u}^{(a)}} = N^{(a)}(\mathbf{X}^{(\beta)}) \mathbf{1}. \tag{2.83}$$

Using this result, $\mathbf{f}_{\mathbf{Q}}^{(a)}$ (2.81) may be expanded as

$$\mathbf{f}_{\mathbf{Q}}^{(a)} = -\mathbf{F}^* \sum_{\alpha \in \mathcal{A}} \sum_{\beta: \mathbf{X}^{(\beta)} \in \tilde{\Omega}_0^{(a)}} \frac{\varphi'(r^{(\alpha\beta)})}{r^{(\alpha\beta)}} \mathbf{R}^{(\alpha\beta)} N^{(a)}(\mathbf{X}^{(\beta)}). \tag{2.84}$$

The continuum contribution over $\bar{\Omega}_{0(i)}$ follows from

$$\bar{\mathbf{f}}_{\mathbf{U}}^{(a)} = - \sum_i^{n_b} \frac{\partial \bar{\Pi}_{\mathbf{U}(i)}}{\partial \mathbf{u}^{(a)}} = - \sum_i^{n_b} \frac{\partial}{\partial \mathbf{u}^{(a)}} \int_{\bar{\Omega}_{0(i)}^{(a)}} \Phi d\Omega = - \sum_i^{n_b} \int_{\bar{\Omega}_{0(i)}^{(a)}} \mathbf{P} : \frac{\partial \mathbf{F}}{\partial \mathbf{u}^{(a)}} d\Omega, \tag{2.85}$$

where $\bar{\Omega}_{0(i)}^{(a)} \equiv \bar{\Omega}_{0(i)} \cap \Omega_0^{(a)}$ and $\mathbf{P} = \frac{\partial \Phi}{\partial \mathbf{F}}$ is the non-symmetric, first Piola-Kirchhoff stress. From Φ given by (2.69), the Piola-Kirchhoff stress is

$$\mathbf{P} = \mathbf{F} \frac{1}{V_0} \sum_i^{n_b} \frac{\varphi'(r_{(i)})}{r_{(i)}} \mathbf{R}_{(i)} \otimes \mathbf{R}_{(i)}, \tag{2.86}$$

using the relations

$$\mathbf{r}_{(i)} = \mathbf{F}^* \mathbf{R}_{(i)} \quad \text{and} \quad \frac{\partial r_{(i)}}{\partial \mathbf{F}} = \frac{1}{r_{(i)}} \mathbf{r}_{(i)} \otimes \mathbf{R}_{(i)}. \tag{2.87}$$

Using

$$\frac{\partial F_{iJ}}{\partial u_k^{(a)}} = \frac{\partial N^{(a)}}{\partial X_J} \delta_{ik}, \tag{2.88}$$

we can expand $\bar{\mathbf{f}}_{\mathbf{U}}^{(a)}$ as

$$\bar{\mathbf{f}}_{\mathbf{U}}^{(a)} = -\mathbf{F}^* \frac{1}{V_0} \sum_i^{n_b} \int_{\bar{\Omega}_{0(i)}^{(a)}} \left[\frac{\varphi'(r)}{r} \mathbf{R} \otimes \mathbf{R} \right]_{(i)} \frac{\partial N^{(a)}}{\partial \mathbf{X}} d\Omega. \tag{2.89}$$

The contribution from $\left[\tilde{\Pi}_{\mathbf{U}}\right]_{(i)}$ differs from (2.89) only by the introduction of the bond density function $\rho_{(i)}(\mathbf{X})$ for $i = 1, \dots, n_b$ and the integration domain, and is given by

$$\tilde{\mathbf{f}}_{\mathbf{U}}^{(a)} = - \sum_i^{n_b} \frac{\partial \tilde{\Pi}_{\mathbf{U}(i)}}{\partial \mathbf{u}^{(a)}} = -\mathbf{F}^* \frac{1}{V_0} \sum_i^{n_b} \int_{\tilde{\Omega}_{0(i)}^{(a)}} \left[\frac{\varphi'(r)}{r} \mathbf{R} \otimes \mathbf{R} \right]_{(i)} \frac{\partial N^{(a)}}{\partial \mathbf{X}} d\Omega. \quad (2.90)$$

Many terms in the integrands of (2.89) and (2.90) do not vary spatially if the body is in a state of homogeneous deformation. Therefore, we can rewrite these expressions as

$$\bar{\mathbf{f}}_{\mathbf{U}}^{(a)} = -\mathbf{F}^* \frac{1}{V_0} \sum_i^{n_b} \left[\frac{\varphi'(r)}{r} \mathbf{R} \otimes \mathbf{R} \right]_{(i)} \int_{\tilde{\Omega}_{0(i)}^{(a)}} \frac{\partial N^{(a)}}{\partial \mathbf{X}} d\Omega \quad (2.91)$$

and

$$\tilde{\mathbf{f}}_{\mathbf{U}}^{(a)} = -\mathbf{F}^* \frac{1}{V_0} \sum_i^{n_b} \left[\frac{\varphi'(r)}{r} \mathbf{R} \otimes \mathbf{R} \right]_{(i)} \int_{\tilde{\Omega}_{0(i)}^{(a)}} \rho_{(i)} \frac{\partial N^{(a)}}{\partial \mathbf{X}} d\Omega. \quad (2.92)$$

Since the Cauchy-Born expressions for the continuum response were selected to represent the crystal structure of the underlying atomistic system, the bonds in (2.84) may be collected into the same groups by orientation and length as those given by the bond types $i = 1, \dots, n_b$ in (2.91) and (2.92). Using this observation, $\mathbf{f}_{\mathbf{Q}}^{(a)}$ from (2.84) may be expressed as

$$\mathbf{f}_{\mathbf{Q}}^{(a)} = -\mathbf{F}^* \sum_i^{n_b} \left[\frac{\varphi'(r)}{r} \mathbf{R} \sum_{\substack{\beta: \mathbf{X}^{(\beta)} \in \tilde{\Omega}_{0(i)}^{(a)}, \\ \mathbf{R}^{(\alpha\beta)} = \mathbf{R}}} N^{(a)}(\mathbf{X}^{(\beta)}) \right]_{(i)} \quad (2.93)$$

Collecting these expressions for the force on a node in $\tilde{\mathcal{N}}_{(i)}$, we find

$$\mathbf{f}^{(a)} = \mathbf{f}_{\mathbf{Q}}^{(a)} + \bar{\mathbf{f}}_{\mathbf{U}}^{(a)} + \tilde{\mathbf{f}}_{\mathbf{U}}^{(a)} = -\mathbf{F}^* \sum_i^{n_b} \left[\frac{\varphi'(r)}{r} \right]_{(i)} \mathbf{f}_{(i)}^{(a)}, \quad (2.94)$$

where

$$\mathbf{f}_{(i)}^{(a)} = \mathbf{R}_{(i)} \sum_{\substack{\beta: \mathbf{X}^{(\beta)} \in \tilde{\Omega}_{0(i)}^{(a)}, \\ \mathbf{R}^{(\alpha\beta)} = \mathbf{R}_{(i)}}} N^{(a)}(\mathbf{X}^{(\beta)}) + \frac{1}{V_0} [\mathbf{R} \otimes \mathbf{R}]_{(i)} \left[\int_{\tilde{\Omega}_{0(i)}^{(a)}} \frac{\partial N^{(a)}}{\partial \mathbf{X}} d\Omega + \int_{\tilde{\Omega}_{0(i)}^{(a)}} \rho_{(i)} \frac{\partial N^{(a)}}{\partial \mathbf{X}} d\Omega \right]. \quad (2.95)$$

Note that $\mathbf{f}_{(i)}^{(a)}$ in (2.95) has units of length, and thus can be directly interpreted as bond overlap. Also, it is independent of the homogeneous state of deformation, depending only on the geometry of the undeformed configuration.

Earlier, we mentioned that (2.95) is evaluated for any node (a) such that $a \in \tilde{\mathcal{N}}_{(i)}$ for at least one bond type (i). For any bond type (i) for which $a \notin \tilde{\mathcal{N}}_{(i)}$, it can be shown that (2.95) evaluates to zero. For such atoms, $\tilde{\Omega}_{0(i)}^{(a)} = \emptyset$ and $\bar{\Omega}_{0(i)}^{(a)} = \Omega_0^{(a)}$. Thus, (2.95) simplifies to

$$\mathbf{f}_{(i)}^{(a)} = \frac{1}{V_0} [\mathbf{R} \otimes \mathbf{R}]_{(i)} \int_{\Omega_0^{(a)}} \frac{\partial N^{(a)}}{\partial \mathbf{X}} d\Omega. \quad (2.96)$$

The integral of the gradient of the nodal shape function over the support of the zone is

$$\int_{\Omega_0^{(a)}} \frac{\partial N^{(a)}}{\partial \mathbf{X}} d\Omega = \oint_{\partial\Omega_0^{(a)}} N^{(a)} \mathbf{N} d\Gamma = 0, \quad (2.97)$$

where \mathbf{N} is the outward normal over $\partial\Omega_0^{(a)}$, the boundary of the support of node (a). We can combine (2.96) and (2.97) to produce $\mathbf{f}_{(i)}^{(a)} = 0$.

If we define the quantity $\tilde{\mathbf{R}}$ to be

$$\tilde{\mathbf{R}} = [\mathbf{f}^{(a)}]^T a \in \tilde{\mathcal{N}}_{(i)}, \quad (2.98)$$

then in the absence of external loads being imposed directly on the nodes in $\tilde{\mathcal{N}}_{(i)}$, we would expect $|\tilde{\mathbf{R}}| = 0$ for all states of deformation. For the case of homogeneous deformation, this amounts to enforcing the condition $\mathbf{f}_{(i)}^{(a)} = 0$ for all $i = 1, \dots, n_b$ and $a \in \tilde{\mathcal{N}}_{(i)}$, which implies (2.95) provides a means for defining the discretized values of $\rho_{(i)}$ optimally. In most situations, the discretization of the bond density $\rho_{(i)}$ may be insufficient to capture the local fluctuation in the bond density required to produce $\mathbf{f}_{(i)}^{(a)} = 0$ exactly. Therefore we approximate this condition by introducing

$$P_{(i)} = \frac{1}{2} \sum_{a \in \tilde{\mathcal{N}}_i} \mathbf{f}_{(i)}^{(a)} \cdot \mathbf{f}_{(i)}^{(a)}. \quad (2.99)$$

and then select $\boldsymbol{\rho}_{(i)}$ that satisfies

$$\min_{\boldsymbol{\rho}_{(i)}} [P_{(i)}], \quad (2.100)$$

where $\boldsymbol{\rho}_{(i)}$ represents the vector of values for all FE integration points at which we are evaluating $\rho_{(i)}(\mathbf{X})$. The expression for $\mathbf{f}_{(i)}^{(a)}$ given in (2.95) suggests an alternative form for the quantity $P_{(i)}$ requiring a simpler calculation of $\mathbf{R}_{(i)} \cdot \mathbf{f}_{(i)}^{(a)}$ in place of $\mathbf{f}_{(i)}^{(a)} \cdot \mathbf{f}_{(i)}^{(a)}$ since $\mathbf{f}_{(i)}^{(a)}$ is collinear with $\mathbf{R}_{(i)}$,

$$P_{(i)} = \frac{1}{2} \sum_{a \in \tilde{\mathcal{N}}_i} \left(\mathbf{R}_{(i)} \cdot \mathbf{f}_{(i)}^{(a)} \right)^2. \quad (2.101)$$

The number of independent equations we can extract from $P_{(i)}$ is determined by the number of spatial dimensions and the number of nodes in $\tilde{\mathcal{N}}_{(i)}$. We cannot uniquely determine $\boldsymbol{\rho}_{(i)}$ if it possesses more unknowns. If we introduce unknowns at the integration points used for the finite element calculations, the number of unknowns is determined by the number of elements covering $\tilde{\Omega}_{0(i)}$ and the number of integration points per element. Clearly, the number of unknowns may generally exceed the number of independent equations. Therefore, it may be necessary to introduce an additional term into either (2.99) or (2.101) to ensure the solution of $\boldsymbol{\rho}_{(i)}$. One possible addition is a term that tends to smooth the bond density distribution, resulting in the modified function

$$P_{(i)}^* = \frac{1}{2} \sum_{a \in \tilde{\mathcal{N}}_i} \left(\mathbf{R}_{(i)} \cdot \mathbf{f}_{(i)}^{(a)} \right)^2 + \frac{1}{2} \kappa \int_{\tilde{\Omega}_{0(i)}} \nabla_{\mathbf{X}} \rho_{(i)} \cdot \nabla_{\mathbf{X}} \rho_{(i)} d\Omega, \quad (2.102)$$

and $\rho_{(i)}$ satisfies

$$\min_{\boldsymbol{\rho}_{(i)}} [P_{(i)}^*], \quad (2.103)$$

where κ is a parameter used to adjust the influence of the gradient regularization. This method is known as Tikhonov regularization and is commonly found in the literature [26]. The stability of determining $\boldsymbol{\rho}_{(i)}$ for general cases of overlap between the crystal and mesh needs to be investigated further.

In summary, the continuum strain energy for overlap elements is calculated using a modification of the Cauchy-Born rule that includes bond density correction functions, $\rho_{(i)}(\mathbf{X})$. These functions are determined by solving the minimization problems given in equations (2.102) and (2.103) using the expression for $\mathbf{f}_{(i)}^{(a)}$ given in equation (2.95). For our analyses, we use a Newton solution scheme to solve for the vector of values $\boldsymbol{\rho}_{(i)}$ subject to the constraint that for each value, $0 \leq \rho_{(i)} \leq 1$.

2.6 Implications of the overlap correction

Examination of (2.95) allows us to quantify the magnitude of the fictitious force on nodes in $\tilde{\mathcal{N}}_{(i)}$ if no correction is made to the Cauchy-Born rule. In this case, the uncorrected bond density function is $\rho_{(i)}(\mathbf{X}) = 1$ for all $i = 1, \dots, n_b$, representing full density for all bond families n_b . Using (2.97) with the uncorrected bond density function, we find

$$\mathbf{f}_{(i)}^{(a)} = \mathbf{R}_{(i)} \sum_{\substack{\beta: \mathbf{X}^{(\beta)} \in \tilde{\Omega}_{0(i)}^{(a)}, \\ \mathbf{R}^{(\alpha\beta)} = \mathbf{R}_{(i)}}} N^{(a)}(\mathbf{X}^{(\beta)}). \quad (2.104)$$

From (2.94) and (2.104), we can determine the total fictitious force acting on nodes that bound the overlap region as a result of uncorrected overlap between the continuum and the underlying crystal.

Interpretation of the expression given in (2.95) is difficult given that integration of the shape function gradient occurs over two distinct domains, $\bar{\Omega}_{0(i)}^{(a)}$ and $\tilde{\Omega}_{0(i)}^{(a)}$. However, detailed examination enables us to conclude that the total force on node (a) from bond type (i) comes from a combination of forces exerted on ghost atoms within the overlap element from free atoms and the force on the node exerted by the continuum to compensate for the bonds that are not present. At equilibrium, $\mathbf{f}_{(i)}^{(a)} = \mathbf{0}$. It is interesting to note that this result can also be obtained naively by omitting cross terms between free nodes and ghost atoms,

$$\mathbf{R}_{(i)} \sum_{\substack{\beta: \mathbf{X}^{(\beta)} \in \tilde{\Omega}_{0(i)}^{(a)}, \\ \mathbf{R}^{(\alpha\beta)} = \mathbf{R}_{(i)}}} N^{(a)}(\mathbf{X}^{(\beta)}) \rightarrow \mathbf{0}, \quad (2.105)$$

and by using the uncorrected Cauchy-Born rule ($\rho_{(i)} = 1$) within the overlap elements,

$$\frac{1}{V_0} [\mathbf{R} \otimes \mathbf{R}]_{(i)} \left[\int_{\bar{\Omega}_{0(i)}^{(a)}} \frac{\partial N^{(a)}}{\partial \mathbf{X}} d\Omega + \int_{\tilde{\Omega}_{0(i)}^{(a)}} \rho_{(i)} \frac{\partial N^{(a)}}{\partial \mathbf{X}} d\Omega \right] \rightarrow \frac{1}{V_0} [\mathbf{R} \otimes \mathbf{R}]_{(i)} \int_{\Omega_0^{(a)}} \frac{\partial N^{(a)}}{\partial \mathbf{X}} d\Omega = \mathbf{0}. \quad (2.106)$$

In effect, decoupling the atomistic and continuum analyses is accomplished by eliminating the influence of ghost atoms on free nodes that border overlap elements combined with treating the overlap element with the constitutive model derived from the normal Cauchy-Born rule as though the overlap element has no underlying crystal lattice present. Thus, the correct solution for the displacement field is obtained without regard to force cross terms. It is important to realize that **both** of the actions discussed above must be done for this to be true. If ghost atom influence is eliminated and a corrected Cauchy-Born rule is used, or vice-versa, the solution obtained will be incorrect.

2.7 One-dimensional examples

To demonstrate the key features of the coupling approach, consider the patch of a one-dimensional coupled system shown in Figure 2.4. The patch consists of the complete support of node (a), which is comprised of two elements of dimension h , and a single pair bond of length R . For this system, bonds exist only between nearest neighbor atoms. Hence, the subscript (i) may be omitted since only a single type of atomic bonds exists for all atoms. The nodal shape function and derivative for this case is given by

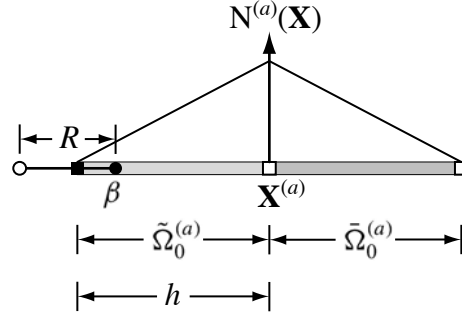


Figure 2.4: Patch from a one-dimensional coupled system.

$$N^{(a)}(X) = \begin{cases} 1 - \frac{X^{(a)} - X}{h} & X \in \tilde{\Omega}_0^{(a)}, \\ 1 + \frac{X^{(a)} - X}{h} & X \in \bar{\Omega}_0^{(a)}, \\ 0 & \text{elsewhere,} \end{cases} \quad \text{and} \quad \frac{\partial N^{(a)}(X)}{\partial X} = \begin{cases} \frac{1}{h} & X \in \tilde{\Omega}_0^{(a)}, \\ -\frac{1}{h} & X \in \bar{\Omega}_0^{(a)}, \\ 0 & \text{elsewhere,} \end{cases} \quad (2.107)$$

respectively. Using (2.95) and setting $f^{(a)} = 0$, we find the optimal bond density must satisfy

$$\int_{\tilde{\Omega}_0^{(a)}} \rho dX = h (1 - N^{(a)}(X^{(\beta)})) \quad \text{for} \quad X^{(a)} - h \leq X^{(\beta)} \leq X^{(a)} - h + R, \quad (2.108)$$

which holds for

$$\rho = 1 - N^{(a)}(X^{(\beta)}) \quad (2.109)$$

over $\tilde{\Omega}_0^{(a)}$. Note that in this case, the problem of determining ρ does not have a unique solution if ρ is discretized with more than one unknown and more than one integration point is used to evaluate the left hand side of (2.108). For this example, we can see how the bond density simply compensates for the overlap in the continuum and the underlying lattice. As mentioned above, attributing fractions of a bond's energy to certain domains becomes ambiguous in multiple dimensions for which the general method for determining the bond density distribution becomes necessary. This point was not addressed by the authors of [12], who examined only one-dimensional chains of atoms with nearest neighbor interactions.

Figure 2.5 shows the displacements of a coupled system composed of five nodes and five atoms. This analysis, and all subsequent simulations shown in this paper, was performed using a research-oriented program capable of both finite element analysis and atomistic simulation that was developed at Sandia National Laboratories [27]. The sets of nodes with free and prescribed displacements are $\mathcal{N} = \{4, 5\}$ and $\hat{\mathcal{N}} = \{1, 2, 3\}$, respectively. The sets of atoms with free and prescribed displacements are $\mathcal{A} = \{1, 2, 3, 4\}$ and $\hat{\mathcal{A}} = \{5\}$, respectively. The chain of atoms is bound by the quadratic potential $\varphi(r) = \frac{1}{2}k(r - R)^2$ acting between nearest neighbors with $R = \frac{1}{2}$. From the Cauchy-Born rule, the elements, with dimension $h = 1$, have an initial modulus $E = Rk$. To demonstrate the effect of

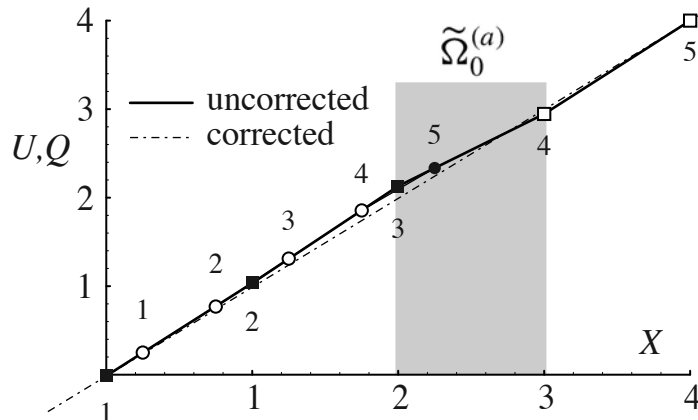


Figure 2.5: Homogeneous displacements of the 1-dimensional coupled system for both the corrected bond density of $\rho(X) = \frac{3}{4}$ and the uncorrected bond density of $\rho(X) = 1$. Atom and element numbers are given within the figure by the digit shown above or below, respectively, the corresponding part.

the bond density function, we prescribe $\rho(X) = 1$, meaning no correction is made for the overlap of elements and bonds between node 4 and atom 5. The system is loaded with the prescribed displacements $Q^{(1)} = X^{(1)} = \frac{1}{4}$ and $U^{(5)} = X^{(5)} = 4$, so that the homogeneously deformed shape should have a constant slope of 1. The results plotted in Figure 2.5 show the coupled system does not deform homogeneously. The reduced slope in the element 3—4 is the result of increased stiffness of this region over the other parts of the system resulting from the overlap between bonds and elements. The slopes of the atomic chain 1—2—3—4 and element 4—5 are the same indicating the stiffness produced by the Cauchy-Born model is consistent with the lattice. Finally, we note that nodes 1, 2, and 3 lie on a straight line defined by displacements of the atomic chain 1—2—3—4, indicating that the method used to transfer the atomistic displacement to the nodes in $\hat{\mathcal{N}}$, an L_2 projection in this case, is able to reproduce homogeneous displacements exactly. In order to reproduce the homogeneous solution, we must define $\rho(X) = \frac{3}{4}$ for $2 \leq X \leq 3$, as given by (2.109).

The simple example shown above of the homogeneously stretched one-dimensional atomic chain was performed using an L_2 projection method. Because of the computational cost, we seek alternatives to calculating $\mathbf{M}_{\hat{\mathcal{U}}\hat{\mathcal{U}}}^{-1}$ associated with the L_2 projection of atomistic displacements to the nodes in $\hat{\mathcal{N}}$. One simple alternative is to use a diagonal approximation to $\mathbf{M}_{\hat{\mathcal{U}}\hat{\mathcal{U}}}$, which has the structure of a finite element mass matrix. A number of “lumping” methods has been developed for the solution of dynamic problems with explicit time integration schemes. Figure 2.6 shows the displacements for a coupled system with $\mathbf{M}_{\hat{\mathcal{U}}\hat{\mathcal{U}}}$ diagonalized using Hinton’s method [28]. The results show that although all of the nodes in $\hat{\mathcal{N}}$ and atoms in \mathcal{A} follow the homogeneous solution $Q(X) = U(X) = X$, the nodes and

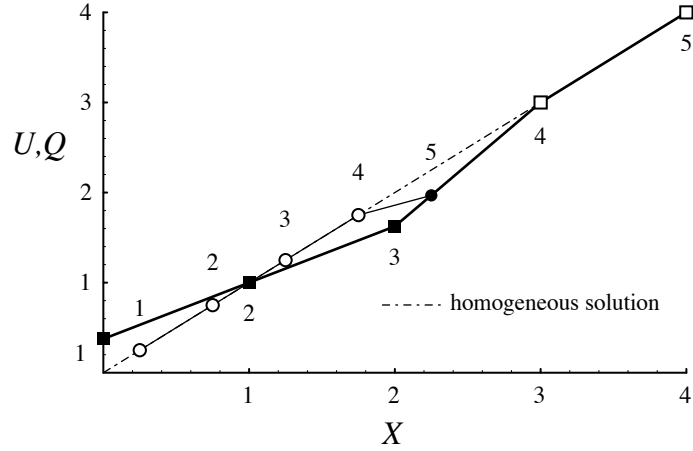


Figure 2.6: Displacements of a coupled system using a diagonal approximation in the L_2 projection.

atoms with prescribed motion, those in $\hat{\mathcal{N}}$ and $\hat{\mathcal{A}}$, respectively, do not follow the homogeneous solution. This solution is produced by defining the bond density $\rho(X) = \frac{6}{11}$ for $2 \leq X \leq 3$ and by weighting the energy of bond 4—5 as $\frac{16}{7}$, which were determined by requiring $\frac{\partial \Pi}{\partial Q^{(4)}} = 0$ and $\frac{\partial \Pi}{\partial U^{(4)}} = 0$ for the system with all active displacements following a homogeneously deformed solution. The additional weight of the 4—5 bond is required because the approximate L_2 projection, using the diagonalized form of $\mathbf{M}_{\hat{\mathcal{U}}\hat{\mathcal{U}}}$, is unable to reproduce homogeneous solutions exactly. The displacement field across nodes 1, 2, and 3 does vary homogeneously, but not with the correct slope. Consequently, atom 5 fails to lie on the solution with homogeneous deformation since it is constrained to lie on the solution between nodes 3 and 4. Further testing with this small case showed that no diagonal matrix could reproduce the homogeneous strain field exactly. These results enable us to conclude that use of diagonalized $\mathbf{M}_{\hat{\mathcal{U}}\hat{\mathcal{U}}}$ is not recommended. Either the original, L_2 projection method or the MLS alternative should be used.

We also examine a 1-D atomic chain with atoms subject to multiple neighbor interactions. For this example, we use the Lennard-Jones potential [29, 30] that has been truncated [31] such that each atom interacts with all of its neighbors out to the 5th nearest neighbor. In this simulation, the chain has been given free boundary conditions on the atoms at either end and the system has been relaxed using a conjugate gradient, energy minimization algorithm. Figure 2.7 shows the bond density correction calculated for each of the five different bond types. For clarity, the crystal itself is also shown with the same symbols as in Figure 2.1 used for free and prescribed atoms and nodes. For the example shown, the four outer-most atoms on either end are free atoms while the remaining atoms are ghost atoms. In this example, it is clear how the volume $\tilde{\Omega}_{0(i)}^{(a)}$ differs with regard to each different bond type (i). It is also interesting to note that for this small system, ghost atoms are required within all elements

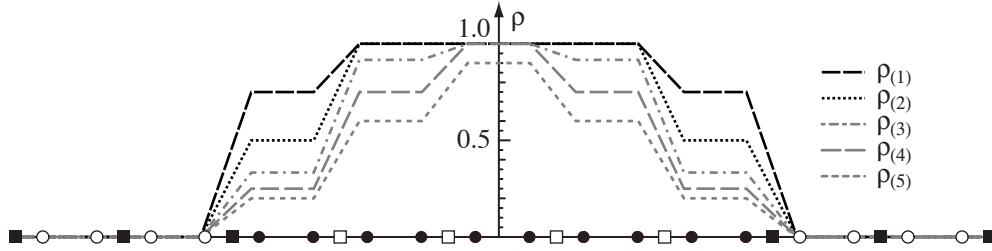


Figure 2.7: $\rho_{(i)}(\mathbf{X})$ for a 1-D atomic chain using a 5th nearest neighbor Lennard-Jones potential.

in the interior due to the long range of the interatomic potential. Even within the center element $\rho_{(5)}$, the bond density correction associated with the bonds between an atom and its 5th nearest neighbors, never reaches the value of unity as ghost-free bonds are present. However, if the chain were made longer, we would see elements for which $\rho_{(i)} = 1$ for all 5 bond families, and ghost atoms could be omitted. In other words, the overlap region would essentially remain the same size that it is in Figure 2.7 while more and more of the system can be modeled using pure continuum elements. Figure 2.8 shows atomic displacements for two such longer 1-D atomic chains. In Figure 2.8(a), the ratio of element size to atomic spacing is 2:1 and the system contains 26 atoms, 14 nodes and 13 elements. In Figure 2.8(b), this ratio is 6:1 and the system contains 30 atoms, 6 nodes and 5 elements. In both figures, we see that without any free atoms on the surface, the system displays zero relaxation, and as successively more free atoms are used at the outer layers, the displacement field converges to that of a pure atomistic 1-D atomic chain. For the 2:1 ratio, this convergence occurs for 4 or more layers of free atoms while for the 6:1 ratio, it occurs for 6 layers of free atoms. Thus, the ratio of element size to atomic spacing, as well as the interaction range of the interatomic potential, affects how many layers of free atoms are needed to achieve this convergence.

2.8 Two-dimensional examples

We next examine the 2-dimensional analog of the homogeneous deformation example given in the previous section. A rectangular region covered by a finite element mesh composed of four-node elements contains a limited region of atoms from a hexagonal crystal lattice, as shown in Figure 2.9(a). These atoms interact through a nearest neighbor, quadratic potential. This region is homogeneously deformed by stretching the system's boundaries in the horizontal direction, as shown in Figure 2.9(b). As mentioned in section 2.6, this case proves to be unaffected by whether the cross terms in equations (2.26) and (2.27) are included or not. For homogeneous deformation, the force coupling cross term between projected nodes and

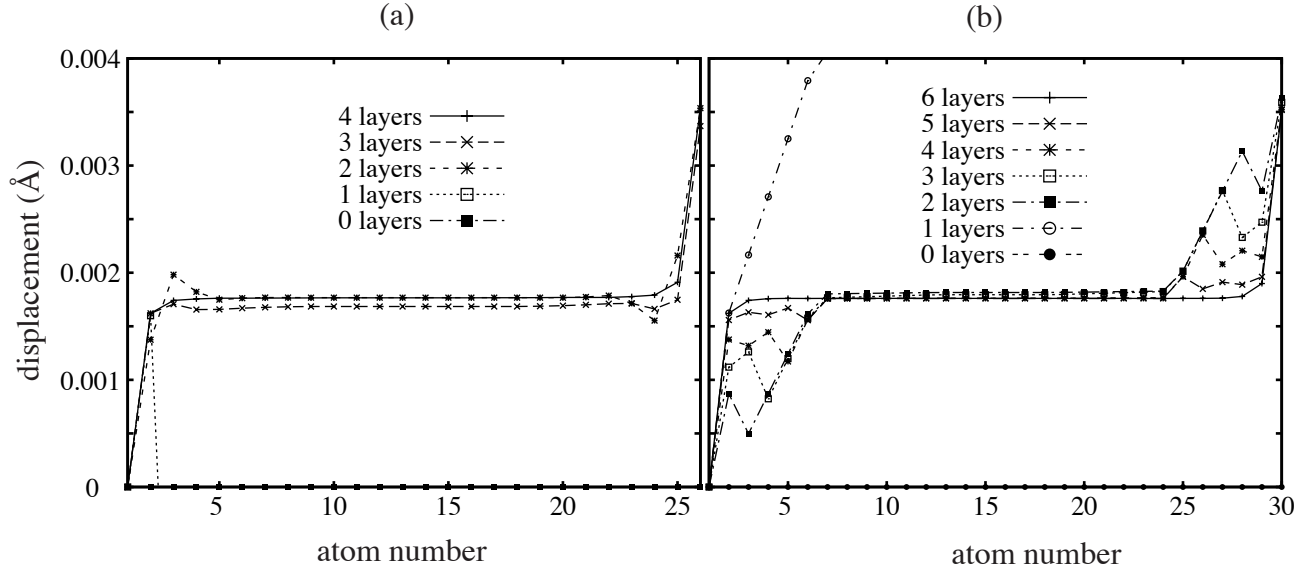


Figure 2.8: Displacements for the relaxation of a free, 1-D atomic chain using a 5th nearest neighbor Lennard-Jones potential. Each curve represents a different number of layers of free atoms used at the chain’s surfaces. The ratio of element size to atomic spacing is (a) 2:1 and (b) 6:1.

free atoms disappears,

$$\mathbf{R}_{\hat{\mathbf{U}}} = \mathbf{0} \rightarrow \mathbf{R}_{\mathbf{Q}} = \frac{\partial \Pi_{\mathbf{Q}}}{\partial \mathbf{Q}} - \mathbf{F}_{\mathbf{Q}} = \mathbf{0}. \quad (2.110)$$

This decouples the displacement of the atoms from the displacement of the overlaying finite element mesh. Indeed, the correct displacement field for the free nodes is obtained if one assumes

$$\mathbf{R}_{\hat{\mathbf{Q}}} = \mathbf{0} \rightarrow \mathbf{R}_{\mathbf{U}} = \frac{\partial \Pi_{\mathbf{U}}}{\partial \mathbf{U}} \Big|_{\rho=1} - \mathbf{F}_{\mathbf{U}} = \mathbf{0}. \quad (2.111)$$

In other words, the correct solutions for both the atomic and nodal displacement fields were obtained by treating them as separate problems. Their only connection is to use the Cauchy-Born rule to create the same material properties for the continuum as for the atomistic system, and the kinematic coupling used for interpolation and projection. Once again, it is important to realize that (2.111) results from eliminating the cross terms to calculate forces on free nodes due to ghost atoms **and** by setting bond densities, $\{\rho_{(i)}\}$, to unity. Only by omitting both coupling mechanisms is the correct FE solution realized. In addition, this decoupling of the problem is possible because the interatomic potential used is a nearest neighbor interaction only. Thus, the atomic crystal shown in Figure 2.9 exhibits no surface relaxation and the Cauchy-Born model based on the same interatomic potential displays the same response as the actual crystal. For longer-ranged potentials, surface relaxation would

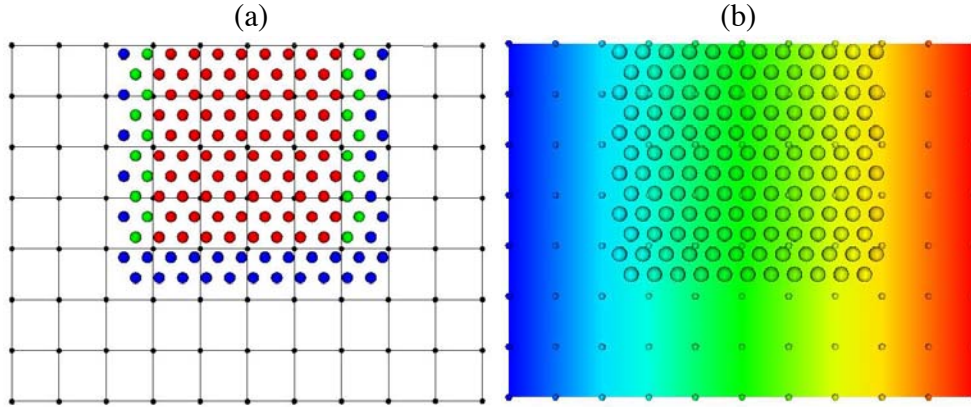


Figure 2.9: (a) The 2-dimensional coupled system consisting of a rectangular mesh of square elements and a portion of a hexagonal lattice. Atoms are colored according to whether they are free (red) or ghost (green and blue). (b) The 2-d system homogeneously stretched in the horizontal direction. Color denotes the magnitude of stretch from zero (blue) to the highest value (red).

occur and the deformations of the decoupled atomistic and continuum systems would no longer coincide.

A case for which the cross terms are important, and the correction for energy of overlapping elements is required to obtain the correct displacement solution, is one in which inhomogeneous deformation occurs, such as the surface relaxation of a cross-section of nanowire. Figure 2.10(a) shows a system composed of a hexagonal lattice with free surfaces overlapped by a square FE mesh. For the coupled system, the atoms that lie within the outer layer of elements are free atoms while all other elements contain ghost atoms. For this example, our potential is the Lennard-Jones potential [29, 30] that has been shifted and truncated [31] such that an atom that interacts with all of its neighbors out to the 3rd nearest neighbor is equivalent to an atom within a bulk crystal. The system relaxes outward as shown in Figure 2.10(b). The coupled system (red atoms) can be directly compared with a system simulated purely with atomistics, (green atoms). Agreement is very good, but not perfect due to the severe inhomogeneous deformation at the corners. Once again, the small system size necessitated the placement of ghost atoms within all elements comprising the system. For larger systems, there would exist a minimum coverage of ghost atoms beyond which placement of additional ghost atoms would be unnecessary. However, for moderate size systems placing atoms everywhere would enable adaptive lattice extension (contraction) to be easily implemented. All one would have to do is to switch the character of the atoms from ghost to free (free to ghost) to grow (shrink) the atomic crystal region and then re-determine the character, prescribed or free, for the system's nodes.

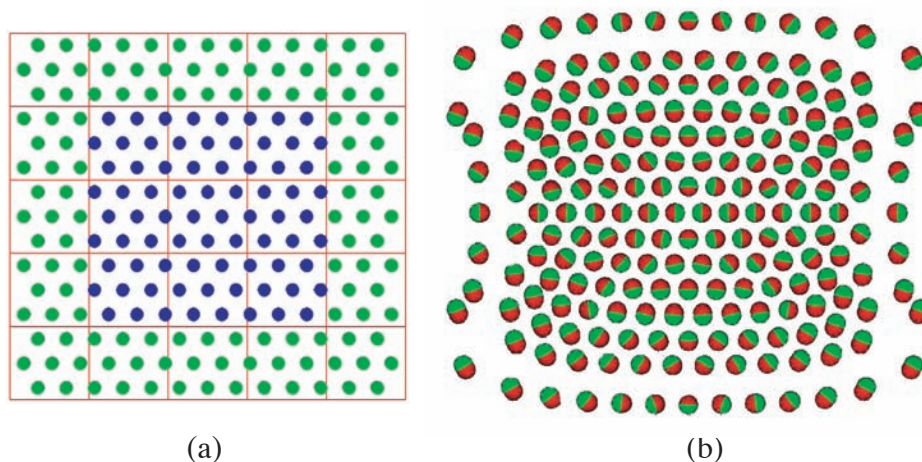


Figure 2.10: (a) A 2-D, hexagonal lattice with free surfaces composed of free (green) and ghost (blue) atoms. The overlapping square FE mesh is shown in red. (b) The relaxed configuration of (a) for the coupled system (red) and a system treated purely with atomistics (green). Displacements are magnified by a factor of 200.

This two-dimensional surface relaxation problem also enables us to investigate the influence of the overlapping mesh on the coupled solution. Specifically, we examine a system in which triangular elements are used instead of square ones. The mesh for this system is shown in Figure 2.11(a). We notice that this system contains fewer atoms per element (202 atoms overlapped by 52 elements) as compared with the square mesh (202 atoms overlapped by 25 elements). Figure 2.11(b) shows the relaxed system with displacements magnified by a factor of 200 for both the coupled (red atoms) and purely atomistic (green atoms) systems. For this case, the displacements fields do not agree as well as for the square mesh. The primary reason for the deficiency of the triangular mesh system is that while square elements use four integration points per element for the FE calculation, triangular elements only use one point per element. Thus, triangular elements can only represent strains that are constant over the element. The use of a single integration point reduces the spatial discretization of $\{\rho_{(i)}\}$ and results in a lower resolution representation of the coarse scale portion of the solution. This leads to a loss of accuracy in the calculation of continuum field variables, and produces a stiffer overall response for the element.

2.9 Three-dimensional examples

A similar surface relaxation simulation is performed for the 3-dimensional system composed of a cube of atoms. This cube contains a face-centered-cubic crystal of 32,000 atoms, and

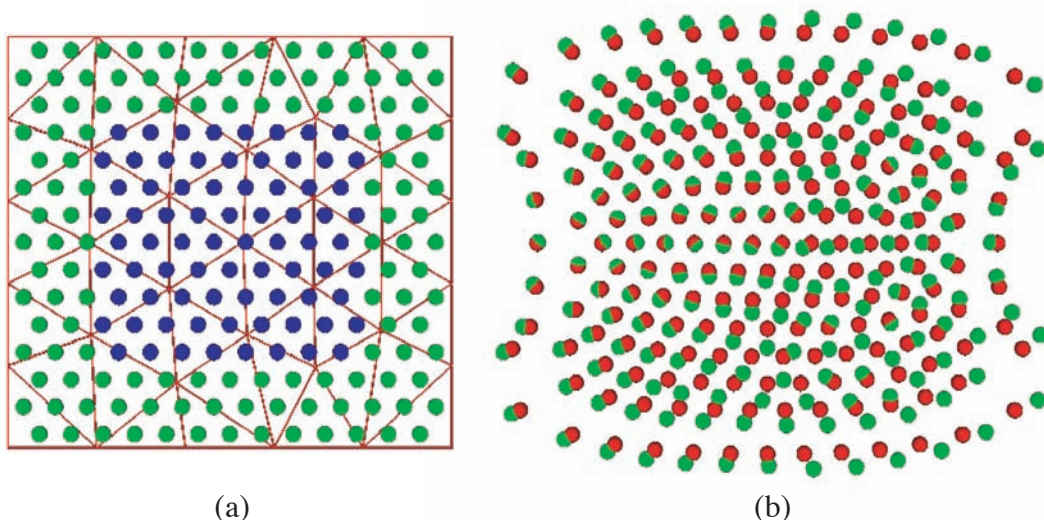


Figure 2.11: (a) A 2-D, hexagonal lattice with free surfaces composed of free (green) and ghost (blue) atoms. The overlapping triangular FE mesh is shown in red. (b) The relaxed configuration of (a) for the coupled system (red) and a system treated purely with atomistics (green). Displacements are magnified by a factor of 200.

atoms interact with a 5th nearest neighbor Lennard-Jones potential with parameters suitable for the simulation of gold. This potential is given by the expression

$$\varphi(r^{\alpha\beta}) = \varphi_{\text{LJ}}(r^{\alpha\beta}) - \varphi_{\text{LJ}}(r^c) - [r^{\alpha\beta} - r^c] \varphi'_{\text{LJ}}(r^c), \quad (2.112)$$

where

$$\varphi_{\text{LJ}}(r) = 4\epsilon \left[\left(\frac{\sigma}{r} \right)^{12} - \left(\frac{\sigma}{r} \right)^6 \right], \quad (2.113)$$

$r^{\alpha\beta} = |\mathbf{x}^{(\alpha)} - \mathbf{x}^{(\beta)}|$, $\epsilon = 0.567895$ eV, $\sigma = 2.623117$ Å and $r^c = 2.63\sigma$. Magnified displacements for half of the cube are shown in Figures 2.12(a), (b), and (c) for the purely atomistic system, coupled atomistic-continuum system with hexahedral elements, and coupled system with tetrahedral elements, respectively. The ratio of element size to atomic spacing is approximately the same for calculations using the hexahedral (5.34:1) and tetrahedral (5.33:1) elements. In Figure 2.12, atoms are colored according to their potential energy with red denoting the highest value for all atoms within the individual system and blue denoting the lowest value. Hence, in Figure 2.12(a), the highest potential energy atoms are found at the cube corners and along the cube edges and are therefore colored red and yellow, respectively. The interior atoms possess the bulk potential energy of gold atoms and are colored dark blue. In Figure 2.12(b), the red and yellow colors are assigned to interior ghost atoms as they do not have any potential energy attributed to them unless bonded to free atoms in the outer layers. It is still observed that free atoms sufficiently far from the surface have

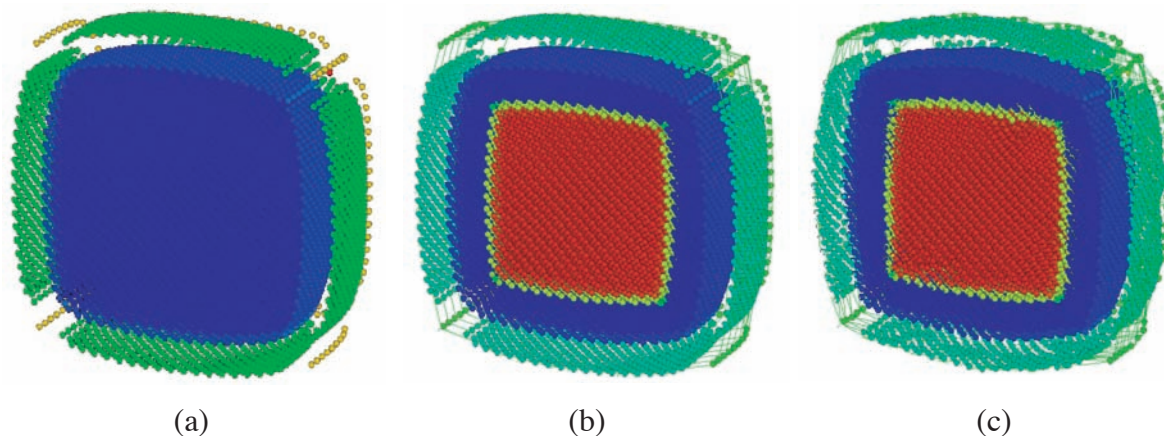


Figure 2.12: One-half of a 3-D cube modeled with (a) pure atomistics, (b) coupled atomistics-continuum using a hexahedral element mesh, and (c) coupled atomistics-continuum using a tetrahedral element mesh. Displacements are magnified by a factor of 200.

potential energies equal to the bulk cohesive energy for gold, and that surface, edge and corner atoms have higher potential energies. Comparison of potential energies for the free atoms in the coupled system with the same respective atoms in the purely atomistic system shows agreement to the fourth significant figure. Atomic potential energy is dominated by the creation of surfaces, while a change in energy due to relaxation is a secondary effect.

Figure 2.12(c) shows similar values of energies to those found in Figure 2.12(b), again agreeing with the purely atomistic system's energies to the fourth significant figure. However, the relaxed configuration with the tetrahedral mesh does not display the same level of accuracy as with the hexahedral mesh. Once again, this loss of accuracy is due to the hexahedral elements possessing the ability to represent varying strain while the tetrahedral elements can only represent constant strain.

Further comparison between the purely atomistic and coupled systems can be made through examination of the stress field created by the surface relaxation. Figure 2.13 shows the variation of the hydrostatic stress for nodes along a line passing through the middle of the cube between opposing faces. The different curves correspond with the numbers of surface layers of free atoms, with 20 layers corresponding to the purely atomistic system. It is observed that when 6 or more atomic layers are used within the atomic region, the coupled system essentially matches the stress field obtained with pure atomistics, especially with regard to the value of tensile stress within the outer layers of the cube. The interior compressive stress also agrees very well, especially for the use of 6 or 8 atomic layers. For comparison, we can also examine the same hydrostatic stress curves produced for system coupled only through kinematics. For these analyses, neither the cross terms nor the bond

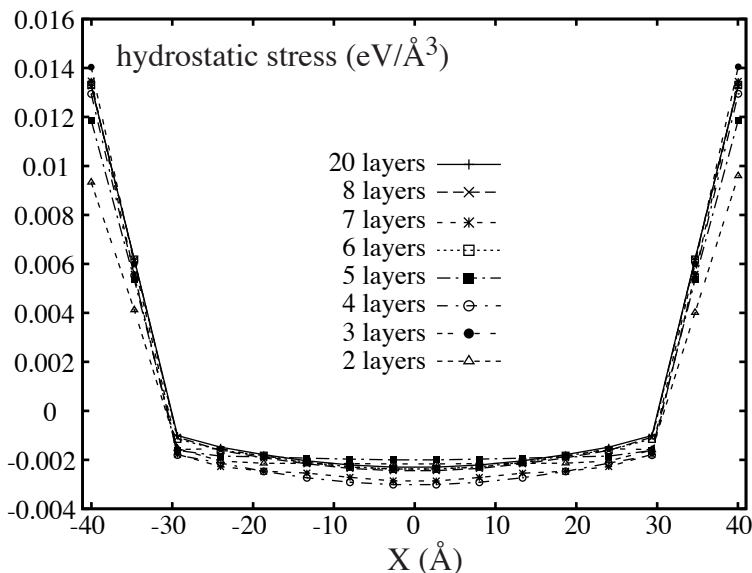


Figure 2.13: Hydrostatic stress for nodes along a line passing through the middle of the relaxed cube. The legend refers to the number of layers of free atoms used for the outer surface of the crystal.

density corrections to the Cauchy-Born rule were used. As shown in Figure 2.14, we observe that while it is again the case that using 6 or more atomic layers comes closest to the pure atomistic solution and the interior compressive stress agrees best when using 6 or 8 atomic layers, this agreement is not as good as when force coupling mechanisms are implemented. This is made obvious by the much wider range of values of compressive stress for the nodes within the cube.

2.10 Summary

We have presented a formulation for an atomistic-to-finite element coupling method for quasistatic analysis. Our quasistatic coupling approach is comprised of three components:

- kinematics - the description of how displacements are transferred from nodes and atoms in \mathcal{N} and \mathcal{A} to nodes and atoms in $\hat{\mathcal{N}}$ and $\hat{\mathcal{A}}$.
- coupled equilibrium equations - equations derived from the total energy of the coupled system incorporating the kinematics of the coupling in displacements.

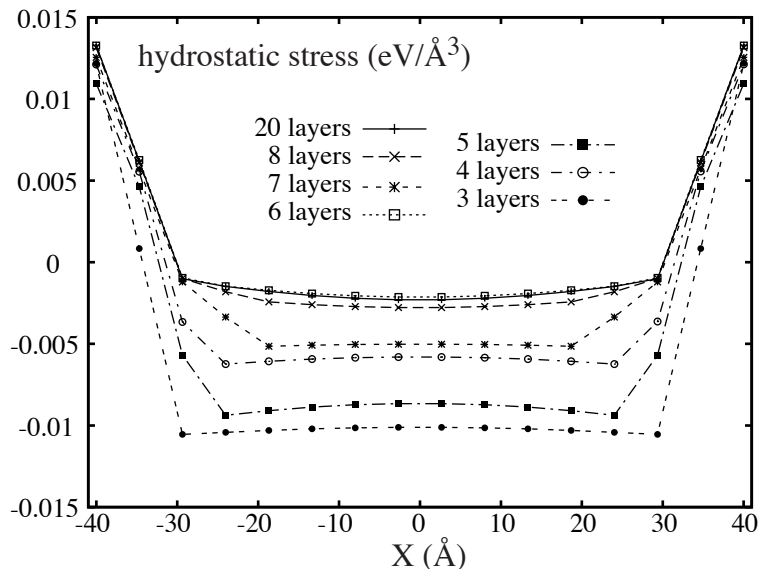


Figure 2.14: The same curves as in Figure 2.13 for a system coupled only through kinematics and use of the Cauchy-Born rule (no force coupling mechanisms used).

- generalized Cauchy-Born - modifications to the usual Cauchy-Born rule needed to compensate for regions of overlap between the continuum and the underlying lattice.

The moving least squares field construction, like that provided by RKPM, appears the most promising for the transfer of atomistic displacements to the nodes in $\hat{\mathcal{N}}$. The formulation provides a method for “fitting” a displacement field over atoms in a given region that can be constructed to reproduce a selected order of polynomials exactly. This property can be used to guarantee that a homogeneous deformation field is transferred to the nodes exactly. Moreover, RKPM has well-defined spectral properties, especially when calculated over a regular set of points, such as a lattice. These properties will allow us to characterize exactly which scale or wavelength of information is transferred to the finite element nodes and which ones need to be accommodated in some other fashion.

The most significant outcome of this work has been the development of a generalized Cauchy-Born procedure for use in finite elements with a limited amount of underlying crystal lattice. The method does suggest it should yield better performance with mesh refinement. The improved results would be the result not only of the finer scale in the finite element basis function, but also as a result of higher resolution in the discretized bond density function. Note that this function only needs to be determined once, over the undeformed configuration, for a given system geometry. The simple one- and two-dimensional examples provided show that the solution may not be unique with the current method of solution.

We do observe that the approach described in this paper, specifically the inclusion of force cross terms within the equilibrium equations and the bond density corrections to the Cauchy-Born rule, does possess good stability with regard to yielding a numerical solution. Omission of these features often results in our energy minimization algorithms failing to converge to any solution for many of the systems described in this paper. This failure is highly dependent on the orientation of the mesh with respect to the underlying atomic lattice and the size of lattice region used. Under limited conditions, the issue of overlap correction can be addressed by terminating the atomistic crystal in specific ways within the mesh. This approach has allowed previous efforts in atomistic-continuum coupling to produce seemingly accurate results. Our development and inclusion of these features eliminates this dependency, and is more generalized for the proper treatment of multi-dimensional systems and longer range potentials.

A remaining concern with this approach, to be addressed in future work, regards the quantification of solution errors obtained with coupled systems. We have minimized the error through our use of cross terms within the equilibrium equations and the bond density corrections to the Cauchy-Born rule. However, several approximations were made to obtain solutions for those same bond density corrections, including the use of a limited number of integration points at which the bond densities $\rho_{(i)}$ are evaluated. Whether the error these approximations introduce to our solution is much smaller than error eliminated by our approach remains an unanswered question.

Several areas for further development of our approach have been identified. Currently, we are working to parallelize the algorithms discussed in this paper for applicability of our approach to large systems. We also plan to develop expressions for the bond density corrections that correspond to multi-body types of interatomic potentials such as the Embedded Atom Method [32], used for modeling FCC and BCC crystals, and the Stillinger-Weber potential [33], used for modeling silicon and other materials with the diamond cubic crystal structure. Finally, the methodology presented in this paper will be adapted to analyze coupled dynamic systems. The bond density corrections developed here will still be used to compute the potential energy portion of the system's Hamiltonian, but more thought will be required with regard to the partitioning and calculation of the kinetic energy portion.

This page intentionally left blank.

Chapter 3

Evaluation of Stress in Atomistic Simulation

Principle Authors: J.A. Zimmerman, E.B. Webb III, J.J. Hoyt, R.E. Jones, P.A. Klein and D.J. Bammann

Atomistic simulation is a useful method for studying material science phenomena. Examination of the state of a simulated material and the determination of its mechanical properties is accomplished by inspecting the stress field within the material. However, stress is inherently a continuum concept and has been proven difficult to define in a physically reasonable manner at the atomic scale. In this paper, an expression for continuum mechanical stress in atomistic systems derived by R.J. Hardy is compared with the expression for atomic stress taken from the virial theorem. Hardy's stress expression is evaluated at a fixed spatial point and uses a localization function to dictate how nearby atoms contribute to the stress at that point; thereby performing a local spatial averaging. For systems subjected to deformation, finite temperature, or both, the Hardy description of stress as a function of increasing characteristic volume displays a quicker convergence to values expected from continuum theory than volume averages of the local virial stress. Results are presented on extending Hardy's spatial averaging technique to include temporal averaging for finite temperature systems. Finally, the behavior of Hardy's expression near a free surface is examined, and is found to be consistent with the mechanical definition for stress.

3.1 Introduction

An important issue of multiscale mechanical modeling is the development of definitions for continuum variables that are calculable within an atomic system. Connections between continuum variables and microscopic quantities originates from long-wavelength elasticity theory

or long-time, equilibrium ensemble averages giving rise to macroscopic balance equations. The instantaneous atomic contributions to these averages do not have the same physical interpretation as the corresponding “point-wise” continuum quantities. A classic example is the Cauchy, or true stress and the ensemble stress defined by the virial theorem (VT). The VT was developed by Clausius [34] and Maxwell [35, 36] to determine the stress field applied to the surface of a fixed volume containing interacting particles. Although the expression developed is a time and spatial averaged quantity, it is often inappropriately used to obtain a point-wise, local virial stress. This results in erroneous estimates of stress for simple situations. An example of this can be seen for a crystal with free surfaces, as done by Cheung and Yip [37] who showed that the atoms within the outer layers of the crystal possessed non-zero values for the normal component of the stress tensor. Nevertheless, the virial stress expression has become an invaluable computational diagnostic tool for evaluating simulations of materials science phenomena such as void formation during thin film growth [38], internal stress fields due to inhomogeneous precipitates [39] and finite deformation leading to atomic-scale plasticity [40]. A comprehensive review on the derivation and application of the VT can be found in the manuscript by Marc and McMillan [41].

There have been several efforts to correct the misuse of the VT by developing definitions for stress that satisfy the equation for balance of linear momentum for a dynamic continuum. Irving and Kirkwood [42] were the earliest to use expressions for mass, momentum and energy densities that are defined for a spatial point at an instant of time based on the statistical distribution of particles near to the point chosen. Their resulting formula for stress contains several expressions that require integration over phase space of quantities weighted by the Dirac delta function and a probability distribution function. One of these quantities is an infinite-series expansion of differential operators. While their pioneering effort is indeed noteworthy, the end product is difficult to implement within a standard particle simulation. Schofield and Henderson [43] also noted that the expression developed by Irving and Kirkwood is non-unique due to the taking of an ensemble average in regions of inhomogeneity.

A different approach to deriving a local stress tensor was taken by Tsai [44], who used considerations of forces acting across, and motion through, a spatial boundary to develop an expression for stress within a 1-dimensional atomic chain. Cheung and Yip [37] later revisited this approach to calculate the normal stress on each atomic plane for a relaxed crystal with planar free surfaces. As already mentioned, they showed that the local virial stress expression produces an unphysical oscillation in normal stress for the atomic plane at the free surface and the nearest adjacent planes while their modification of Tsai’s expression correctly yields zero normal stress. This approach has also been used to examine interplanar stress across strained interfaces [45]. While this approach certainly appeals to the mechanical intuition for a definition of stress, their resulting expression is also difficult to implement in a point-wise sense. The examples considered by these authors are 1-dimensional, and it is unclear how to define a local area surrounding a spatial point such that an inhomogeneous

stress field can be correctly determined. Rowlinson and Widom [46] have presented a similar analysis that examines forces between atomic pairs that interact through differential areas. However, their approach uses a known pair correlation function, which in general may not be easily determined, and estimates the kinetic contribution to stress from the equilibrium temperature of the system, which may not be properly defined for some cases.

There have been several more recent attempts to improve upon the approach originally conceived by Irving and Kirkwood. Lutsko [47] derived a stress-like tensor from a local momentum balance equation by the use of Dirac delta functions and transformation into Fourier space. Cormier *et al.* [48] used Lutsko's work to develop an expression for stress that is convenient for calculation within an atomistic simulation. However, this approach is limited for two reasons. First, the use of the integral Fourier transformation assumed a particle system of infinite spatial extent. Cormier *et al.* noted this, and commented that the presence of system boundaries needs to be considered to develop a more rigorous expression that accounts for the role of image defects. Second and more important is the fact that Lutsko used an incorrect formulation of the spatial form of the balance of linear momentum. Equation (1) of reference [47] contains the material time derivative of a momentum density, $\frac{d\mathbf{p}}{dt}$. The proper term for the left hand side of this equation should be a mass density multiplied by the material time derivative of a velocity field, $\rho \frac{d\mathbf{v}}{dt}$. This was pointed out by Zhou [49, 50], who also noted that even if the spatial time derivative, $\frac{\partial \mathbf{p}}{\partial t}$, is used instead of the material time derivative the balance equation is still incorrect (compared to equation (1.2) in [42]) and the resulting expression makes improper use of the momentum terms involving atomic velocities. Recent publications by Zhou and McDowell [51] and Zhou [49, 50] attempted to correct these errors by interpreting mechanical stress as an internal force interaction between material points. They asserted that expressions for stress should only contain terms related to those forces and no terms involving a momentum flux through an arbitrarily defined spatial region. These authors made several insightful points about the nature of stress and virial-like expressions for the stress tensor; however, the expression they derived included a term for an arbitrarily-sized volume containing a single atom.

Among these efforts already discussed is the notable work by Hardy and colleagues [52, 53, 54]. The formalism developed by Hardy bypasses some of the mathematical complexities of Irving and Kirkwood's approach by using a finite-valued and finite-ranged localization function in lieu of the Dirac delta function. This property of having a finite range is also referred to as the function being of compact support. While the range of this function — the characteristic size of the volume that contains atoms contributing to properties at the spatial point chosen — can be selected arbitrarily, the resulting expression for stress contains terms that theoretically remain constant for different size volumes. It can also be shown that several of the expressions already mentioned, including the virial stress, can be recovered by taking Hardy's expression to appropriate limits. In this paper, we review Hardy's formalism and present a computational comparison between Hardy's expression for stress and local volume averages of the virial stress within a FCC crystal. For a bulk crystal, we present

results for a variety of simulated conditions: unstrained and deformed lattices, zero and finite temperatures, and at single instances in time and averages over multiple time steps. Our results show that for all but the most trivial of conditions, the Hardy stress expression is as accurate or more than the virial stress. The value of stress fluctuates with changing characteristic volume for both expressions, and the magnitudes of these fluctuations are minimized by using a larger characteristic volume or by time averaging over a minimum number of time steps. We also present results for the behavior of the stress expression in a crystal with a free surface. It is observed that the effective free surface of a solid does not coincide with the top-most atomic layer, but is instead positioned at a distance beyond which no force interactions can be detected.

3.2 Hardy's Formalism for Atomistic-Continuum Equivalence

Hardy's development started with the spatial forms of the balance of mass, linear momentum and energy for a continuum point[13]:

$$\frac{\partial \rho}{\partial t} = \partial \mathbf{x} \cdot (\rho \mathbf{v}) \quad (3.1)$$

$$\frac{\partial \mathbf{p}}{\partial t} = \partial \mathbf{x} \cdot (\boldsymbol{\sigma} - \rho \mathbf{v} \otimes \mathbf{v}), \quad (3.2)$$

$$\frac{\partial e}{\partial t} = \partial \mathbf{x} \cdot (\boldsymbol{\sigma} \cdot \mathbf{v} - e \mathbf{v} - \mathbf{q}), \quad (3.3)$$

where $\partial \mathbf{x} \equiv \frac{\partial}{\partial \mathbf{x}}$, ρ is mass density, \mathbf{p} is linear momentum density, e is internal energy density consisting of potential, kinetic and thermal contributions, \mathbf{q} is heat flux vector and the material velocity field \mathbf{v} is defined such that $\mathbf{p} = \rho \mathbf{v}$. Hardy then defines the continuum fields of ρ , \mathbf{p} and e as functions of a fixed spatial point \mathbf{x} at time t in terms of atomic positions (\mathbf{x}^α) and velocities (\mathbf{v}^α) by using localization functions, ψ :

$$\rho(\mathbf{x}, t) = \sum_{\alpha=1}^N m^\alpha \psi(\mathbf{x}^\alpha - \mathbf{x}) \quad (3.4)$$

$$\mathbf{p}(\mathbf{x}, t) = \sum_{\alpha=1}^N m^\alpha \mathbf{v}^\alpha \psi(\mathbf{x}^\alpha - \mathbf{x}) \quad (3.5)$$

$$e(\mathbf{x}, t) = \sum_{\alpha=1}^N \left\{ \frac{1}{2} m^\alpha (v^\alpha)^2 + \phi^\alpha \right\} \psi(\mathbf{x}^\alpha - \mathbf{x}) \quad (3.6)$$

Here, m^α and ϕ^α represent the mass and potential energy, respectively, attributed to atom α . The localization function ψ spreads out the properties of the atoms ($\alpha = 1, 2, \dots, N$), and allows each atom to contribute to a continuum property at the position \mathbf{x} at time t . The function ψ has units of inverse volume and $\psi \neq 0$ only in some characteristic volume surrounding the spatial point \mathbf{x} . Hardy has established a few rules with regard to the behavior of ψ :

1. $\psi(\mathbf{r})$ is a normalized function, thus $\int_{\mathcal{R}^3} \psi(\mathbf{r}) d^3\mathbf{r} = 1$.
2. The spatial gradient of the localization function, $\partial_{\mathbf{x}}\psi(\mathbf{x}^\alpha - \mathbf{x})$, is equivalent to the negative of the gradient of ψ with respect to its argument, $\mathbf{r} = \mathbf{x}^\alpha - \mathbf{x}$,

$$\frac{\partial\psi(\mathbf{r})}{\partial\mathbf{x}} = \frac{\partial\psi(\mathbf{r})}{\partial\mathbf{r}} \frac{\partial\mathbf{r}}{\partial\mathbf{x}} = -\frac{\partial\psi(\mathbf{r})}{\partial\mathbf{r}}.$$

This relation can be used to show that $\frac{\partial\psi}{\partial t} = -\mathbf{v}^\alpha \cdot \partial_{\mathbf{x}}\psi$.

3. A bond function $B^{\alpha\beta}(\mathbf{x})$ between atoms α and β is defined by the expression

$$B^{\alpha\beta}(\mathbf{x}) \equiv \int_0^1 \psi(\lambda\mathbf{x}^{\alpha\beta} + \mathbf{x}^\beta - \mathbf{x}) d\lambda,$$

where $\mathbf{x}^{\alpha\beta} = \mathbf{x}^\alpha - \mathbf{x}^\beta$. $B^{\alpha\beta}$ represents a weighted fraction of the bond length segment between atoms α and β that lies within the characteristic volume. By taking the derivative of $\psi(\lambda\mathbf{x}^{\alpha\beta} + \mathbf{x}^\beta - \mathbf{x})$ with respect to λ ,

$$\frac{\partial\psi(\lambda\mathbf{x}^{\alpha\beta} + \mathbf{x}^\beta - \mathbf{x})}{\partial\lambda} = -\mathbf{x}^{\alpha\beta} \cdot \partial_{\mathbf{x}}\psi(\lambda\mathbf{x}^{\alpha\beta} + \mathbf{x}^\beta - \mathbf{x}),$$

and then integrating from $\lambda = 0$ to $\lambda = 1$, one obtains

$$\psi(\mathbf{x}^\alpha - \mathbf{x}) - \psi(\mathbf{x}^\beta - \mathbf{x}) = -\mathbf{x}^{\alpha\beta} \cdot \partial_{\mathbf{x}}B^{\alpha\beta}(\mathbf{x}).$$

More detailed information regarding the use of these localization functions can be found in [52], [55] and [4].

In order to derive an expression for a symmetric stress tensor, Hardy has made four key assumptions about the forms of the energies and forces for the atoms in the system:

- i. The total potential energy of the system, Φ , can be considered to be the summation of individual potential energies of each atom within the system, $\Phi = \sum_{\alpha=1}^N \phi^\alpha$.
- ii. The force on any atom can be expressed by the summation $\mathbf{F}^\alpha \equiv -\frac{\partial\Phi}{\partial\mathbf{x}^\alpha} = \sum_{\beta \neq \alpha}^N \mathbf{F}^{\alpha\beta}$. In general, it is not clear what the physical meaning of $\mathbf{F}^{\alpha\beta}$ is. When Φ is the summation of pair potentials, $\phi^\alpha = \frac{1}{2} \sum_{\beta \neq \alpha}^N \phi^{\alpha\beta}(x^{\alpha\beta})$ where $x^{\alpha\beta} = |\mathbf{x}^{\alpha\beta}|$, $\mathbf{F}^{\alpha\beta}$ obviously means the force exerted on atom α from atom β . However, for some multi-body potentials the meaning is not so straight-forward.
- iii. The atomic potential energies depend only on interatomic distances, $\phi^\alpha = \phi^\alpha(x^{\alpha\beta}, x^{\alpha\gamma}, \dots, x^{\beta\gamma})$, so $\mathbf{F}^\alpha = -\sum_{\beta \neq \alpha}^N \sum_{\gamma=1}^N \frac{\partial\phi^\alpha}{\partial x^{\alpha\beta}} \frac{\mathbf{x}^{\alpha\beta}}{x^{\alpha\beta}}$. This expression includes the possibility that $\alpha = \gamma$. While this assumption clearly holds for radially-symmetric potentials such as pair potentials and the Embedded Atom Method (EAM) [32], it is necessary to consider invariance of the system potential energy to show that it also holds for potentials that depend on bond orientations (see Section 3.5).

- iv. Each atomic potential energy depends only on the distances between the atom under consideration and all other atoms, $\phi^\alpha = \phi^\alpha(x^{\alpha\beta}, x^{\alpha\gamma}, \dots, x^{\alpha N})$. Thus, the force between atoms α and β can be expressed as $\mathbf{F}^{\alpha\beta} = - \left\{ \frac{\partial \phi^\alpha}{\partial x^{\alpha\beta}} + \frac{\partial \phi^\beta}{\partial x^{\alpha\beta}} \right\} \frac{\mathbf{x}^{\alpha\beta}}{x^{\alpha\beta}}$. Clearly, while this assumption holds for pair potentials and EAM, it does not for some multi-body potentials such as the 3-body potential of Stillinger-Weber [33] used to model silicon.

Using the density functions shown above within the balance equations, and by considering the four assumptions listed, Hardy developed the following expression for stress at a spatial point,

$$\boldsymbol{\sigma}(\mathbf{x}, t) = - \left\{ \frac{1}{2} \sum_{\alpha=1}^N \sum_{\beta \neq \alpha}^N \mathbf{x}^{\alpha\beta} \otimes \mathbf{F}^{\alpha\beta} B^{\alpha\beta}(\mathbf{x}) + \sum_{\alpha=1}^N m^\alpha \mathbf{u}^\alpha \otimes \mathbf{u}^\alpha \psi(\mathbf{x}^\alpha - \mathbf{x}) \right\}, \quad (3.7)$$

where $\mathbf{u}^\alpha \equiv \mathbf{v}^\alpha - \mathbf{v}$. Hardy's formalism also provides expressions for the heat flux vector \mathbf{q} and the internal energy density e .

It is possible to recover various definitions for atomic stress already mentioned by making specific choices for the characteristic volume. For example, if the characteristic volume is taken to be the entire volume of the atomic system, and the system is static, (3.7) exactly reproduces the result of the virial theorem, the average stress within the system, $\bar{\boldsymbol{\sigma}} = \frac{1}{V} \int_{\mathcal{R}^3} \boldsymbol{\sigma}(\mathbf{x}) d^3\mathbf{x}$. In this case time averaging is unnecessary since the assumption of static equilibrium for the continuum is made. For a dynamic continuum, the calculation of the material velocity at the chosen spatial point, \mathbf{v} , would be necessary because a non-zero value would affect the quantities $\{\mathbf{u}^\alpha\}$ in (3.7). Another example is that of the characteristic volume collapsing to a spatial plane containing no atoms. Hardy noted this case in his original publication [52], and showed that his stress expression reduces to the common definition for stress of force divided by area. This result demonstrates the physical intuitive quality desired by both Tsai and Cheung and Yip, while avoiding the need to consider momentum transport across spatial boundaries. Finally, it can be observed that for a characteristic volume that surrounds a single atom, the expression derived by Zhou [49, 50] for the average stress within the volume is obtained. In this situation, the material velocity of the continuum equals the velocity of the atom encased, $\mathbf{v} = \mathbf{v}^\alpha$, and no momentum term appears in the stress expression.

The stress expression developed by Hardy and given in equation (3.7) is robust in that it defines a suitable measure of stress at any length scale, and is also supposedly independent of the choice of localization function. However, in the next section we test those assertions and develop guidelines for the ways in which to use this expression.

3.3 Results and Discussion

For our simulations, we use the EAM potentials for copper (Cu) by Foiles, Baskes and Daw [32]. Unless otherwise noted, the localization function has a constant value within a spherical volume of radius R_c and equals zero outside of the volume, *i.e.* $\psi(r)$ is a radial step function centered at $r = R_c$. With this choice of ψ , $B^{\alpha\beta}$ has the simple geometric interpretation of the fraction of bond length between atoms α and β (normalized by $\frac{4}{3}\pi R_c^3$) that lies within the characteristic volume. As both Hardy and Cormier *et al.* have noted, this applies even for situations in which neither atom α nor atom β lie within the characteristic volume, but a portion of the line segment connecting the two atoms does.

3.3.1 Stress in a crystal at zero temperature

Quasi-static simulations were performed for a bulk Cu lattice comprised of 3,072 atoms with periodic boundary conditions on all sides at zero temperature and pressure. The size of the computational box was 8 x 8 x 12 unit cells. For this system, the stress at any spatial point should equal zero; however, this was not observed as shown in Figure 3.1. The Hardy

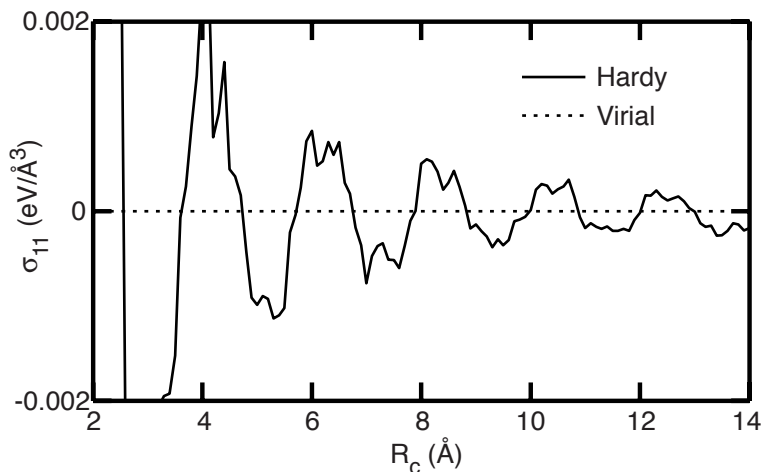


Figure 3.1: Virial and Hardy stress for an atomic system at zero temperature and pressure.

stress contains small fluctuations that diminish in magnitude as R_c increases. Hardy, Root and Swanson [54] noticed this correlation between fluctuations in stress and the size of the characteristic volume. Also displayed in Figure 3.1 is the volume average of the local virial stress for a spherical volume of radius R_c . This volume average can be expressed by the

relation

$$\bar{\pi} = -\frac{1}{V_c} \left\{ \frac{1}{2} \sum_{\alpha \in V_c} \sum_{\beta \neq \alpha} \mathbf{x}^{\alpha\beta} \otimes \mathbf{F}^{\alpha\beta} + \sum_{\alpha \in V_c} m^\alpha \mathbf{u}^\alpha \otimes \mathbf{u}^\alpha \right\}, \quad (3.8)$$

where $V_c = \frac{4}{3}\pi R_c^3$. For quasi-static analysis, the second term in the above expression vanishes. Figure 3.1 shows that the value for $\bar{\pi}_{11}$ is exactly zero, to the limit of computational precision, for all values of R_c , an expected result since all individual atomic stresses are zero for this case. The behavior of the Hardy stress expression is due to differing amounts of force contribution for individual interacting atomic pairs as the characteristic volume changes. As the characteristic volume increases, the bond function $B^{\alpha\beta}$ changes its value only for those atomic pairs that have at least one of the atoms lying outside the volume. As R_c increases, the magnitude of these force contributions become much less significant than the force contributions from atomic pairs already inside the volume. Since the number of bonds lying completely within the volume increases as R_c^3 and the number that partially contribute to the stress increases as R_c^2 , one would expect the amplitude of fluctuations to decay as roughly R_c^{-1} . However, analysis of the values shown in Figure 3.1 reveals that this decay occurs much faster, with the magnitude of the fluctuation decreasing at a rate between $R_c^{-2.4}$ and R_c^{-3} . Future efforts will be undertaken to understand the mathematical and physical significance of this. A more detailed examination of this fluctuation was done by varying the position of the spatial point within a unit cell of the crystal lattice, as shown in Figure 3.2. For this detailed analysis, a cubic function was used for the localization function,

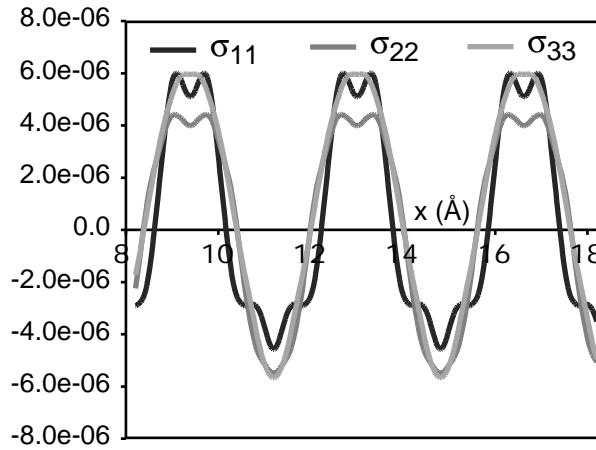


Figure 3.2: Hardy stresses within a Cu crystal at zero temperature and pressure. Spatial position is varied across 2.5 unit cells of lattice parameter equal to 3.615 Å.

$\psi(r) \sim 1 - 3\left(\frac{r}{R_c}\right)^2 + 2\left(\frac{r}{R_c}\right)^3$ where $r \equiv |\mathbf{x}^\alpha - \mathbf{x}| < R_c$. This function has the properties that $\psi(r) \rightarrow 0$ and $\psi'(r) \rightarrow 0$ as $r \rightarrow R_c$, and permits us to isolate the general behavior of using any localization function from the discontinuous nature of the step function. This figure shows that the fluctuation of stress occurs over the length scale of the crystal's lattice

parameter around a zero mean value. It also reveals that the magnitude of the fluctuation is much smaller for a cubic localization function than for the constant function. While it is disturbing that application of the Hardy expression contains an intrinsic fluctuation for the zero stress case, it will be demonstrated that this fluctuation is insignificant for particular simulations at either non-zero stress or finite temperature.

The curve shown in Figure 3.1 was for the normal stress evaluated at a single spatial point chosen at random. Examination of the mean of this curve averaged over many such randomly chosen points, shown in Figure 3.3, reveals that the magnitude of these fluctuations becomes vanishingly small as the number of averaging points increases. The fluctuations decrease

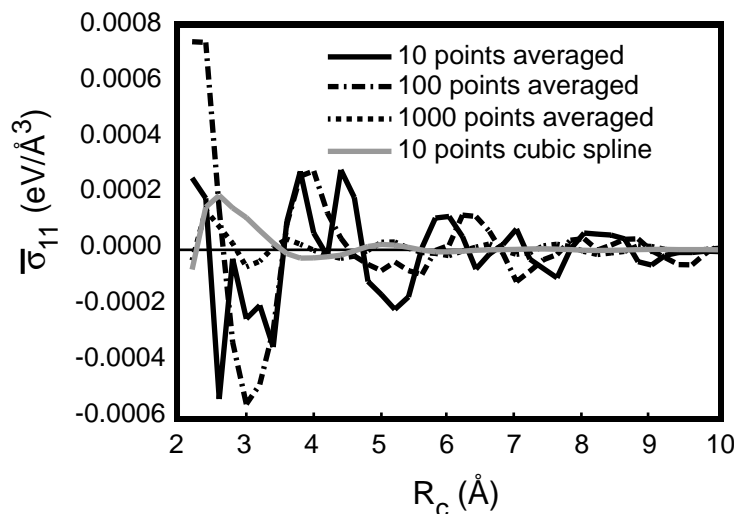


Figure 3.3: Mean of the Hardy stress averaged over many spatial points.

in magnitude by a factor of 10 when stress is averaged over 10 or 100 spatial points, and decrease by a factor of 50 or greater when stress is averaged over 1000 points. This behavior is consistent with the definition of the Hardy stress (3.7). As more spatial points are used for averaging, we are, in-effect, integrating (3.7) over all space. This integration results in recovery of the average system stress predicted by the virial theorem, which is zero for this case. These evaluations were primarily done using a localization function of constant value within the characteristic volume. However, we also performed an averaging of 10 spatial points using the cubic function already discussed. It is clear that for a given characteristic volume size, the use of a localization function that smoothly and continuously evaluates to zero at the volume boundary, *i.e.* $\psi(r) \rightarrow 0$ and $\psi'(r) \rightarrow 0$ as $r \rightarrow R_c$, produces a more consistent estimate of continuum stress.

The impact of these fluctuations is indeed less significant for cases of non-zero values of stress, as shown in Figure 3.4 for a system under 2% uniaxial strain. The Hardy stress fluctuates around the expected value of $0.02 \text{ eV}/\text{\AA}^3$, with the magnitude of the fluctuation

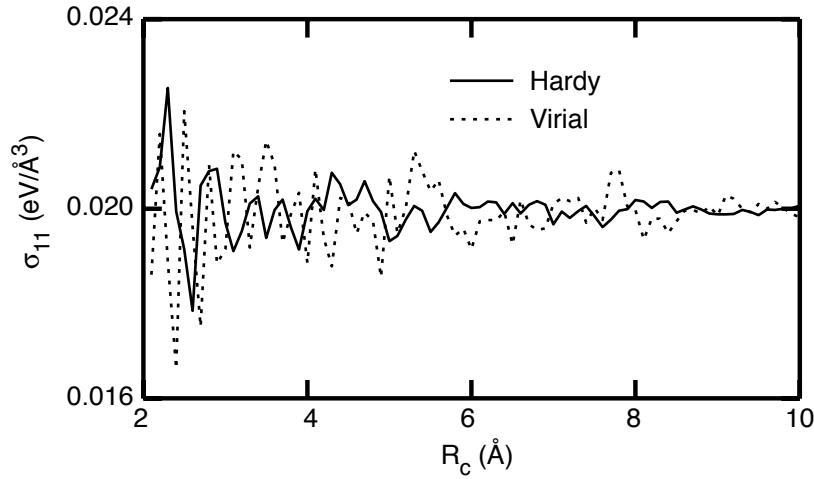


Figure 3.4: Virial and Hardy stress for an atomic system at zero temperature and 2% uniaxial strain.

decaying with increased R_c . The error is acceptably low at even moderate values of R_c , it is only 4% at $R_c = 6 \text{ \AA}$. The virial stress also fluctuates about the expected value due to the minor changes in volume that alter all continuum densities. The error in the averaged virial stress does not decay as quickly as for the Hardy stress, and is significant even up to distances of 8 \AA .

3.3.2 Stress in a crystal at finite temperature

Stress within a system at finite temperature was also evaluated. Figure 3.5(a) shows the stress evaluated at two distinct spatial points within a Cu system consisting of 4,000 atoms ($10 \times 10 \times 10$ unit cells) equilibrated to zero pressure at room temperature, 300 K. The two points are located at positions (A) $\{11.3 \text{ \AA}, 15.5 \text{ \AA}, 7.0 \text{ \AA}\}$ and (B) $\{-11.7 \text{ \AA}, -12.5 \text{ \AA}, -14.8 \text{ \AA}\}$, where the bounds of the system are $\pm 18.075 \text{ \AA}$ in each direction. In our simulations, temperature control is performed by exerting a drag force on each atom that is proportional to both the difference between the current temperature and the desired temperature for the system and the atom's velocity [56]. We observe that the value of stress evaluated at an arbitrarily chosen spatial point at an instant of time varies much more than for the zero temperature case shown in Figure 3.1. We also note that this variation does not possess the periodic nature with oscillations of a single wavelength, the lattice parameter. The curves shown for the two spatial points possess much more complex shapes than the zero temperature case, and differ significantly from one another. For the range of $R_c > 6 \text{ \AA}$, the variations in each curve, and the differences between the two curves, are at a much smaller scale and the value of stress is close to zero, although the difference between the finite temperature value

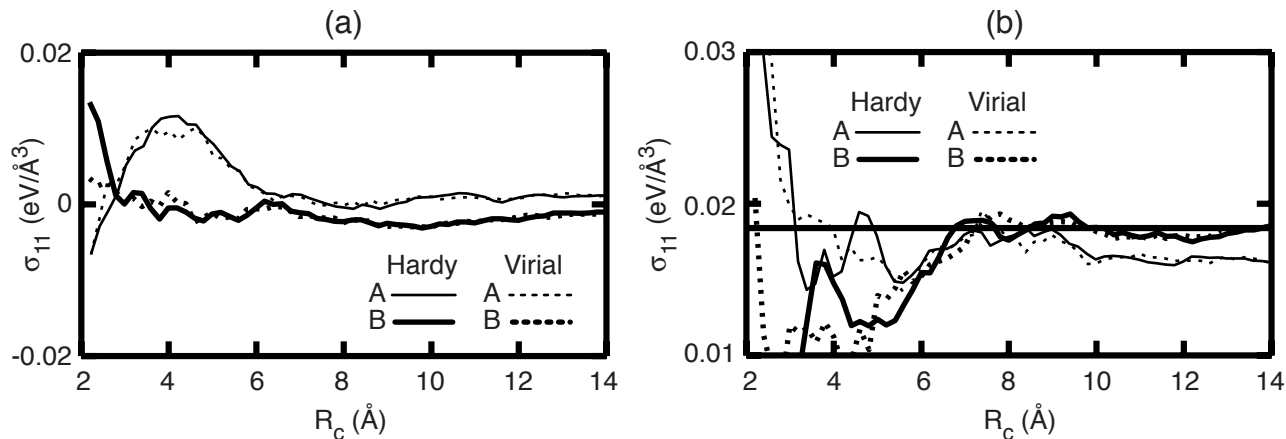


Figure 3.5: Virial and Hardy stress for an atomic system at 300 K temperature at (a) zero pressure and (b) 2% uniaxial strain. The heavy horizontal line in (b) is the system value of stress as determined from the virial theorem. Two sets of lines are shown for each stress to signify the two spatial points, A and B.

of stress predicted at even the largest value of R_c , 14 Å, and the system averaged value is significant. This provides evidence that a larger characteristic volume must be used at finite temperature in order to capture the statistics at a similar level of accuracy as for the zero temperature case. For systems of limited size, we would recommend either averaging over multiple volumes centered on nearby spatial points at a given time step or averaging over the same characteristic volume for multiple time steps. The former sacrifices the resolution for inhomogeneous stress fields while the latter requires a sufficient time window of analysis.

It can also be noticed in Figure 3.5(a) that the behavior of the locally averaged virial stress is very similar to the Hardy stress, especially for values of $R_c > 6$ Å. The characteristic shape common to both stresses may be due to the kinetic contribution to the stress tensor since this term is the same expression for both equations (3.7) and (3.8). However, it is important to note that for even moderate values of R_c , Hardy and virial stress are comparable.

Figure 3.5(b) shows the stresses for the same system at 300 K uniaxially strained by 2%. As before, it is noticed that at finite temperature the variations in stress with R_c possess both larger magnitudes, ~ 0.005 eV/Å³ as compared with ~ 0.001 eV/Å³ for the zero temperature case in Figure 3.4, and a more complex shape.

We have already proposed that by averaging the stress expression evaluated for the same characteristic volume over multiple time steps, the Hardy and virial expressions for stress may achieve a higher level of accuracy and would be statistically similar to the single time step, zero temperature evaluations. Figure 3.6 shows the resulting time averaged curves for one of the spatial points evaluated in Figure 3.5. Although curves are displayed only for the Hardy

stress expression, the volume-averaged virial stress behaves similarly in all cases, especially for $R_c > 6 \text{ \AA}$. Figure 3.6(a) shows the curves resulting from averaging the stress component σ_{11} over 1, 10, 100 and 1000 MD time steps ($\Delta t = 2 \text{ fs}$) for the zero pressure simulations at 300 K and Figure 3.6(b) shows similar curves for the system uniaxially strained 2%. Both

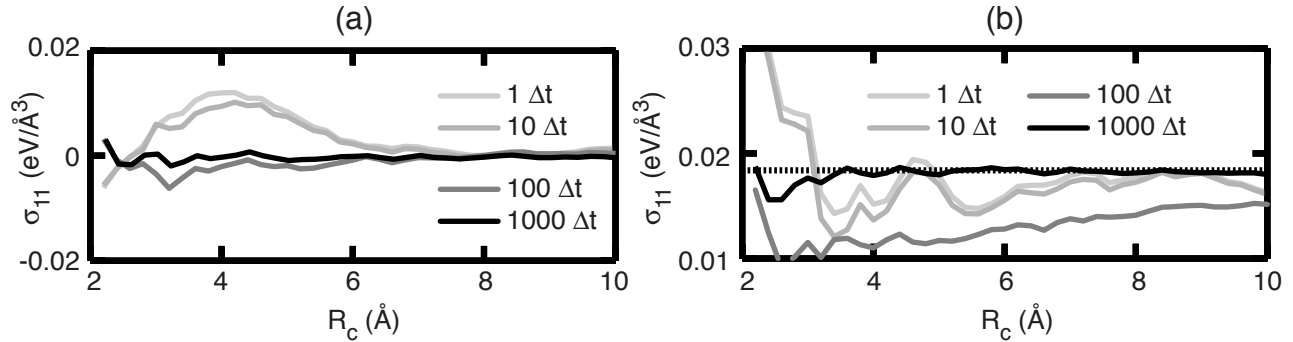


Figure 3.6: Hardy stress for an atomic system at 300 K temperature at (a) zero pressure and (b) 2% uniaxial strain. The dotted horizontal line in (b) is the system value of stress as determined from the virial theorem. Each point plotted is actually the value of stress averaged over 1, 10, 100 or 1000 MD time steps ($\Delta t = 2 \text{ fs}$), as denoted by the legend.

sets of data make a compelling case for time averaging at finite temperature. In particular for the zero stress case, σ_{11} is observed to be predominantly tensile for both the 1 and 10 Δt data at small values of R_c . For averaging over 100 Δt , this behavior is absent and the data converges on an acceptable description of the system stress state for $R_c > 5 \text{ \AA}$. Examination of Figure 3.6(b) shows that longer averaging time, at least 1000 time steps, *i.e.* 2 ps, is needed to reduce the error in the predicted stress to some tolerable level. These curves do indicate that statistical behavior becomes noticeably more consistent in going from 10 Δt to 100 Δt . For both 1 and 10 Δt , the behavior in the predicted stress is not consistent; indeed, at $R_c = 10 \text{ \AA}$, the curves possess deviations from the ensemble average that are increasing as R_c increases. For both 100 Δt and 1000 Δt averaging, however, the predicted stress moves consistently towards the ensemble average as R_c is increased. Thus, in order to maintain a localized characteristic volume and obtain some predetermined level of accuracy, one must restrict the analysis to some minimum time for averaging. One conclusion that can be made is that just as both the Hardy and virial stress expressions converge to expected continuum mechanical behavior by using some type of local volume averaging, this convergence is even more pronounced by performing a localized time averaging. Also, just as the value of R_c — the size of the characteristic volume for weighted spatial averaging — is required to be larger than some minimum value related to either the lattice parameter or the inter-atomic potential interaction range in order to achieve a sufficient level of accuracy, so too should the time averaging window size be required to be larger than some minimum period. It is unclear what precisely determines this minimum amount of time, but it may be influenced by the phonon lifetimes characteristic for the particular materials and temperatures simulated. The ability to attain the same level of statistical accuracy by enlarging one of these windows

while refining the other suggests that an ergodicity property exists for sub-sets of the full atomistic system.

This analysis shows that at finite temperature, deformation, or both, the Hardy stress expression is certainly as good as the virial stress and even displays improved behavior in some instances. The finite temperature analysis also establishes a significant motivation for time averaging of the stress expression.

3.3.3 Stress in a crystal with a free surface

The underlying basis for fluctuations of stress with characteristic volume size greatly impacts stress evaluation for regions with inhomogeneous structure, such as at a free surface. Figure 3.7 shows the stress within a Cu crystal as a function of distance from a free surface for two values of R_c , 6 and 10 Å. We first examine Figure 3.7(a) and (b), which display the

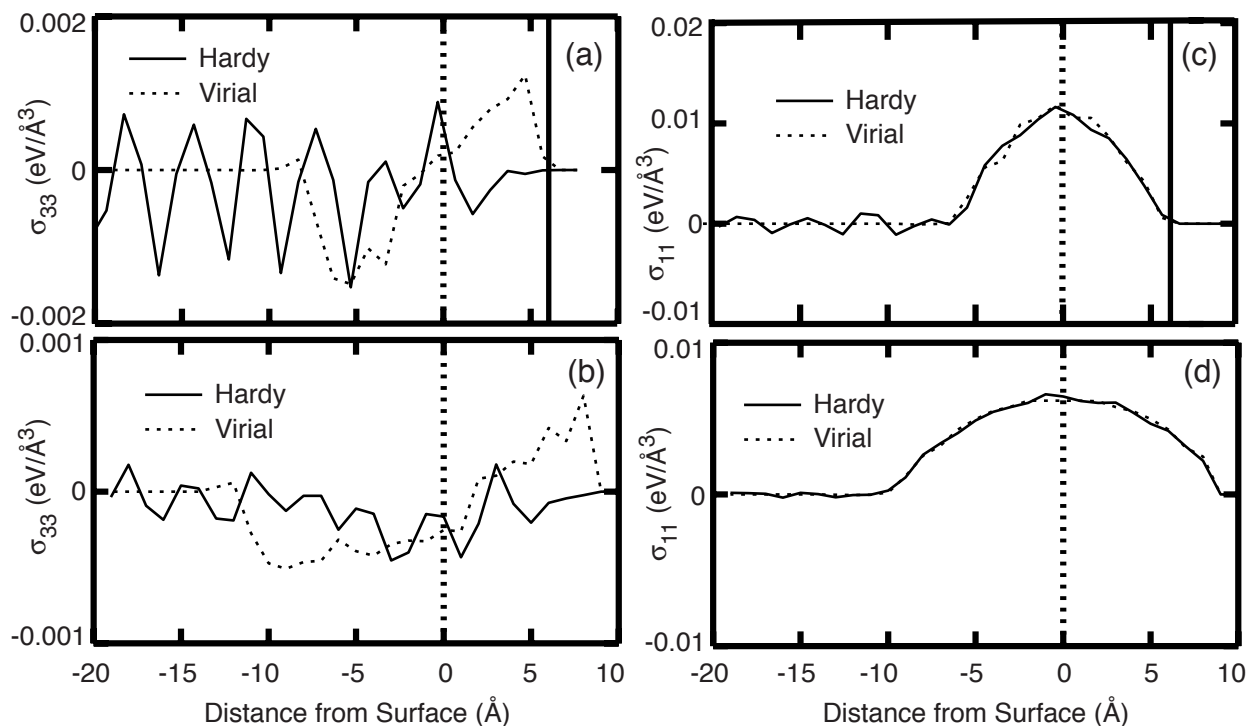


Figure 3.7: Virial and Hardy stress for an atomic system at zero temperature and pressure with a free surface. The dashed line denotes the position of the top layer of atoms while the solid line denotes the effective position of the free surface of the crystal. (a), (b) The normal stress for the direction perpendicular to the free surface for $R_c = 6, 10$ Å. (c),(d) The normal stress for directions parallel to the free surface for $R_c = 6, 10$ Å.

normal stress for the direction perpendicular to the free surface. Within a distance R_c of the top atomic layer, the magnitude of fluctuations is comparable for both expressions. However, the wavelength of the virial fluctuation is clearly tied to the size of the characteristic volume. It equals twice the value of R_c . This result shows a smearing of the oscillation in local virial stress noticed by Cheung and Yip [37]. In contrast, the wavelength for the Hardy stress fluctuations is considerably smaller than for the virial, and is roughly the same for both values of R_c . Also, the Hardy value decays within the region between the top atomic layer and the “effective” surface of the crystal, located at a distance equal to R_c , while the virial stress increases in magnitude, only dropping to zero within 0.5 \AA of the effective surface. Again, it is important to notice that within a distance R_c above the top atomic layer, atomic force interactions are detectable and contribute to the calculation of stress.

Also examined were the normal stress components for directions parallel to the free surface, the planar stress that normally corresponds to surface stress. This is shown in Figure 3.7(c) and (d) for the same atomic system discussed above. We observe that the stress distribution is essentially the same for both the Hardy and virial expressions, displaying a build-up of finite stress below the effective surface that represents a material’s surface stress, and a drop-off to zero at the effective surface of the solid. We also notice that the maximum value of the tangential stress is smaller for $R_c = 10 \text{ \AA}$ than for 6 \AA , while the extent of the build-up region is larger as it equals $2R_c$. It is the case that for both choices of R_c , the integration of σ_{11} over the build-up region yields a value of surface stress of 0.085 eV/\AA^2 .

3.4 Conclusions and Discussion

Our analysis has shown that, for most situations of non-zero deformation, finite temperature, or both, the definition for Cauchy stress in an atomic system developed by Hardy provides an estimate for continuum mechanical stress as or more accurate than the expression based on the virial theorem. In general, fluctuations in the Hardy stress are lower in magnitude and decay faster with increasing characteristic volume size. Use of a smooth, continuous localization function with compact support reduces the magnitude of variations in the Hardy stress from expected values. Our results also showed that the fluctuations in stress for systems at finite temperature are larger in magnitude than at zero temperature. However, it was discovered that time averaging of the stress expression yields improved convergence to the expected value of stress at finite temperature for both unstrained and deformed states of the crystal. Given this result and the results shown for spatial averaging, it is clear that a lower limit for spatial and temporal resolution exists when trying to make a legitimate correspondence between a sub-volume of atoms during a sub-interval of time and a continuum material point at a particular time. This limit implies that for systems that are either too small in size, or simulations that are too short in duration, connections between such systems and an equivalent continuum cannot be made. For simulations involving inhomogeneous

deformation or rapidly time varying atomistic quantities, there may also exist an upper limit of resolution beyond which information is lost when trying to map atomistic quantities to their continuum counterparts. Finally, the behavior of the Hardy expression for stress near a free surface was found to be consistent with the mechanical definition of stress. Visualization of the normal stress field revealed that the effective free surface of a solid does not coincide with the top-most atomic layer, but rather at a distance beyond which no force interactions can be detected. The free surface itself is now defined as the spatial plane at which the component of $\boldsymbol{\sigma}(\mathbf{x}, t)$ for the direction normal to the plane equals zero.

An attempt can be made to improve upon Hardy’s method with regard to the elimination of stress fluctuations, at least for the case of zero temperature, by recognizing its similarity to moving least squares (MLS) particle methods [57, 58] used by the continuum mechanics community. An important consideration for such methods is the condition of consistency, the ability of a numerical solution to a boundary value problem to reproduce certain states of deformation, *e.g.* homogeneous stress, exactly. An example of such a method is the Reproducing Kernel Particle Method (RKPM) [59], which uses a multiplicative combination of polynomial basis functions and a compact support window function. The resulting “corrected” window function allows the solutions for field variables to exactly represent polynomials up to the order given by the basis functions. The use of such corrected localization functions within Hardy’s framework may be sufficient to capture homogeneous deformation fields and eliminate fluctuations at the primitive cell scale. It is interesting to note that in Hardy’s formulation fields such as velocity and stress are defined in a way that makes them consistent with the continuum balance of linear momentum. Unlike MLS, where a smoothing approximation would be applied first and then a constitutive law based on the continuum displacement or velocity would be applied to obtain stress, Hardy derives his stress ultimately from the interatomic energy potentials and the atomic velocity trajectories. Hardy’s method may be interpreted as a post-processing step for a single configuration of an atomistic simulation. However, given that his derived quantities are consistent with continuum balance laws, an outside observer could not tell whether continuum quantities were derived from atomistic balance of linear momentum or the continuum version. This feature may make Hardy’s method useful for atomistic-continuum coupling.

An important aspect in the derivation of Hardy’s stress expression is the group of underlying assumptions made, listed in section 3.2, that restrict the use of the expression to systems governed by central potentials such as pair potentials and the EAM. Application of Hardy’s formalism to generalized, multi-body potentials requires a redefinition of the quantities $\mathbf{F}^{\alpha\beta}$. However, it is unclear if such definitions would still yield a *symmetric* stress tensor. Modifications to Hardy’s derivation may be required that connect the atomic system to a non-standard continuum model. This effort will be undertaken by the authors at a future time.

3.5 Appendix: Invariance of Atomic Bond Energies

For a finite system of N particle, the set of their positions, $\kappa = \{\mathbf{x}^\alpha, \alpha = 1..N\}$, with their masses m^α constitutes a ‘configuration’ in a static setting (momenta \mathbf{p}^α or velocities \mathbf{v}^α are necessary to describe a configuration in a dynamic setting). The energy of the system Φ depends on the configuration $\Phi = \Phi(\kappa) = \Phi(\{\mathbf{x}^\alpha\})$; however, a basic symmetry rule, invariance under superposed rigid body motion or change in coordinate frame, restricts how the energy depends on the configuration. Invariance requires that

$$\Phi^+ := \Phi(\{\mathbf{x}^{\alpha+}\}) = \Phi(\{\mathbf{x}^\alpha\}) =: \Phi$$

where

$$\mathbf{x}^{\alpha+} = \mathbf{Q}\mathbf{x}^\alpha + \mathbf{a}, \quad \mathbf{Q} \in Orth^+$$

In other words, the potential energy of the system cannot change with rigid rotations and translations of the configuration. This implies that the energy cannot depend directly on the particles’ positions.

Every atomistic system of particles has a substructure made up of bonds \mathcal{B} , so that the total energy can be decomposed as:

$$\Phi = \sum_{K \in \mathcal{B}} \phi^K .$$

The energy of an individual bond depends only on a subset of the configuration, *e.g.* two $\{\mathbf{x}^\alpha, \mathbf{x}^\beta\}$ or three $\{\mathbf{x}^\alpha, \mathbf{x}^\beta, \mathbf{x}^\gamma\}$ or four atoms $\{\mathbf{x}^\alpha, \mathbf{x}^\beta, \mathbf{x}^\gamma, \mathbf{x}^\delta\}$. By applying the invariance principle, it is clear that ϕ^I can only depend on invariants like a distance

$$I_d = \|\mathbf{x}^{\alpha\beta}\| \quad \text{where } \mathbf{x}^{\alpha\beta} := \mathbf{x}^\beta - \mathbf{x}^\alpha ,$$

a cosine of an angle

$$I_a = \frac{1}{\|\mathbf{x}^{\alpha\beta}\| \|\mathbf{x}^{\beta\gamma}\|} \mathbf{x}^{\alpha\beta} \cdot \mathbf{x}^{\beta\gamma} ,$$

an area

$$I_s = \|\mathbf{x}^{\alpha\beta} \times \mathbf{x}^{\beta\gamma}\| ,$$

or a volume

$$I_v = [\mathbf{x}^{\beta\alpha}, \mathbf{x}^{\gamma\alpha}, \mathbf{x}^{\delta\alpha}] := (\mathbf{x}^{\beta\alpha} \times \mathbf{x}^{\gamma\alpha}) \cdot \mathbf{x}^{\delta\alpha} .$$

In all these invariants the difference in positions removes the dependence on the rigid translation \mathbf{a} and the inner product or cross product removes the dependence on the rigid rotation \mathbf{Q} .

Chapter 4

Statistical Mechanics and Multiscale Processes

Principle Author: C.J. Kimmer

No robust multiscale method exists for coupling molecular dynamics (MD) and finite element (FE) simulations when the MD region is at nonzero temperature and the continuum constitutive model is temperature dependent. Coarse-grained molecular dynamics (CGMD) [10] and the quasicontinuum method (QC) [60] are the main published attempts at this coupling, but there are few demonstrations that they are complete or robust. Newer methods such as the bridging scale [12] can in principle incorporate the effects of temperature in both the atomistic and continuum regions, but an adequate means of doing so has not correctly been identified yet.

All these approaches try to produce a high-fidelity representation of a system with many degrees of freedom using a system with many fewer degrees of freedom. In addition to the challenge of dynamically accounting for the removed, “unimportant” degrees of freedom, the continuum stress-strain description is not the natural one for the MD system. Moreover, the correspondence between a temperature-dependent continuum and a temperature-dependent atomic system is defined only in the long time, large length scale limit. Here, it suffices to consider model problems with a clear relationship between equivalent atomistic and continuum systems. Consequently, attention will be restricted to homogeneous deformation, uniform temperature, or a uniform temperature gradient. Even in these cases, the long time, large length scale limit leading to equivalence are much longer and larger than would be practical or even useful for a coupling problem. To remedy this difficulty, the atomic-scale data must be analyzed to extract useful information for the continuum, or the continuum description must be modified to more accurately reflect atomic-scale phenomena at non-zero temperature.

This chapter first reviews the basic notions of statistical mechanics (SM) for equilibrium and

non-equilibrium systems. The description of equilibrium SM is classical and based on "text-book" approaches. Developments in nonequilibrium SM are much more current as the field is still active, and at least parts of the discussion constitute a review of the literature. The next section discusses relevant statistical measures for determining the correspondence between equivalent atomistic and continuum systems at non-zero temperature. Assuming a generic coupling method for transferring information between temperature-dependent MD and FE simulations, the implications for consistency with the corresponding all-atomic system at thermal equilibrium are discussed. Numerical examples illustrating the discussed measures are given, and, finally, similar simulations and measures for nonequilibrium systems are discussed.

4.1 Equilibrium Statistical Mechanics

4.1.1 Overview of Phase Space and Ensembles

A useful model Hamiltonian for a system with atoms labelled by $\alpha \in \{1 \dots N\}$ is

$$\mathcal{H} = \sum_{\alpha} \frac{p_{\alpha}^2}{2m_{\alpha}} + \sum_{\alpha, \beta} \phi_{\alpha\beta}(x_{\alpha\beta}) \quad (4.1)$$

The main assumption here is that only central force pair-potential interactions exist between the atoms. The magnitude of the separation between atom α and atom β 's coordinates is denoted by $x_{\alpha\beta} = |\mathbf{x}_{\alpha\beta}| = |\mathbf{x}_{\alpha} - \mathbf{x}_{\beta}|$, and the momentum of atom α is \mathbf{p}_{α} .

Mechanical equilibrium states are extrema of the potential energy, but thermal equilibrium describes a more complicated state determined by temperature and any number of other macroscopic variables such as pressure (or stress) or applied external fields. Although the thermal equilibrium state and a material's macroscopic response is ultimately determined by fundamental interactions at the atomic scale or smaller, it is neither possible nor practical to possess a completely detailed knowledge of every degree of freedom in a macroscopic system ($N \sim 10^{23}$). Consequently, the experimentally-obtained macroscopic quantities characterizing a material's state are themselves temporal and spatial averages of quantities depending on the details of atomic motion. Mathematically, macroscopic quantities are the averages of functions of the N coordinates and momenta. The average value of the Hamiltonian \mathcal{H} is an example of one such quantity; it is the system's internal energy.

To facilitate the description of macroscopic quantities that are possibly functions of the $6N$ individual components of the momenta and coordinates, the concept of *phase space* is helpful. Phase space is the $6N$ -dimensional space of the coordinates and momenta, and the concatenation of all components of the momenta and coordinates $\Gamma = (\mathbf{p}_1, \mathbf{p}_2, \dots, \mathbf{p}_N, \mathbf{x}_1, \mathbf{x}_2, \dots, \mathbf{x}_N)$

represents a *microstate* of the system. The set of all microstates with the same macroscopic value (of \mathcal{H} , say) is a *macrostate*, whose thermomechanical properties are probed by experiment.

If the initial conditions for the Hamiltonian of Equation 4.1 are known, the deterministic trajectory in phase space is the solution to Hamilton's equations of motion

$$\dot{\mathbf{x}}_\alpha = \frac{\partial \mathcal{H}}{\partial \mathbf{p}_\alpha} = \frac{\mathbf{p}_\alpha}{m_\alpha} \quad \dot{\mathbf{p}}_\alpha = -\frac{\partial \mathcal{H}}{\partial \mathbf{x}_\alpha}. \quad (4.2)$$

When only the macrostate is known, there can be a considerable degeneracy of microstates in the single macrostate. At this point, the dynamics specified by the equations is not a very useful way to characterize the macrostate. The trajectories are less relevant than the sets of degenerate microstates. These sets of microstates define an *ensemble*, and in statistical mechanics, the ensembles of microstates are the tool for determining the equilibrium macrostates. The most common ensembles are the microcanonical ensemble which is the set of all states with a given energy U and volume V , the canonical ensemble with fixed N and varying U , and the grand canonical ensemble in which N varies as well.

The distribution function $f(\Gamma)$ is the likelihood of being in the microstate Γ . It is used to compute the *ensemble average* $\langle X \rangle$ of a quantity X over all microstates:

$$\langle X \rangle = \frac{\int f(\Gamma) X(\Gamma) d\Gamma}{\int f(\Gamma) d\Gamma}. \quad (4.3)$$

So far, two kinds of averaging have been mentioned—ensemble averages and the spatial or temporal averages performed by a measurement. The two approaches are unified by the *ergodic hypothesis* which posits the two to be equivalent, allowing the averaging over trajectories performed by measurement to be replaced by ensemble averaging over microstates. A second fundamental hypothesis states that an equilibrium system is equally likely to be in any microstate with the correct equilibrium values of the macroscopic parameters. In other words, the distribution function for the microcanonical ensemble is $f = \delta(\mathcal{H} - U)$. In phase space, the system, occupies an *energy shell* whose area \mathcal{Z} is given by

$$\mathcal{Z}(U) \equiv \int \delta(\mathcal{H} - U) d\Gamma. \quad (4.4)$$

The microcanonical ensemble correctly describes an energetically-isolated, macroscopic system in thermal equilibrium.

For Hamiltonian systems, states in phase space are neither created nor destroyed, and the total time derivative of the distribution function f is zero. For systems governed by more general equations of motion, the creation of states in phase space must be taken into account, but this aspect will not be treated here. At thermal equilibrium, the distribution function

will depend on time only through the individual coordinates and momenta. The condition $\frac{df}{dt} = 0$ allows one to write

$$\frac{\partial f}{\partial t} = - \sum_{\alpha} \left(\frac{\partial f}{\partial \mathbf{p}_{\alpha}} \cdot \frac{\partial \mathbf{p}_{\alpha}}{\partial t} + \frac{\partial f}{\partial \mathbf{x}_{\alpha}} \cdot \frac{\partial \mathbf{x}_{\alpha}}{\partial t} \right) \equiv -i\mathbf{L}f \quad (4.5)$$

and define the *Liouvillian* operator \mathbf{L} . The Liouville equation 4.6 is the fundamental equation of equilibrium and nonequilibrium statistical mechanics since it relates the time evolution of f to the details of atomic motion, but its importance is more formal than practical. A formalism for treating nonequilibrium dynamics using the Liouville equation is described in Section 4.2.2.

At thermal equilibrium, the Liouville equation simplifies to

$$\sum_{\alpha} \left(\frac{\partial f}{\partial \mathbf{p}_{\alpha}} \cdot \frac{\partial \mathbf{p}_{\alpha}}{\partial t} + \frac{\partial f}{\partial \mathbf{q}_{\alpha}} \cdot \frac{\partial \mathbf{q}_{\alpha}}{\partial t} \right) = 0. \quad (4.6)$$

When $f = f(\mathcal{H})$ one sees that

$$\frac{\partial f}{\partial \mathbf{p}_{\alpha}} = \frac{\partial f}{\partial \mathcal{H}} \frac{\partial \mathcal{H}}{\partial \mathbf{p}_{\alpha}} = \frac{\partial f}{\partial \mathcal{H}} \frac{\partial \mathbf{x}_{\alpha}}{\partial t} \quad \text{and} \quad \frac{\partial f}{\partial \mathbf{x}_{\alpha}} = \frac{\partial f}{\partial \mathcal{H}} \frac{\partial \mathcal{H}}{\partial \mathbf{x}_{\alpha}} = - \frac{\partial f}{\partial \mathcal{H}} \frac{\partial \mathbf{p}_{\alpha}}{\partial t}. \quad (4.7)$$

Consequently, for isolated systems (with time-independent Hamiltonians), thermal equilibrium is maintained by Hamilton's equations of motion independently of the details of the atomic-scale dynamics.

For a system of fixed N exchanging energy with its surroundings, the microcanonical ensemble is inappropriate. To illustrate, divide an energetically isolated system into two subsystems that exchange energy through the interaction of their respective particles. Labeling the subsystems particle numbers and Hamiltonians as N_1 , N_2 , \mathcal{H}_1 , and \mathcal{H}_2 , energy is exchanged between the two systems because \mathcal{H}_1 depends on atoms in system 2, and vice versa. Denoting the subsystems' energies as U_1 and U_2 , the quantities are constrained so that

$$N_1 + N_2 = N, \quad U_1 + U_2 = U, \quad dN_1 = dN_2 = 0, \quad dU_1 = -dU_2. \quad (4.8)$$

The total system is a microcanonical ensemble, so the best that can be said about the subsystems is that $\mathcal{Z}(U) = \int \mathcal{Z}_1(U_1) \mathcal{Z}_2(U - U_1) dU_1$. For macroscopic systems with N , N_1 , and N_2 large, the integral over U_1 is dominated by its largest term, occurring when $U_1 = \bar{U}_1$ and $U_2 = \bar{U}_2 \equiv U - \bar{U}_1$. To $O(\frac{1}{N})$ (this is why statistical mechanics works),

$$\mathcal{Z}(U) \sim \mathcal{Z}_1(\bar{U}_1) \mathcal{Z}_2(\bar{U}_2). \quad (4.9)$$

Moreover, at $U_1 = \bar{U}_1$

$$\frac{\partial}{\partial U_1} (\mathcal{Z}_1(U_1) \mathcal{Z}_2(U_2))_{U_1=\bar{U}_1} = 0 \quad (4.10)$$

implies that the two subsystems are constrained by

$$\left. \frac{\partial \log \mathcal{Z}_1}{\partial U_1} \right|_{U_1=\bar{U}_1} = \left. \frac{\partial \log \mathcal{Z}_2}{\partial U_2} \right|_{U_2=\bar{U}_2}. \quad (4.11)$$

This constraint defines the entropy $S_1(U_1) \equiv k_B \log \mathcal{Z}(U_1)$ and temperature $T_1 = \frac{\partial U_1}{\partial S_1}$ with similar expressions for subsystem 2.

The distribution function for the canonical ensemble is obtained in the limit that one of the subsystems is a heat reservoir providing or receiving energy to maintain the other subsystem. So, taking one of the subsystems, say the second, as a reservoir: $U_2 \gg U_1, N_2 \gg N_1$ and expanding about the state U_1

$$k_B \log \mathcal{Z}_2(U_2) = S_2(U_2) = S_2(U) - U_1 \left. \frac{\partial S_2}{\partial U_2} \right|_{U_2=U} = S_2(U) - \frac{U_1}{T}. \quad (4.12)$$

Finally, exponentiating each side yields the form of \mathcal{Z} and consequently f for subsystem 1 in the canonical ensemble where energy varies near equilibrium due to contact with a thermal reservoir

$$f(\Gamma) \propto e^{-\frac{U(\Gamma)}{kT}}. \quad (4.13)$$

Similar arguments apply to the grand canonical ensemble where the distribution function is

$$f(\Gamma) \propto e^{-\frac{U(\Gamma)-\alpha N}{kT}} \quad (4.14)$$

where α is the chemical potential which is essentially the change in energy upon adding a single particle to a system in equilibrium. The volume \mathcal{Z} in phase space occupied by the canonical and grand canonical ensembles is known as the *partition function* and is given by

$$\mathcal{Z} \equiv \frac{1}{N!h^{3N}} \int f(\Gamma) d\Gamma. \quad (4.15)$$

The constant of proportionality has been introduced for completeness but without justification. It is given for compatibility with a quantum-mechanical system where the energy U must be replaced by the Hamiltonian operator \mathcal{H} .

4.1.2 Statistical Mechanics of a Harmonic Crystal

The coupling problem is considerably simplified if the material being modeled has crystalline order, and virtually every theory or description of the dynamic behavior of a crystal makes reference to the linear or harmonic material where the atoms interact via Hooke's law. Consequently, the results of the above section will be applied to a harmonic crystal. The other relevant reason for taking the harmonic limit of the model Hamiltonian of Equation 4.1

is that the displacement–based description of finite element codes is often overlaid on the atomistic region in many coupling schemes, so that an atomic-scale description in terms of displacements may be desired.

A perfect monatomic crystal’s lattice and atomic sites \mathbf{X}_α can be generated by linear combinations of the linearly independent vectors \mathbf{a}_j

$$\mathbf{X}_\alpha = \sum_j n_j^\alpha \mathbf{a}_j. \quad (4.16)$$

For a crystal with atom α displaced to position \mathbf{x}_α , the potential energy Φ can be Taylor-expanded in terms of the displacements $\{\mathbf{u}_\alpha \equiv \mathbf{x}_\alpha - \mathbf{X}_\alpha\}$, and the result can be written as a quadratic form of the \mathbf{u}_α :

$$\Phi = \frac{1}{2} \sum_\alpha \sum_{\beta \neq \alpha} \mathbf{u}_\alpha \cdot \mathbb{D}(\mathbf{X}_\alpha - \mathbf{X}_\beta) \cdot \mathbf{u}_\beta + O(u^3) \quad (4.17)$$

provided the displacements are small, $|\mathbf{u}_\alpha| \ll |\mathbf{a}_j|$. The quantities $\mathbb{D}(\mathbf{X}_\alpha - \mathbf{X}_\beta)$ are known as dynamical matrices, and their $\mathbf{X}_{\alpha\beta} \equiv \mathbf{X}_\alpha - \mathbf{X}_\beta$ -dependence is henceforth subsumed in the notation $\mathbb{D}_{\alpha\beta} \equiv \mathbb{D}(\mathbf{X}_{\alpha\beta})$ and $\mathbb{D}_\alpha \equiv \mathbb{D}(\mathbf{X}_\alpha)$. If Φ is assumed described by pair potentials $\phi_{\alpha\beta}(\mathbf{x}_\alpha, \mathbf{x}_\beta)$, the $\mathbb{D}_{\alpha\beta}$ are given by

$$\mathbb{D}_{\alpha\beta} = \delta_{\alpha\beta} \sum_\gamma \frac{\partial^2 \phi_{\alpha\gamma}}{\partial \mathbf{x}_\alpha \partial \mathbf{x}_\gamma} - \frac{\partial^2 \phi_{\alpha\beta}}{\partial \mathbf{x}_\alpha \partial \mathbf{x}_\beta} \quad (4.18)$$

Here, the $\phi_{\alpha\beta}$ will be taken as a single central-force potential $\phi(x_{\alpha\beta})$, and Equation 4.18 can be rewritten as

$$\mathbb{D}_{\alpha\beta} = \delta_{\alpha\beta} \sum_\gamma (A_{\alpha\gamma} \mathbf{1} + B_{\alpha\gamma} \hat{\mathbf{X}}_{\alpha\gamma} \otimes \hat{\mathbf{X}}_{\alpha\gamma}) - (A_{\alpha\beta} \mathbf{1} + B_{\alpha\beta} \hat{\mathbf{X}}_{\alpha\beta} \otimes \hat{\mathbf{X}}_{\alpha\beta}) \quad (4.19)$$

with the coefficients $A_{\mu\nu}$ and $B_{\mu\nu}$ given by

$$A_{\mu\nu} \equiv \frac{1}{X_{\mu\nu}} \left| \frac{\partial \phi(x)}{\partial x} \right|_{x=X_{\mu\nu}} \quad B_{\mu\nu} \equiv \left| \frac{\partial^2 \phi(x)}{\partial x^2} - \frac{1}{x} \frac{\partial \phi(x)}{\partial x} \right|_{x=X_{\mu\nu}}. \quad (4.20)$$

When the variation of \mathbf{u}_α from site α to its neighboring ones is small, the $\mathbb{D}_{\alpha\beta}$ are related to the elastic moduli c_{ijkl} by

$$c_{ijkl} = -\frac{1}{8\Omega} \sum_\alpha (\mathbf{X}_i^\alpha \mathbb{D}_{jk}^\alpha \mathbf{X}_l^\alpha + \mathbf{X}_j^\alpha \mathbb{D}_{ik}^\alpha \mathbf{X}_l^\alpha + \mathbf{X}_i^\alpha \mathbb{D}_{jl}^\alpha \mathbf{X}_k^\alpha + \mathbf{X}_j^\alpha \mathbb{D}_{il}^\alpha \mathbf{X}_k^\alpha). \quad (4.21)$$

Here Ω is the unit cell volume, and lowercase indices denote Cartesian components of their respective vectors or matrices.

Neglecting terms that are $O(u^3)$ and higher, the equations of motion are linear

$$m_\alpha \ddot{\mathbf{u}}_\alpha = \sum_{\beta} \mathbb{D}_{\alpha\beta} \cdot \mathbf{u}_\beta, \quad (4.22)$$

and they may be Fourier-transformed to obtain

$$-m_\alpha \omega^2 \boldsymbol{\xi}_\mathbf{k}^\lambda = \sum_{\beta} \mathbb{D}_{\alpha\beta} e^{-i\mathbf{k} \cdot \mathbf{X}_{\alpha\beta}} \boldsymbol{\xi}_\mathbf{k}^\lambda \equiv \mathbb{D}^\mathbf{k} \boldsymbol{\xi}_\mathbf{k}^\lambda. \quad (4.23)$$

The original linear system for the N -atom crystal has been diagonalised yielding $3N$ independent normal modes propagating according to the N wavevectors \mathbf{k}

$$\mathbf{u}_\alpha = \sum_{\mathbf{k}, \lambda} \boldsymbol{\xi}_\mathbf{k}^\lambda e^{-i(\mathbf{k} \cdot \mathbf{X}_\alpha - \omega(\mathbf{k})t)}. \quad (4.24)$$

The wavevector \mathbf{k} is a reciprocal lattice vector while the direction, amplitude, and phase of the motion are contained in the complex vector $\boldsymbol{\xi}_\mathbf{k}^\lambda$ with $\lambda = 1..3$ indexing modes for each \mathbf{k} . The normal mode transformation diagonalizes the Hamiltonian so that it may be written in terms of generalized momenta $\{p_\mathbf{k}^\lambda\}$ and positions $\{q_\mathbf{k}^\lambda\}$ as

$$\mathcal{H} = \sum_{\mathbf{k}, \lambda} \left(\frac{|p_\mathbf{k}^\lambda|^2}{2} + \omega(\mathbf{k})^2 \frac{|q_\mathbf{k}^\lambda|^2}{2} \right). \quad (4.25)$$

The relation between $p_\mathbf{k}^\lambda$, $q_\mathbf{k}^\lambda$, and the normal modes of the crystal is

$$q_\mathbf{k}^\lambda = \omega(\mathbf{k}) |\boldsymbol{\xi}_\mathbf{k}^\lambda| e^{-i\omega(\mathbf{k})t}, \quad p_\mathbf{k}^\lambda = \dot{q}_\mathbf{k}^\lambda. \quad (4.26)$$

The modes are independent in the sense that a crystal described by Equation 4.22 and excited to a single mode remains in that mode indefinitely—modes do not interact. This statement is not true in general for nonlinear equations of motion.

Since the harmonic crystal has a diagonal Hamiltonian, the partition function can be written as a product over normal modes

$$\mathcal{Z} \propto \prod_{\mathbf{k}, \lambda} \left[\int e^{-\frac{(p_\mathbf{k}^\lambda)^2}{2k_B T}} dp_\mathbf{k}^\lambda \int e^{-\frac{(\omega(\mathbf{k})q_\mathbf{k}^\lambda)^2}{2k_B T}} dq_\mathbf{k}^\lambda \right], \quad (4.27)$$

and each integral may be evaluated separately. It is straightforward to evaluate the mean kinetic energy, $\mathcal{T}_\mathbf{k}^\lambda$ or potential energy, $\mathcal{U}_\mathbf{k}^\lambda$ of a given mode using Equation 4.3 to obtain the important result that

$$\mathcal{T}_\mathbf{k}^\lambda = \mathcal{U}_\mathbf{k}^\lambda = \frac{k_B T}{2}. \quad (4.28)$$

The total energy of the crystal is thus $6Nk_B T$, and the normal mode amplitudes may be obtained from Equation 4.26 as

$$|\boldsymbol{\xi}_\mathbf{k}^\lambda|^2 = \frac{k_B T}{2\omega(\mathbf{k})^2}. \quad (4.29)$$

Of course, this approach can say nothing about the phases of each normal mode.

The results of this section may also be obtained using either the *generalized equipartition theorem*,

$$\left\langle p \frac{\partial \mathcal{H}}{\partial p} \right\rangle = \left\langle q \frac{\partial \mathcal{H}}{\partial q} \right\rangle = \frac{k_B T}{2}, \quad (4.30)$$

or the *virial theorem*,

$$\left\langle \sum_{i=1}^{3N} q_i \dot{p}_i \right\rangle = -3Nk_B T. \quad (4.31)$$

Both of these theorems are valid for arbitrary Hamiltonians, but their derivation is more lengthy than the brute-force approach used here. Most importantly, for the vast number of systems with Hamiltonians whose kinetic energy has the same form as in Equation 4.1, one has

$$\left\langle \frac{1}{2m_\alpha} \mathbf{p}_\alpha \cdot \mathbf{p}_\alpha \right\rangle = \frac{3}{2} k_B T. \quad (4.32)$$

For the harmonic Hamiltonian, the generalized equipartition theorem confirms Equation 4.28 so that the average kinetic and potential energies are equal, but this result does not hold for a more general potential.

Finally, these results were obtained in the canonical ensemble, so the energy is not strictly constant but rather fluctuates about the mean values found above. For statistical mechanics to be valid, the fluctuations must be small, and they may be characterized by the variance of the Hamiltonian and calculated using the partition function

$$\langle \delta \mathcal{H}^2 \rangle \equiv \langle (U - \mathcal{H})^2 \rangle = \langle \mathcal{H}^2 \rangle - \langle \mathcal{H} \rangle^2 = 6Nk_B T^3. \quad (4.33)$$

As $N \rightarrow \infty$, the fluctuations become infinitesimal relative to U (which varies as N^2), and the equilibrium ensemble is equivalent to the microcanonical one.

4.2 Nonequilibrium Statistical Mechanics

4.2.1 Overview

Equilibrium statistical mechanics can only treat uniform macroscopic behavior, but any MD–FE coupling at nonzero temperature may involve significant non–uniform or transient material states. A weakness of the statistical treatment is that little reconciliation can be affected between the macroscopic and microscopic viewpoints without f , and there are few ways to reasonably obtain it away from equilibrium where even the most basic theory can still be debated.

The only spatial inhomogeneity that can be well-treated is coupling to an external field in linear response theory (Section 4.2.4). Likewise, the only temporal inhomogeneity treated in equilibrium statistical mechanics is relaxation to equilibrium after a fluctuation, and this treatment is through linear response theory as well. Beyond linear response theory, a statistically unlikely nonequilibrium state transforms itself into a statistically likely equilibrium state through internal evolution as well as interaction with its surroundings. Often, the internal and external interactions occur over vastly different timescales so that some sort of internal equilibrium is achieved long before equilibrium with the surroundings is achieved. In a normal mode language, high frequency modes correspond to rapid relaxation times since they typically have short mean free paths while low frequency modes have longer mean free paths and relaxation times and require much more global rearrangement (Section 4.2.5).

The treatment of temporal and spatially-inhomogeneous phenomena in a statistical framework begins by considering correlated response to disturbances, and such considerations lead to a generalized Langevin equation that treats the "chaotic" microscopic motion statistically. More phenomenologically, the major "textbook" [61, 62, 63, 64, 65, 66] components of nonequilibrium statistical mechanics are the linear response of systems to small deviations from thermal equilibrium or coupling to an external field and local equilibrium configurations where macroscopically large subsystems of the still larger nonequilibrium system act as if in equilibrium. To consider stronger deviations from the macroscopic homogeneity required of a system in thermal equilibrium, one may continue to work in an equilibrium-based framework and use hydrodynamics or kinetic theory to treat macro- and meso-scale deviations from equilibrium, respectively. Another approach is to formulate a nonequilibrium theory from scratch, generalizing the equilibrium definitions of macroscopic quantities to depend on a larger set of variables. These aspects are summarized in turn.

4.2.2 Ensemble Equations of Motion

For nonequilibrium systems, the distribution function has time dependence if the system is relaxing towards equilibrium or perturbed from equilibrium. The Liouville Equation (Eq. 4.6) has the formal solution

$$f(t) = e^{-iLt} f(0) \tag{4.34}$$

which could in principle describe relaxation to equilibrium. More importantly, for *phase quantities* $\mathcal{A}(\Gamma)$ (i.e. functions of the atomic coordinates and momenta), Eq. 4.6 implies that the phase quantities evolve according to

$$\frac{d\mathcal{A}}{dt} = iL\mathcal{A}. \tag{4.35}$$

Its formal solution is

$$\mathcal{A}(t) = e^{iLt} \mathcal{A}(0), \tag{4.36}$$

and time-dependent ensemble averages can be written as

$$\langle \mathcal{A}(t) \rangle \equiv \int \mathcal{A}(0) f(t) d\Gamma = \int \mathcal{A}(0) e^{-iLt} f(0) d\Gamma = \int \mathcal{A}(t) f(0) d\Gamma. \quad (4.37)$$

Ensemble averages in time-dependent systems can be thought of as an average of $\mathcal{A}(0)$ over all initial microstates with distribution governed by $f(t)$ (first integral in 4.37), or the average may be taken over all current microstates subject to the initial distribution (final integral above). Equilibrium distribution functions and equilibrium ensemble averages are stationary in times.

Liouville's equation has too many degrees of freedom for numerical treatment, but macroscopic response can be related to microscopic motion and inhomogeneities through a formalism introduced by Zwanzig[67] and refined by Mori[68] that uses Equation 4.37 as the basis for an inner product space. For phase quantities \mathcal{A} and \mathcal{B} , the inner product is the correlation function $C_{\mathcal{A}\mathcal{B}}$

$$C_{\mathcal{A}\mathcal{B}}(t) = \langle \mathcal{A}(0), \mathcal{B}(t) \rangle \equiv \int \mathcal{B}(t) f \mathcal{A}(0) d\Gamma. \quad (4.38)$$

The time dependence of f is suppressed above to emphasize that this is an equilibrium ensemble average and hence stationary in time. The physical interpretation of this inner product is that orthogonal vectors are uncorrelated. Projection operators \mathbf{P} and $\mathbf{Q} \equiv 1 - \mathbf{P}$ decompose \mathcal{B} into components parallel and orthogonal to \mathcal{A}

$$\mathbf{P}\mathcal{B}(t) = \frac{\langle \mathcal{A}, \mathcal{B}(t) \rangle}{\langle \mathcal{A}(0), \mathcal{A}(0) \rangle} \mathcal{A} = \frac{C_{\mathcal{A}\mathcal{B}}(t)}{C_{\mathcal{A}\mathcal{A}}(0)} \mathcal{A}. \quad (4.39)$$

Equation 4.35 can now be written as

$$\frac{d\mathcal{A}(t)}{dt} = e^{iLt} i(\mathbf{P} + \mathbf{Q})L\mathcal{A}(0). \quad (4.40)$$

The \mathbf{P} -term is the component of $iL\mathcal{A}(0) = \dot{\mathcal{A}}(t)$ parallel to \mathcal{A} , so the only difficulty is the treatment of the \mathbf{Q} -term above. A few operator identities (see Chapters 3 and 4 of Evans [63] for a complete derivation) allow the uncorrelated term to be written as the sum of two terms. The simplest term is local in time, uncorrelated with \mathcal{A} , and usually called the random force, $F_{\mathcal{A}}(t)$. The final term arising from the \mathbf{Q} -term in Equation 4.40 has a nonzero correlation with \mathcal{A} arising from the cumulative effect of random forces over time. Finally, these three terms give the *generalized Langevin equation* for \mathcal{A} :

$$\frac{\partial \mathcal{A}}{\partial t} = C_{\dot{\mathcal{A}}\mathcal{A}}/C_{\mathcal{A}\mathcal{A}}\mathcal{A}(t) - \int_0^t K(t')\mathcal{A}(t-t') dt' + F_{\mathcal{A}}(t). \quad (4.41)$$

The first term is the equal-time, spatially-correlated response from the \mathbf{P} term, and the history-dependent memory kernel is given in terms of the random force as

$$K(t) = \langle F_{\mathcal{A}}(t)\mathcal{A}(0) \rangle C_{\mathcal{A}\mathcal{A}}^{-1}(0). \quad (4.42)$$

For all but the simplest systems, $K(t)$ is unknown and must be computed numerically [69].

Langevin or projection-operator based formalisms have been extended to treat coordinates and momenta symmetrically [70], inhomogeneous systems [71], and nonequilibrium MD simulations [72, 73]. Langevin or conceptually-related equations have also been applied to atomistic simulations as a thermostat [74], to coarse grain in time [75] and space [76], and to smooth over time [77]. The Laplace-transforms of L , P , and Q that are at the heart of the operator identities leading to the generalized Langevin equation serve similar duty in the bridging-scale formalism of Wagner [12].

4.2.3 Microscopic balance laws and hydrodynamics

Generally, hydrodynamics refers to the description of processes that occur much more slowly than microscopic relaxation times and only describes processes where the magnitude of the wavevector \mathbf{k} approaches zero and frequency $\omega(\mathbf{k}) = c|\mathbf{k}|$. In solids, then, hydrodynamic modes are sound waves, and displacement by a long-wavelength wave is locally equivalent to an energetically-degenerate uniform translation of the crystal. Modes satisfying these restrictions obey macroscopic balance equations to low order in small \mathbf{k} , and these restrictions and results follow a macroscopic, phenomenological treatment of hydrodynamics [78]. In a more thermodynamic, yet still phenomenological, picture, enough high-frequency collisions occur during a low-frequency hydrodynamic excitation to maintain some sort of equilibrium.

In 1950, Irving and Kirkwood considered ensemble averages of microscopic balance laws for a swarm of particles interacting through pair potentials[79]. They demonstrated that the above results also arise from a microscopic formalism that is relevant to the atomistic-continuum coupling problem. An atomic quantity $\mathcal{A}^\alpha(t)$ formally exists only at atom α 's instantaneous position $\mathbf{x}^\alpha(t)$ (i.e. these are Lagrangian coordinates). A field $\mathcal{A}(\mathbf{x}, t)$ is defined by

$$\mathcal{A}(\mathbf{x}, t) = \sum_{\alpha} \mathcal{A}_{\alpha}(t) \delta(\mathbf{x}_{\alpha}(t) - \mathbf{x}) \quad (4.43)$$

with $\delta(\mathbf{x})$ the Dirac delta function. The units of \mathcal{A} are those of the $\{\mathcal{A}^\alpha\}$ divided by the volume, the latter factor arising from $\delta(\mathbf{x})$, and the time dependence of field quantities will be suppressed in the following, $\mathcal{A}(\mathbf{x}) \equiv \mathcal{A}(\mathbf{x}, t)$. For a thermodynamic system, the quantities of interest are the number, mass, momentum, and energy densities. They are respectively

given by the following formulae:

$$n(\mathbf{x}) = \sum_{\alpha} \delta(\mathbf{x}_{\alpha}(t) - \mathbf{x}) \quad (4.44)$$

$$\rho(\mathbf{x}) = \sum_{\alpha} m_{\alpha} \delta(\mathbf{x}_{\alpha}(t) - \mathbf{x}) \quad (4.45)$$

$$\mathbf{p}(\mathbf{x}) = \sum_{\alpha} m_{\alpha} \mathbf{v}_{\alpha} \delta(\mathbf{x}_{\alpha}(t) - \mathbf{x}) \quad (4.46)$$

$$e(\mathbf{x}) = \sum_{\alpha} \left(\frac{1}{2} m_{\alpha} \mathbf{v}_{\alpha} \cdot \mathbf{v}_{\alpha} + \phi_{\alpha} \right) \delta(\mathbf{x}_{\alpha}(t) - \mathbf{x}) \quad (4.47)$$

The flow velocity $\mathbf{v}(\mathbf{x})$ is defined such that

$$\rho(\mathbf{x}) \mathbf{v}(\mathbf{x}) = \mathbf{p}(\mathbf{x}), \quad (4.48)$$

and local relative velocities $\mathbf{u}_{\alpha}(\mathbf{x})$ via $\mathbf{u}_{\alpha}(\mathbf{x}) \equiv \mathbf{v}_{\alpha} - \mathbf{v}(\mathbf{x})$. Computing the time derivatives of the above quantities allows the establishment of conservation laws

$$\frac{\partial n}{\partial t} = -\nabla \cdot \mathbf{j}_n \quad (4.49)$$

$$\frac{\partial \rho}{\partial t} = -\nabla \cdot \rho \mathbf{v} \quad (4.50)$$

$$\frac{\partial (\rho \mathbf{v})}{\partial t} = \nabla \cdot (\sigma - \rho \mathbf{v} \otimes \mathbf{v}) \quad (4.51)$$

$$\frac{\partial e}{\partial t} = \nabla \cdot (\mathbf{v} \cdot \sigma - e \mathbf{v} - \mathbf{q}) \quad (4.52)$$

The undefined quantities in the conservation laws follow:

$$\mathbf{j}_n(\mathbf{x}) = \sum_{\alpha} \mathbf{v}_{\alpha} \delta(\mathbf{x}_{\alpha}(t) - \mathbf{x}) \quad (4.53)$$

$$\mathbf{q}(\mathbf{x}) = \sum_{\alpha} \left(\left(\frac{1}{2} m_{\alpha} \mathbf{u}_{\alpha} \cdot \mathbf{u}_{\alpha} + \phi_{\alpha} \right) \mathbf{u}_{\alpha} - \frac{1}{2} \sum_{\beta \neq \alpha} \mathbf{x}_{\alpha\beta} (\mathbf{u}_{\alpha} \cdot \mathbf{F}_{\alpha\beta}) \right) \delta(\mathbf{x}_{\alpha}(t) - \mathbf{x}) \quad (4.54)$$

$$\sigma(\mathbf{x}) = \sum_{\alpha} \left(m_{\alpha} \mathbf{u}_{\alpha} \otimes \mathbf{u}_{\alpha} \delta(\mathbf{x}_{\alpha}(t) - \mathbf{x}) - \frac{1}{2} \sum_{\beta \neq \alpha} \mathbf{x}_{\alpha\beta} \otimes \mathbf{F}_{\alpha\beta} B_{\delta}^{\alpha\beta}(\mathbf{x}) \right) \quad (4.55)$$

where $B_{\delta}^{\alpha\beta}(\mathbf{x})$ is given by

$$B_{\delta}^{\alpha\beta}(\mathbf{x}) = \int_0^1 \delta(\mathbf{x}_{\beta} + \lambda \mathbf{x}_{\alpha\beta} - \mathbf{x}) d\lambda. \quad (4.56)$$

The statistical-mechanical quantities Irving and Kirkwood considered are ensemble averages of the above fields

$$\mathcal{A}_{SM} = \langle \mathcal{A} \rangle. \quad (4.57)$$

They used Dirac δ -functions for their ensemble averages and merely stated that spatial and time averages are necessary to obtain the macroscopic balance laws from these microscopic ones.

Hardy's corresponding value $\mathcal{A}_H(\mathbf{x})$ [52] is obtained by averaging \mathcal{A} over space with the weighting function $\psi(\mathbf{x})$,

$$\mathcal{A}_H(\mathbf{x}) = \int \mathcal{A}(\mathbf{x} - \tilde{\mathbf{x}}) \psi(\tilde{\mathbf{x}}) d\tilde{\mathbf{x}} = \sum_{\alpha} \mathcal{A}_{\alpha}(t) \psi(\mathbf{x}_{\alpha}(t) - \mathbf{x}). \quad (4.58)$$

Derivatives with respect to space and time commute with spatial-averaging; since the microscopic quantities satisfy balance laws for number density, mass, momentum, and energy, Hardy's averaged quantities do as well.

To obtain the hydrodynamic (i.e. long wavelength) limit of these balance laws, Irving and Kirkwood do not leave B_{δ} in their macroscopic balance equations. They carry out an ensemble average to transform B_{δ} to an integral of the pair correlation function, $g^{(2)}(\mathbf{r}, \mathbf{R})$ giving the probability of finding a particle at $\mathbf{r} + \mathbf{R}$ given one at \mathbf{r} . They retain only the dominant terms in the Taylor expansion of the averaged B_{δ} , yielding for the configurational contribution to the stress tensor

$$\frac{\langle \rho(\mathbf{x}) \rangle^2}{2m^2} \int \frac{\mathbf{R} \otimes \mathbf{R}}{R} \frac{d\phi}{dR} g^{(2)}(\mathbf{x}, \mathbf{R}) d\mathbf{R}, \quad (4.59)$$

where ϕ is the (assumed) pairwise, centrosymmetric interaction potential. Alternatively, these equations can be (and often are) Fourier-transformed and developed in \mathbf{k} -space, too. An advantage of this procedure is that the hydrodynamic or continuum limit is readily available as the small- \mathbf{k} limit, simplifying considerably the derivation of the quantities that require the bond function for their determination.

The Irving and Kirkwood procedure shows that microscopic balance equations are satisfied dynamically and by the ensemble-averaged quantities. The passage to the hydrodynamic limit occurs when the corresponding macroscopic quantities vary slowly over microscopic scales. In terms of a mean free path l and collision time τ , $|\mathbf{k}|l \ll 1, \omega\tau \ll 1$ determine the wave number and frequency responses well-treated by hydrodynamics. In the hydrodynamic limit, the distribution function is the equilibrium one, the macroscopic mass, energy, and number densities behave as the averaged microscopic ones, and the continuum balance laws are achieved.

4.2.4 Linear Response

The equations of hydrodynamics are valid under many conditions, but they must be completed by constitutive relations, which to a first approximation are assumed to be linear between flux and driving force. Calculation of these linear macroscopic quantities from the microscopic properties of a material is the concern of the linear response formalism, which begins by considering the weak deviations from equilibrium where linearity may be expected to hold.

In the canonical ensemble, a heat bath is used as a means of introducing or quantifying internal energy fluctuations $\delta U(t) \equiv U(t) - \langle U \rangle$ in the system. For equilibrium systems, the likelihood $p(\delta U)$ of a fluctuation depends on the entropy change $\delta S(\delta U)$ it produces:

$$p(\delta U) \propto e^{-\frac{\delta S(\delta U)}{k_B}}, \quad (4.60)$$

and similar formulae hold for fluctuations in other macroscopic quantities. Equivalently, these fluctuations are Gaussian random processes in the thermodynamic limit since entropy is maximized and terms higher than second order in the expansion of Equation 4.60 are negligible. Consequently, fluctuations of $\mathcal{A}(t)$ are characterized entirely by the ensemble average of the second moment $\langle \delta \mathcal{A}^2 \rangle \equiv \langle \mathcal{A}^2 \rangle - \langle \mathcal{A} \rangle^2 \neq 0$, and comparison of the second to higher moments of the momentum distribution in an MD simulation provides an effective measure of how equilibrated the region is. The exact form of the variances of fluctuating quantities depends on the ensemble used, and the application to MD simulations is treated in Reference [80]. Fluctuations in nonequilibrium systems are examined in Reference [81].

There is also an intimate relation between fluctuations in macroscopic quantities and the final stages of relaxation towards equilibrium. Statistical mechanics traditionally views the system-heat bath interaction as one between a subsystem and its surrounding material. Consequently, the mechanisms of energy exchange between system and reservoir are the same as those of energy transport within the system, or more strongly, if an equilibrium system is experiencing a fluctuation, it is impossible to know the system is at equilibrium until the fluctuation dissipates.

Assuming a linear relation between response and driving force, the constant of proportionality can be calculated from ensemble averages depending on either a quantity or its time derivative. To make the discussion definite, consider heat transport where the driving force for heat flux $\langle \mathbf{q} \rangle$ is the temperature gradient ∇T . The heat equation

$$\frac{\partial T}{\partial t} = \nabla \cdot \langle \mathbf{q} \rangle \quad (4.61)$$

is completed by the linear constitutive law of Fourier

$$\langle \mathbf{q} \rangle = -\kappa \nabla T \quad (4.62)$$

with the thermal conductivity denoted κ . The heat flux is written as $\langle \mathbf{q} \rangle$ rather than \mathbf{q} to emphasize that the proper quantity appearing in Fourier's law is an ensemble average of a microscopic heat flux such as Hardy's \mathbf{q} .

The first form for the conductivity is an *Einstein relation* that becomes exact in the long time limit

$$\kappa = \lim_{t \rightarrow \infty} \frac{1}{2VkT^2t} \langle (\mathcal{J}_{\mathbf{q}}(t) - \mathcal{J}_{\mathbf{q}}(0))^2 \rangle, \quad (4.63)$$

where $\frac{\partial}{\partial t} \mathcal{J}_{\mathbf{q}} \equiv \mathbf{q}$. This equation is obtained by calculating the average response to a temperature perturbation at the origin, so Fourier's law is assumed and then shown to have validity in the small- k limit.

Equivalent to the Einstein relation is the *Green-Kubo* relation which relates the thermal conductivity to an autocorrelation function

$$\kappa = \frac{1}{VkT^2} \int_0^\infty C_{\mathbf{q}\mathbf{q}}(t) dt, \quad (4.64)$$

following from Equation 4.63 by the definition of the derivative and that equilibrium ensemble averages are stable with respect to time averages. In the above equation, the thermal conductivity is a scalar and the correlation function is $\langle \mathbf{q}(t) \cdot \mathbf{q}(0) \rangle$ since the ensemble average yields isotropic response. The quantities appearing in the Green-Kubo relations are time derivatives of the quantities appearing in the Einstein relations, and an advantage of these linear relations is that, by the ergodic hypothesis, they require no knowledge of the distribution function and can be computed from MD simulations.

Since the constitutive laws obtained by Einstein or Green-Kubo relations are derived from a perturbation of the distribution function, it is possible to treat nonlinear response by continuing the perturbation expansion further. This continued expansion is not treated here since it is confined to mechanical effects that can be represented in the Hamiltonian as an external field. Such a representation is not practically possible with thermal variables, so nonlinear response is of limited utility in the atomistic-continuum coupling problem. Linear response theory suffers from this same shortcoming, but there are enough different derivations of the linear constitutive laws for the thermal conductivity that one does not have to explicitly represent the temperature gradient as a mechanical perturbation.

4.2.5 Local Equilibrium

For a system subject to perturbation by external fields, there are well-developed techniques for computing both linear and non-linear response of nonequilibrium systems. For a system subject to a thermal perturbation or prescribed temperature fields, the machinery used for

arbitrary external fields can only be applied by esoteric mappings converting the temperature variation into a mechanical one.

The most intuitive description of a weakly nonequilibrium system is one where small portions of the system act as if they are essentially in equilibrium, although macroscopic quantities may vary spatially. This Local Equilibrium (LE) hypothesis is essentially the underlying assumption of thermomechanical models where it is assumed that temperature, energy, and entropy fields completely describe a body (although in reality the thermomechanical continuum is described by rational thermodynamics[82] which is an extension of classical thermodynamics rather than modern statistical mechanics), and LE is the underlying assumption of hydrodynamics (previous Section) and kinetic theory (Section 4.2.7). To achieve this local equilibration, one demands that high-frequency modes (short lifetimes, 'chaotic' atomic motion) quickly thermalize while long wavelength modes responsible for collective motion towards global relaxation thermalize much more slowly[83, 84]. For an inverse temperature field $\beta(\mathbf{x}, t) \equiv 1/kT(\mathbf{x}, t)$ and fields for the Hamiltonian density $\mathcal{H}(\mathbf{x})$, number density $n(\mathbf{x})$, and chemical potential $\mu(\mathbf{x})$, the system as a whole has the grand-canonical distribution function

$$f(t) \sim e^{-\int \beta(\mathbf{x}, t)(\mathcal{H}(\mathbf{x}, t) - \mu(\mathbf{x}, t)n(\mathbf{x}, t)) d\mathbf{x}}. \quad (4.65)$$

The proportionality constant is determined by the normalization of f over phase space. For a system with flow velocity field $\mathbf{v}(\mathbf{x})$, the energy \mathcal{H} appearing above must be in the commoving frame (at local equilibrium $\mathbf{v}(\mathbf{x}) = 0$), and Equation 4.65 is generalized to

$$f(t) \sim e^{-\int \beta(\mathbf{x}, t) [\mathcal{H}(\mathbf{x}, t) - \mu(\mathbf{x}, t)n(\mathbf{x}, t) - \frac{1}{2}\rho(\mathbf{x})\mathbf{v}(\mathbf{x}) \cdot \mathbf{v}(\mathbf{x})] d\mathbf{x}}. \quad (4.66)$$

Beyond these global distribution functions, the heart of the LE hypothesis is that local ensemble averages can also be computed based on the values of the fields at arbitrary \mathbf{x} . The internal energy density field $U(\mathbf{x}, t) = \langle \mathcal{H}(\mathbf{x}) - \frac{1}{2}\rho(\mathbf{x})v(\mathbf{x})^2 \rangle$ corresponds to the ensemble or time average of Hardy's thermal energy density $e_t(\mathbf{x})$ and includes both strain energy and thermal vibrations unless strain (or stress) is explicitly incorporated into the ensemble as an independent macroscopic variable. The chemical potential need have no direct relevance to Hardy's formalism unless an external field is acting on the system or it is necessary to couple MD simulations from a nonconstant- N ensemble to the continuum.

Virtually any definition of a temperature field in an MD or coupled system that relies on an equilibrium measure of temperature is beholden to the local equilibrium hypothesis for its justification. The local equilibrium approach has the virtue of being intuitive and relatively easy to visualize compared to most statistical descriptions of mechanical systems, but it can fail in the implementation for there is *a priori* no completely general way to define it as a molecular dynamics post-processing step.

The LE distribution function of Equation 4.66 does not admit transport processes, for the flow velocity and current densities necessarily have ensemble averages of zero in the local

frame. In order to incorporate transport processes, Equations 4.66 and 4.65 are generalized as in the linear response to a perturbation field, and no new results are produced. To first order, then, there is no operational need to distinguish between a local equilibrium calculation and a global equilibrium one. It may be that higher order local equilibrium corrections (which show up, for instance, if the distribution of fluctuations is seen to deviate from the Gaussian equilibrium) are important to ensure that a local equilibrium formalism is applied correctly.

The LE hypothesis is often invoked to explain results and concepts and less often tested. It is semi-directly tested in an MD simulation of shear fluid flow [85] where a form of local averaging is used to smooth over thermodynamic quantities and test if the local velocity distribution is consistent with an LE one. Another test of the range of validity of the LE hypothesis is applied to a ϕ^4 field theory and the Fermi-Past-Ulam model by Aoki and Kusnezov [86, 87, 88].

4.2.6 Extended Irreversible Thermodynamics

To go beyond the LE approach and describe more general short-time, high-frequency phenomena, one must either know the distribution of microstates during the nonequilibrium process or construct a more robust theory. In the latter approach, equilibrium statistical mechanics is extended to depend on macroscopic variables capable of characterizing thermal and spatial inhomogeneities. This *extended irreversible thermodynamics* (EIT) formalism constructs an entropy and hence a distribution function that depends on heat flux and other dissipative fluxes [89, 66] characteristic of the problem being studied in the same manner that one is free to choose the macroscopic quantities of equilibrium statistical mechanics that define the ensemble of interest. In another sense, EIT attempts to extend the description of hydrodynamics (Section 4.2.3) by admitting the fluxes as primary quantities that are no longer constrained to obey linear and local constitutive laws.

Formally, there is very little difference between equilibrium statistical mechanics and EIT beyond the generalizations involved in the extended variable set. For instance, if the heat flux \mathbf{q} is the only new variable introduced as a macroscopic parameter, the entropy S is a function of internal energy U and \mathbf{q}

$$dS = \left(\frac{\partial S}{\partial U} \right)_{\mathbf{q}} dU + \left(\frac{\partial S}{\partial \mathbf{q}} \right)_U \cdot d\mathbf{q}. \quad (4.67)$$

The equilibrium expressions for the macroscopic quantities become leading terms in expansions depending on the dissipative fluxes. For example, a nonequilibrium temperature is defined by the reciprocal of the first term on the right hand side above:

$$T^{-1}(U, (\mathbf{q})) \equiv \left(\frac{\partial S}{\partial U} \right)_{\mathbf{q}} \sim T_{eq}^{-1}(U) + a(U)\mathbf{q} \cdot \mathbf{q}, \quad (4.68)$$

where T_{eq} is the typical equilibrium definition of temperature [90]. A review and critique of the EIT approach to temperature is given by Eu and Garcı-Colın [91]. Equation 4.67 implies there is an additional thermodynamic quantity conjugate to \mathbf{q} and proportional to the derivative with respect to \mathbf{q} , and this term describes the entropy flux’s dependence on \mathbf{q} [66], which is proportional to $\mathbf{q} \cdot \mathbf{q}$ near the equilibrium state.

Among the appealing results of EIT are that it is able to obtain the Maxwell-Cattaneo telegraph equation for thermal conductivity as the evolution equation for \mathbf{q} while LE treatments cannot go beyond Fourier’s Law. However, the procedure used to obtain this heat conduction equation is subject to the same process of dropping higher-order terms and introducing linear relationships that occur in LE thermodynamics; the only difference is the extended parameter space. Without stronger developments in experimental verification or validation by simulation, EIT has no more fundamental claim to correctness than the more classical treatments it supplants. Consequently, any attempt to apply statistical-mechanical results to the problem of atomistic-continuum coupling must ultimately be labelled phenomenological.

4.2.7 Kinetic Theory

When attempting to incorporate nonequilibrium effects into the distribution function and to go beyond the hydrodynamic limit and handle terms higher than order k^2 , the more sophisticated approach of kinetic theory and the Boltzmann transport equation must be used. The basic tenet of kinetic theory is to treat the particles as occasionally colliding but otherwise independently distributed. In the independent limit, the distribution function decomposes into products of 1-particle distribution functions, and the effect of collisions is seen in their modification of the distribution functions after a collision. In fluids, collisions are collisions, while in solids, collisions are phonon creation and annihilation processes. Most decompositions are aimed at treating the fluid case, although some effort has been exerted to treat solids explicitly. [92] More often solids are treated as a phonon gas, and the results for the theory applied to fluids carry over more directly. [93] The distribution function for a 1D phonon gas experiencing a heat flux has been obtained by Camacho. [94] A more in-depth treatment of the phonon transport and the Boltzmann transport equation is available. [95]

4.3 Relevance to the Coupling Problem

The coupling approach of replacing atomistic regions experiencing only long-wavelength disturbances (i.e. at the continuum limit) with less computationally-expensive finite elements is relatively well-defined for mechanical equilibrium at zero temperature. For *thermal* equilibrium, the continuum limit of an atomic system is approached only in an average sense

since displacement and velocity fluctuations necessarily have short wavelength components. For a nonequilibrium system at nonzero temperature, the situation is further complicated by the possible presence of temperature gradients and flow.

For the thermal equilibrium, spatially uniform system, the timescale for obtaining the continuum limit in an MD system is much longer than either the MD or FE timestep would be in practice. If this were not so, there would be no need to simulate the atoms. Consequently, it is an open question what form an appropriate continuum constitutive model should take for the nonzero temperature coupling problem. Regardless of constitutive models or timescale effects, the N^{-1} -dependence of fluctuations on particle number has difficult implications for any attempt to transfer thermodynamically-significant information between the MD and FE regions. For a typical coupling problem, there may be 10^2 atoms per finite element; fluctuations could be considerable. These fluctuations make it difficult to define a meaningful temperature field. At best, correspondence between a coupled simulation and an MD simulation of equivalent systems at nonzero temperature can be expected in the case of thermal equilibrium, and the equivalence is only validated after appropriate averaging is carried out.

To be more quantitative the dynamics of coarse-grained variables, assumed to be analogous to the FE degrees of freedom in a coupled simulation, are considered. The coarse grained displacements $\bar{\mathbf{u}}_i, i \in \{1..N_{CG}\}, N_{CG} < N$ obtained from atomic displacements $\mathbf{u}_\alpha, \alpha \in \{1..N\}$

$$\bar{\mathbf{u}}_i = \mathbb{P}_{i\alpha} \mathbf{u}_\alpha. \quad (4.69)$$

We adopt the convention that Arabic subscripts label coarse-grained quantities while Greek subscripts continue to label atomic quantities. As written, the projection operator acts independently on each component of the atomic displacements. Equivalent notations may be developed with the operators as matrices acting on the concatenation of all displacement vectors, [12] or as higher-order tensors like $\mathbb{P}_{i\alpha} \delta_{j\beta}$. To retain only the essential indices, the most compact notation is preferred here.

This form of coarse graining is compatible with Rudd and Broughton’s CGMD method, [10], Wagner’s bridging scale method, [12] the quasistatic coupling of Chapter 2, and Hardy’s formulae for regular meshes. [52] The terminology used below is mainly from the bridging scale method. The coarse-grained variables can be identified with finite-element nodes and finite element shape functions interpolating between the nodal displacements can determine a “coarse scale” portion of each atom’s displacement \mathbf{u}_α

$$\bar{\mathbf{u}}_\alpha = \bar{\mathbf{u}}(\mathbf{X}_\alpha) = \mathbb{N}_{\alpha i} \bar{\mathbf{u}}_i = \mathbb{P}_{\alpha\beta} \mathbf{u}_\beta. \quad (4.70)$$

The $N \times N_{CG}$ matrix $\mathbb{N}_{\alpha i}$ interpolates the displacement field from the nodal values while the $N \times N$ projection matrix $\mathbb{P}_{\alpha\beta}$ performs the equivalent operation on the atomic displacements. Consequently, the projection \mathbb{P} is the composition of \mathbb{N} and \mathbb{P} , $\mathbb{P} = \mathbb{N} \cdot \mathbb{P}$. The total atomic

displacements can be written as the sum

$$\mathbf{u}_\alpha = \bar{\mathbf{u}}_\alpha + \mathbf{u}'_\alpha, \quad (4.71)$$

where the remainder $\mathbf{u}'_\alpha = (\delta_{\alpha\beta} - \mathbb{P})\mathbf{u}_\beta \equiv \mathbb{Q}_{\alpha\beta}\mathbf{u}_\beta$ is denoted the “fine scale” component. The exact form of the operator \mathbb{P} is determined by the nodal locations and interpolating functions. [10, 12] The nodal locations, choice of interpolating functions, and atomic reference configuration completely determines \mathbb{N} . The $\{\bar{\mathbf{u}}_i\}$ are chosen to minimize

$$\sum_{\alpha} m_{\alpha} \mathbf{u}'_{\alpha} \cdot \mathbf{u}'_{\alpha}, \quad (4.72)$$

which implies

$$\mathbb{P} = (\mathbb{N}^T \mathbb{M} \mathbb{N})^{-1} \mathbb{N}^T \mathbb{M}, \quad M_{\alpha\beta} = m_{\alpha} \delta_{\alpha\beta} (\text{no sum on } \alpha). \quad (4.73)$$

Finally, there are the useful relationships $\mathbb{P}^2 = \mathbb{P}$ and $\mathbb{P} \cdot \mathbb{Q} = 0$. These operators are time independent, so that coarse scale velocity or momenta are obtained by convolving the atomic velocities or momenta, respectively, rather than the atomic displacements. In Fourier space, the projection operators act as low pass filters where the mesh size determines the wavelength cutoff and determines how the continuum limit is approached as $\mathbf{k} \rightarrow \mathbf{0}$.

The dynamics of the $\{\bar{\mathbf{u}}_i\}$ are completely determined when all atomic degrees of freedom are specified. When they are not, as in a coupled MD–FE simulation, the dynamics must be treated approximately. The bridging scale method neglects the fine scale completely in regions without atoms and treats it statistically at the interface between the atoms and the continuum. This statistical treatment is similar to the GLE but relies on the assumption that the force is linear in the fine scale degrees of freedom. At nonzero temperature for realistic atomic systems, this assumption has not been examined. A Cauchy–Born constitutive model is used for the FE region. CGMD linearizes the interatomic force law using dynamical matrices (Sect. 4.1.2); this linearization is apparently maintained even if the nodal and atomic positions coincide. Both CGMD and the bridging scale assume the lacking fine scale degrees of freedom are distributed canonically and compute the missing energy to be $k_B T$ per missing degree of freedom, but these missing degrees of freedom do not have a direct effect on the dynamics of the continuum.

Averages (over time or ensemble averages) of the coarse and fine–scale quantities are projections of the atomic averages:

$$\langle \bar{\mathbf{u}}_\alpha \rangle = \mathbb{P}_{\alpha\beta} \langle \mathbf{u}_\beta \rangle \quad \delta \bar{\mathbf{u}}_\alpha = \bar{\mathbf{u}}_\alpha - \langle \bar{\mathbf{u}}_\alpha \rangle = \mathbb{P}_{\alpha\beta} \delta \mathbf{u}_\beta. \quad (4.74)$$

Fluctuations in atomic velocities are related to temperature, and for linear force laws, fluctuations in atomic displacements are similarly related (Sect. 4.1.2). Here, we assume isotropic response where fluctuations are characterized by

$$\langle \delta \mathbf{u}_\alpha^2 \rangle = \langle (\delta \mathbf{u}_\alpha) \cdot (\delta \mathbf{u}_\alpha) \rangle. \quad (4.75)$$

For equilibrium systems, spatial homogeneity implies that fluctuations in the atomic displacements or velocities are uniform over space and consequently independent of the particle label

$$\langle \delta \mathbf{u}_\alpha^2 \rangle = \langle \delta \mathbf{u}_\beta^2 \rangle \equiv \langle \delta \mathbf{u}^2 \rangle \quad \forall \alpha, \beta. \quad (4.76)$$

For coarse and fine-scale quantities, the global nature of the L2 projection operator \mathbf{P} leads to spatial correlations appearing in the fluctuation formulae for the coarse-scale atomic displacements. They are given by

$$\langle \delta \bar{\mathbf{u}}_\alpha^2 \rangle = \langle \mathbf{P}_{\alpha\beta} \delta \mathbf{u}_\beta \mathbf{P}_{\alpha\gamma} \delta \mathbf{u}_\gamma \rangle. \quad (4.77)$$

A similar relation for the fine-scale displacements gives

$$\langle (\delta \mathbf{u}'_\alpha)^2 \rangle = \langle \mathbf{Q}_{\alpha\beta} \delta \mathbf{u}_\beta \mathbf{Q}_{\alpha\gamma} \delta \mathbf{u}_\gamma \rangle. \quad (4.78)$$

Finally, the orthogonality of \mathbf{P} and \mathbf{Q} ensure that

$$\langle \delta \mathbf{u}_\alpha^2 \rangle = \langle \delta \bar{\mathbf{u}}_\alpha^2 \rangle + \langle (\delta \mathbf{u}'_\alpha)^2 \rangle \quad (4.79)$$

so that there are no cross correlations between the coarse and fine scales

$$\langle \delta \mathbf{u}'_\alpha \delta \bar{\mathbf{u}}_\alpha \rangle = 0. \quad (4.80)$$

Similar formulae hold for the nodal displacements, whose fluctuations are given by

$$\langle \delta \bar{\mathbf{u}}_i^2 \rangle = \langle \mathbb{P}_{i\alpha} \delta \mathbf{u}_\alpha \mathbb{P}_{i\beta} \delta \mathbf{u}_\beta \rangle, \quad (4.81)$$

and a similar formula exists for the velocity fluctuations. With the relation $\mathbb{N} \cdot \mathbb{P} = \mathbf{P}$, the atomic coarse scale and nodal fluctuations at thermal equilibrium can be compared. Spatial homogeneity at thermal equilibrium implies that the nodal fluctuations will be independent of the node label i . The atomic coarse-scale fluctuations can be written in terms of the nodal ones

$$\langle \delta \bar{\mathbf{u}}_\alpha^2 \rangle = \mathbb{N}_{\alpha i} \langle \delta \bar{\mathbf{u}}_i^2 \rangle = \left(\sum_i \mathbb{N}_{\alpha i} \right) \langle \delta \mathbf{u}_{nodal}^2 \rangle \quad (4.82)$$

where $\langle \delta \mathbf{u}_{nodal}^2 \rangle$ denotes the averaged nodal fluctuation. For typical finite-element shape functions, the sum is unity, indicating that the two fluctuations will be identical; this is no surprise since the coarse scale is merely the interpolation of the nodal quantities.

These simple fluctuation formulae have relevance to the coupling problem. First, if one associates long-time or ensemble averages with a continuum at uniform temperature, one demands that $\langle (\delta \bar{\mathbf{u}}_\alpha)^2 \rangle \rightarrow 0$ so that the coarse scale can be associated with a continuum displacement field. In this limit, the fine scale fluctuations equal the atomic fluctuations. This immediately leads to the conclusion that a coupling method can only neglect anharmonic

effects in the fine-scale degrees of freedom if they are negligible in the entire MD simulation region and not just at the MD-FE boundary. Whether or not anharmonicity is indeed negligible is strongly problem—dependent. In a coupled simulation at nonzero temperature, one only need keep track of $\langle(\delta\bar{\mathbf{u}}_\alpha)^2\rangle$ or its equivalent nodal quantity in order to have an error estimate for how well the continuum limit is approximated.

All the above manipulations of fluctuation formulae remain valid when atomic velocities are used rather than the displacement. The formulae for the velocities imply that there will be a portion of the atomic temperature measure associated with the coarse-scale degrees of freedom. Specifically, an instantaneous atomic measure of temperature T_α is given by

$$T_\alpha \equiv \frac{m_\alpha}{k_B} \delta\mathbf{v}_\alpha^2 = \frac{m_\alpha}{k_B} \left((\delta\bar{\mathbf{v}}_\alpha)^2 + (\delta\mathbf{v}'_\alpha)^2 \right). \quad (4.83)$$

At thermal equilibrium, $\langle T_\alpha \rangle = T$ by the generalized equipartition theorem (Sec. 4.1.2). Once again, if the continuum limit is associated with the vanishing of the coarse scale fluctuations, the fine-scale velocities contain the thermal vibrations of the atoms

$$T_\alpha \approx \frac{m_\alpha}{k_B} (\delta\mathbf{v}'_\alpha)^2. \quad (4.84)$$

This observation leads to a nodal measure for temperature. Although the nodal projection of fine-scale quantities is zero, the nodal projection of the second moments of the fine-scale quantities is not. Consequently, define the instantaneous nodal temperature T_i at node i as

$$T_i(t) \equiv \mathbb{P}_{i\alpha} T_\alpha. \quad (4.85)$$

A similar relationship defines the time-averaged nodal temperature $\langle T_i \rangle$ as the projection of the time-averaged fine-scale velocity fluctuations. If the interatomic force law is linear or anharmonicity is negligible, the equipartition theorem can also relate displacement fluctuations to temperature. Consequently, a similar nodal measure of the second moment of the fine-scale displacements is defined

$$(\delta\mathbf{u}'_i)^2 \equiv \mathbb{P}_{i\alpha} (\delta\mathbf{u}'_\alpha)^2. \quad (4.86)$$

If this measure varies linearly with temperature, the system can be said to be in a regime where equipartition is valid, and the constant of proportionality can be used to define an effective spring constant κ_{eff} for the interatomic interactions

$$k_B \langle T \rangle = \kappa_{eff} \langle (\delta\mathbf{u}'_i)^2 \rangle. \quad (4.87)$$

The effective spring constant need not be the equilibrium spring constant for the 0K lattice.

These fluctuation formulae are all for instantaneous averages; the time correlation functions (Eq. 4.38) of the coarse-grained atomic quantities are also relevant to the coupling problem.

The correlation functions of the atomic-scale quantities $C_{\bar{u}\bar{u}}(t)$ and $C_{u'u'}(t)$ are introduced; the cross correlation $C_{\bar{u}u'}(t)$ is 0. They nonzero correlations are subject to the constraint

$$C_{uu}(t) \langle \delta \mathbf{u}^2 \rangle = C_{\bar{u}\bar{u}}(t) \langle \delta \bar{\mathbf{u}}_\alpha^2 \rangle + C_{u'u'}(t) \langle \delta (\mathbf{u}'_\alpha)^2 \rangle, \quad (4.88)$$

which follows from Eqs. 4.38 and 4.79. At thermal equilibrium, these functions are spatially uniform, so no particle label α appears above. In practice, they would be calculated from an equilibrium MD simulation computing over many time origins and averaging over many atoms to improve the statistics. The time correlation functions are special cases of

$$C_{uu}(\mathbf{r}, t) = \frac{\langle \delta \mathbf{u}_\alpha(t) \cdot \delta \mathbf{u}_\beta \rangle}{\langle \delta \mathbf{u}_\alpha^2 \rangle}, \quad \mathbf{X}_\alpha - \mathbf{X}_\beta = \mathbf{r} \quad (4.89)$$

with similar relations for the coarse and fine-scale quantities. To examine only temporal correlations, the $C(t)$ may be appropriate, while the $C(\mathbf{r}, t)$ are required to examine spatial correlations.

If an error measure based on coarse-scale fluctuations is used in a coupled MD-FE simulation, then it is also appropriate to compare $C_{u'u'}$ with C_{uu} as an error measure. More importantly for the nonzero-temperature coupling problem, the correlation functions should be the primary means of obtaining error measures for estimated quantities like a nodal temperature T_i . If T_i is thought of as something the nodes sample from the atomic data, then the number of good samples obtained from space and time averages depends on the length and time scales of the averaging and the length and time scales determined by temperature-temperature autocorrelation function. The length and time scales determined from the correlation functions are the correlation lengths and times, which are most easily obtained by assuming an exponential decay and fitting the correlation function to $C(t) \sim e^{-t/\tau}$ or $C(R) \sim e^{-R/\lambda}$ to estimate a correlation time τ or length λ . Sampling intervals less than τ or averaging over a length smaller than λ does not yield statistically-independent data, so little is gained for a temperature estimate at scales less than these. Beyond providing an error measure for how well a quantity like temperature can be estimated from real-time data, which is the interest of this Chapter, the correlation lengths and times provide indications about how the coarse-scale quantities should behave. For times or lengths much longer than these scales, one may hope to speak of continuum dynamics, while for times much shorter, the motion is almost completely deterministic and may depend strongly on the fine-scale components. The intermediate range is most likely where nonzero-temperature MD-FE coupling methods would be needed, and these scales require some combination of continuum dynamics with some effective way to mimic the effects of the missing fine scale degrees of freedom.

4.3.1 Numerical Examples

To investigate the dynamic behavior of coarse-grained and coarse- and fine-scale kinematic quantities, MD simulations of FCC Cu ($a = 3.63 \text{ \AA}$) atoms interacting with the EAM

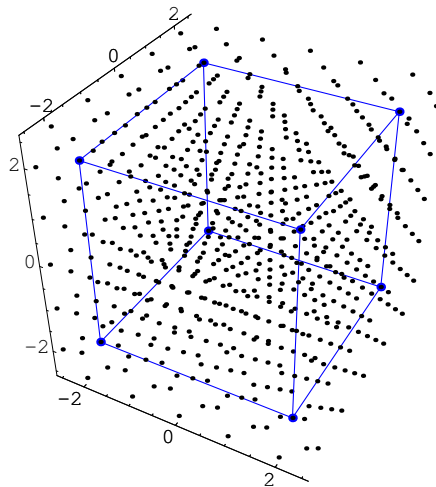


Figure 4.1: Schematic of the system used to evaluate the statistics of coarse-grained quantities. The atoms are black points while the finite-element nodes and edges are in blue. The axes are in units of the lattice constant a , and periodic, stress-free boundary conditions are applied in all three coordinate directions. The actual system dimensions were $8 \times 8 \times 8a$, $a = 3.63 \text{ \AA}$ with a varying element size l_{FE} .

potential in a cube of side length $8a$ with periodic, stress-free boundary conditions on all faces were performed. The temperature of the system is thermostatted to 300K, and the system is equilibrated and allowed to expand to a new equilibrium lattice spacing before any dynamic quantities are computed. To compute nodal quantities, a constant energy simulation, i.e. the constant-pressure boundary condition is removed, is used with the same periodic boundary conditions. The reference configuration is taken to be the 0 K lattice. A single finite element hexahedron of varying side length l_{FE} is placed inside the periodic, cubic simulation box, and the operator \mathbb{P} used to determine the nodal displacements from the atomic ones. A schematic of the system geometry is shown in Fig. 4.1.

A timestep of $t_0 \equiv 1\text{fs}$ is used for all simulations, although the atomic data is sampled only every 200 fs to compute the coarse and fine scale displacements as well as the nodal quantities. Typically, 250 sampled values, corresponding to a time of 50000 fs, are used to compute a time-averaged nodal quantity or its fluctuations. This time interval is much larger than the ratio of FE to MD timesteps is expected to be in a typical coupled simulation, but such a large sampling is required to minimize statistical errors. This difficulty of such a long time being required to obtain reasonable thermodynamic information from the MD data is a fundamental one faced by the coupling problem at nonzero temperature.

Since the reference configuration is the 0K lattice, thermal expansion appears in the time-averaged nodal displacements as a uniform strain. Thermal vibrations are fluctuations about

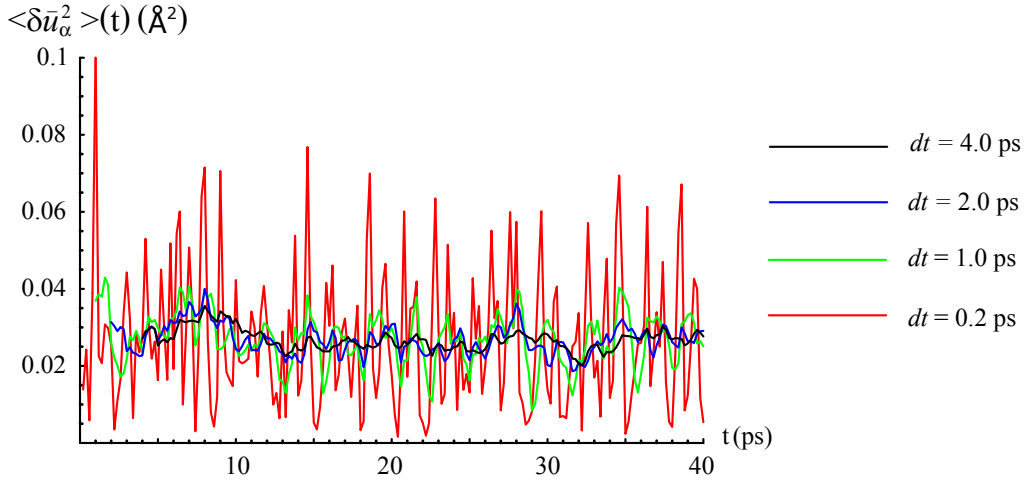


Figure 4.2: The nodal fluctuations $\delta \bar{u}_i^2(t)$ calculated as averages over the time interval dt . Although all values of dt shown here reproduce the average $\langle \delta \bar{u}_i^2 \rangle$ acceptably, computing a nodal quantity over a longer time interval produces a more smoothly varying quantity. To obtain a nodal quantity that is temporally this smooth, the averaging time is over a minimum of 1000 MD timesteps—considerably larger than the FE to MD timestep ratio that could be used in a coupled simulation.

the time-averaged, 300K equilibrium atomic or nodal positions. Running averages of the second moment of instantaneous fluctuations of the nodal displacements u_i over different time intervals is shown in Fig. 4.2, illustrating the difficulty of obtaining smoothly-varying nodal quantities at nonzero temperature. The equivalent continuum for this system is a uniform stress (due to thermal expansion), uniform temperature system. In contrast, the nodal displacements are uniform only in an average sense over large spatial regions or over long times. Consequently, the instantaneous coarse-scale velocity is nonzero although the equivalent continuum does not have a flow velocity. The nonzero second moments of the nodal velocity are proportional to a coarse-scale temperature that is nonzero unless the element size is very large. The element size l_{FE} influences the sampling properties of the CG quantities primarily through the number of sampled atoms in an element, $N_s \sim (l_{FE}/a)^3$. The second moments of the nodal displacement fluctuations plotted against N_s , which is not a monotonically increasing function of element size, are shown Fig. 4.3. As the element size increases, the number of atoms within the element remain constant for certain ranges of l_{FE} as different shells of atoms are included in the element. This fact is reflected in the graphs plotted against N_s rather than again l_{FE} . The second moment of the coarse scale velocity decreases with element size, and Fig. 4.4 shows that the fine-scale kinetic energy is the correct temperature measure for large elements. Analysis of the coarse and fine scale velocities shows that $\langle \bar{\mathbf{v}}_\alpha^2 \rangle / \langle (\mathbf{v}'_\alpha)^2 \rangle \sim l_{FE}^{-3.2}$. Since $l_{FE}^3 \sim N_s$, this indicates that

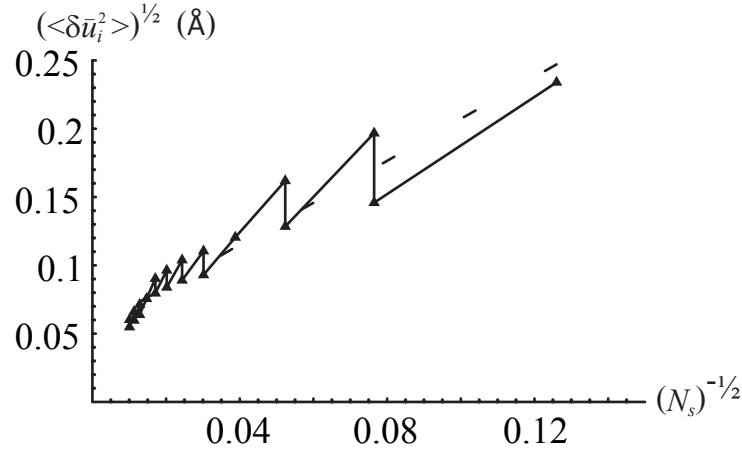


Figure 4.3: Time-averaged nodal displacement fluctuations $\sqrt{\langle \delta \bar{u}_i^2(t) \rangle}$ plotted against $1/\sqrt{N_s}$. The dotted line shows a linear least-squares fit.

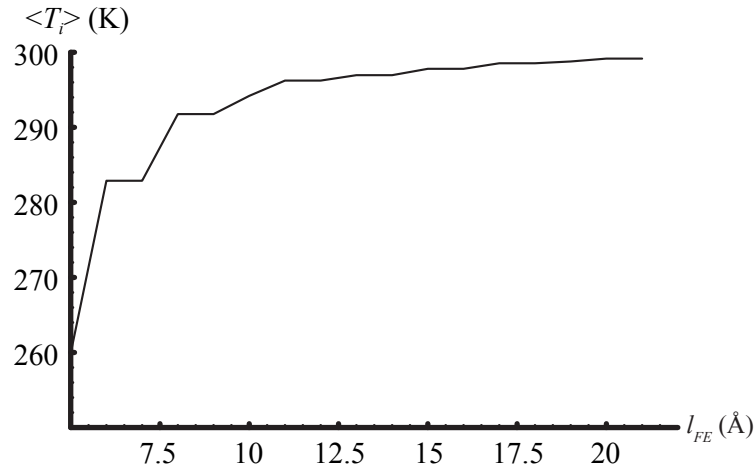


Figure 4.4: The nodal temperature $\langle T_i \rangle$ plotted against element size l_{FE} . For the largest elements, virtually all of the thermal vibrations are included in the nodal temperature which approaches the atomic temperature 300K.

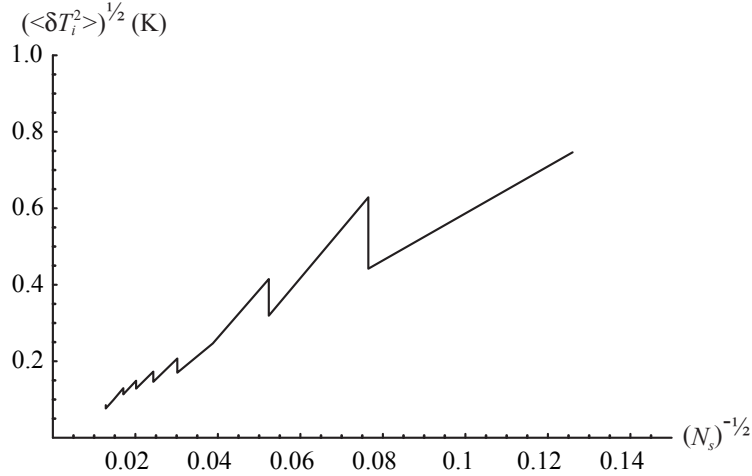


Figure 4.5: The N_s -dependence of the nodal temperature fluctuations $\sqrt{\langle \delta T_i^2 \rangle}$. The different values of l_{FE} with the same N_s also illustrate the stronger dependence on l_{FE} at small l_{FE} .

the nodal temperature varies as N_s^{-1} , as it would for independent sampling of the atoms. The suitability of T_i then is primarily an effect of the increased number of atoms sampled for node i 's temperature value. The N_s -dependence of the temperature measure is shown in Fig. 4.5. Similarly, in this system at 300K, the displacement fluctuations can characterize the temperature, too, indicating that anharmonic effects are not strong at this temperature.

Recently, the projection of the $v_\alpha^2 = \bar{v}_\alpha^2 + (v'_\alpha)^2$ to nodal positions was proposed as a temperature measure. [96] This temperature measure has two important flaws. First, there is no basis for assuming the fine-scale degrees of freedom are the only ones distributed canonically yet still associating a temperature measure computed from both the coarse and fine scale components. Second, although $v_\alpha^2 \approx (v'_\alpha)^2$ in systems with zero flow as the element size increases, there is no justification for including atomic contributions to the flow velocity in a temperature measure. Both of these flaws are incompatible with equilibrium (the canonical ensemble) and local equilibrium (the flow velocities) statistical mechanics. The correct temperature measure can depend only on the fine-scale velocities.

For a more stringent test of the formalism's ability, simulations in a long strip of FCC Cu (Fig. 4.6) are also performed. A constant amount of heat is added at one end and the same amount removed at the other, creating a constant heat flux and uniform temperature gradient along the rod after a nonequilibrium steady state has been established (see Sect. 6.6). There is a trade-off between resolving transient or spatially varying phenomena and obtaining good enough statistics for a simple constitutive model to reproduce the observed behavior. For a sampling interval of t_0 , Figures 4.7 and 4.8 show that smaller element sizes do not reproduce

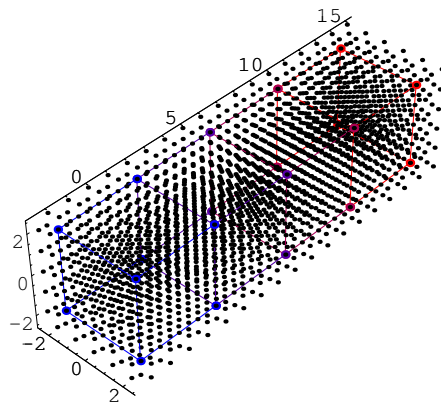


Figure 4.6: Schematic geometry for the nonequilibrium system. A uniform temperature gradient of 100 K is established between the cold end (blue) and the hot end (red). The axes are in units of $a = 3.63 \text{ \AA}$ while the actual system used was $40 \times 8 \times 8a$. The finite element connectivity is demonstrated by the colored edges. Cubes of side l_{FE} are placed along the x direction, and the number of elements in the overlaid finite–element system depends on l_{FE} since the MD system size is fixed.

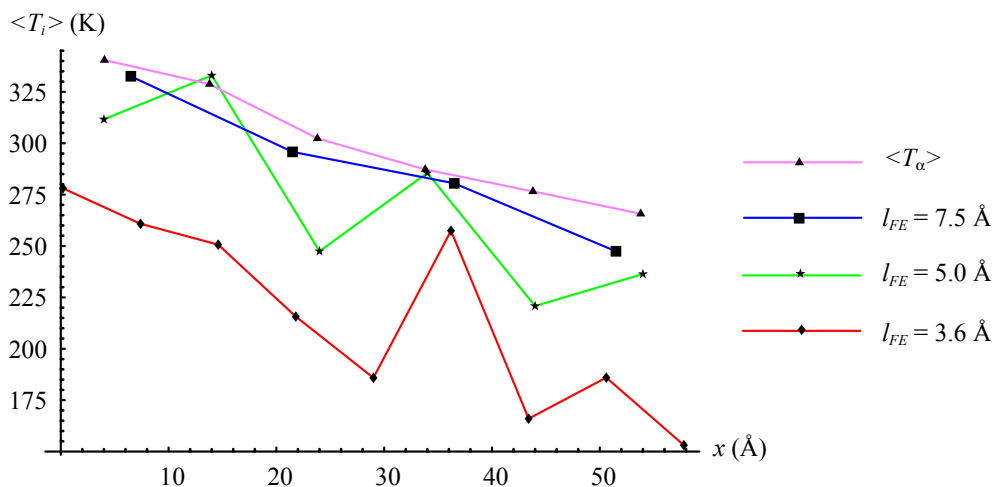


Figure 4.7: The time–averaged nodal temperature $\langle T_i \rangle$ for a smaller sampling interval. The time–averages are computed by sampling every 2 fs for a total time interval of 500 fs—two orders of magnitude smaller than those in the other plots. This small interval is clearly inadequate to resolve ∇T . For comparison, the time–averaged temperature $\langle T_\alpha \rangle$ computed from all atoms is also shown.

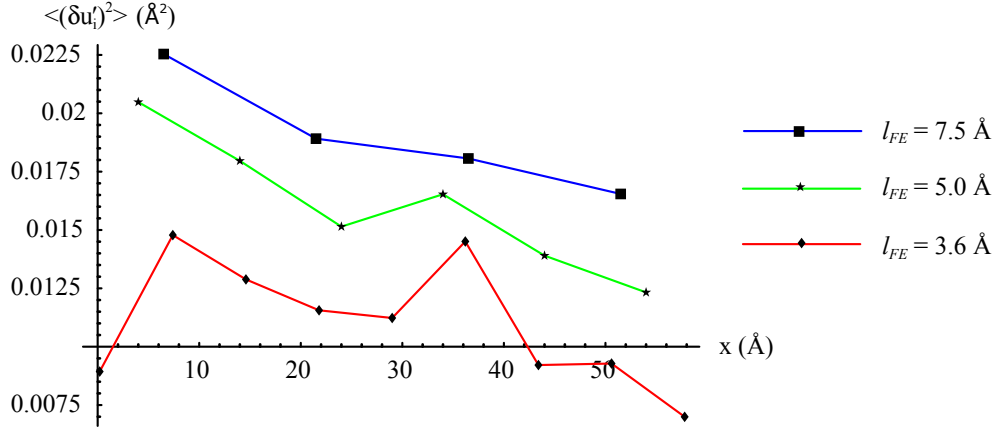


Figure 4.8: The fine scale fluctuations $\langle \delta(\mathbf{u}_i^2) \rangle$ for a smaller sampling interval.

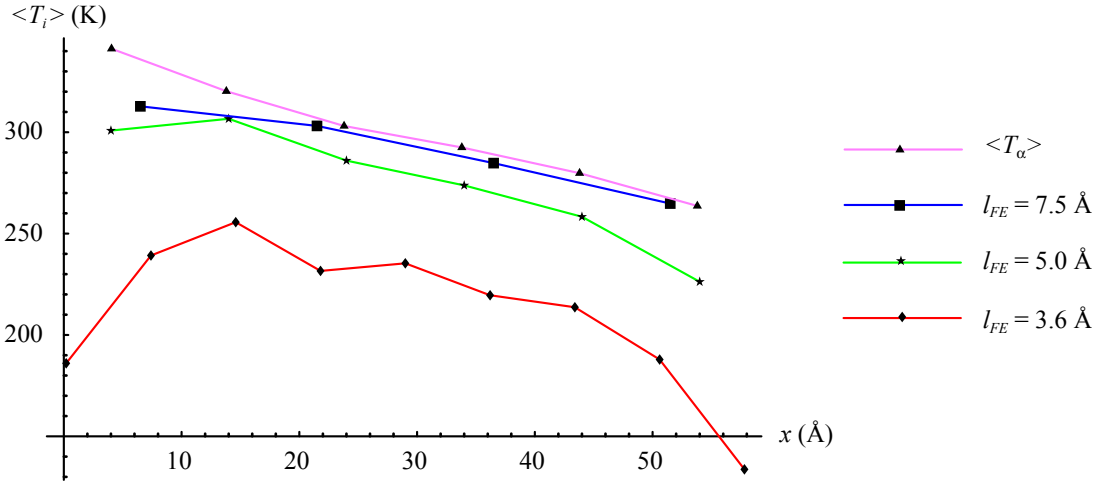


Figure 4.9: The time-averaged nodal temperature $\langle T_i \rangle$ for a larger sampling interval. Compare to Fig. 4.7. Although the smallest element sizes consistently underestimate the temperature, they do generally get ∇T correct.

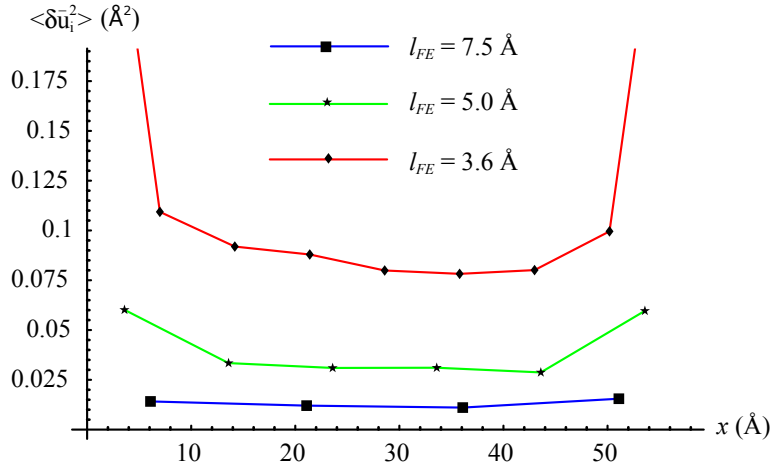


Figure 4.10: The coarse-scale fluctuations $\langle \delta \bar{u}_i^2 \rangle$ decrease with increasing l_{FE} . Except for boundary effects attributable to the constant heat flux boundary conditions, they are independent of the local temperature along the strip.

the temperature gradient. Variation of element size l_{FE} reveals the number dependence of the nodal temperature measures (Fig. 4.9). Figs. 4.10 and 4.11 show the nodal coarse and fine scale fluctuations for different element sizes along the length of the rod. The $\langle \delta \bar{u}_i^2 \rangle$ at the smallest values of l_{FE} are accompanied by more thermal, vibrational energy appearing in the coarse scale. For these smaller element sizes, the excess temperature in the coarse scale is accompanied by the consistent underestimation of the nodal temperatures T_i , as shown in Figs. 4.9 and 4.11.

Time-averaging is seen to be a crucial ingredient to produce correspondence between atomistic and continuum system for these model systems. The time interval required to produce acceptable error measures, determined here by the averages of the fluctuations of the nodal quantities, depends on the element size l_{FE} . The dependence of the time interval on l_{FE} is a reflection that the error measures depend on the number of statistically independent samples of the nodal displacements or temperatures. This number of samples is roughly

$$N_s \sim \frac{l_{FE}}{\lambda_c} \frac{\Delta T_s}{\tau_c}, \quad (4.90)$$

where the material and problem dependence enters through the correlation length λ_c and correlation time τ_c (Sect. 4.3). The dependence of the nodal fluctuations on the number of atoms contributing to the value of the nodal quantity reveals that the above arguments based on statistical independence are correct for this material and this range of temperatures.

For the coupling problem, there are three regions of interest: the one in which the continuum

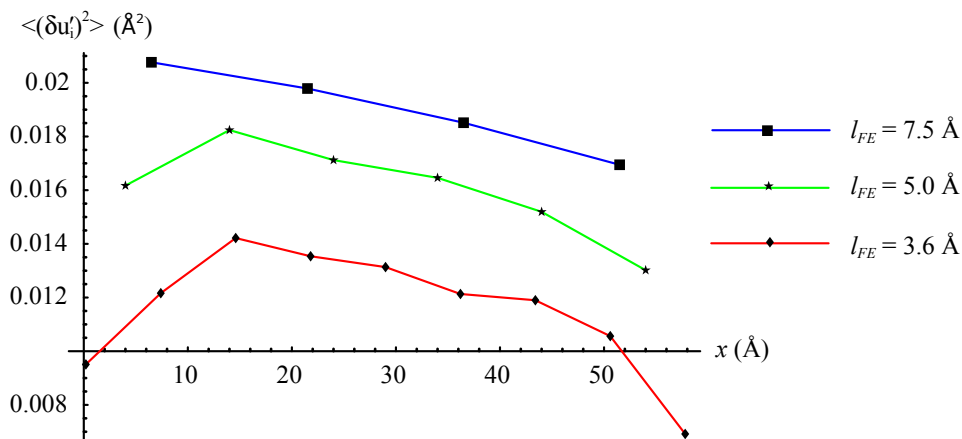


Figure 4.11: Nodal projection of the fine scale fluctuations for different element sizes reveals that they may be used as a temperature measure in this steady-state simulation. This is essentially a computation of a coarse-grained Debye–Waller factor for the system as a function of the local temperature along the length of the system.

element size and/or timestep is much larger than the correlation time and/or length, the one in which these quantities are comparable, and the one in which the element size and timestep are much smaller, i.e. they are on the order of the lattice spacing and molecular dynamics timestep. In the first regime, the continuum limit can be said to have been obtained, although the fluctuations in the continuum quantities may not be representable at the continuum level. In the third regime, the nodes act just like atoms, although in some sort of weakly-averaged sense. The middle regime is the least clear of the two, for it is intermediate between deterministic and stochastic behavior.

4.4 Conclusions

A typical multiscale problem is archetypically mesoscale; it removes degrees of freedom from the atomic-scale so that some statistical treatment is necessary to correctly describe the dynamical evolution of the coarse-grained variables at nonzero temperature. Unfortunately, the degree of coarse-graining and the system sizes simulated are not macroscopic so that the $O(1/N)$ correctness in the thermodynamic limit leading to smooth hydrodynamics is not directly applicable, even to coupled systems in thermal equilibrium.

The state of the art in nonequilibrium statistical mechanics is not adequate for describing the

evolution of the coarse-grained variables, but the Mori-Zwanzig formalism provides at least a basis for treating the removed degrees of freedom. From a simpler approach, elementary statements based on fluctuation formulae and correlation functions have strong implications on how the coarse-grained variables should behave depending on the relative length and time scales of the FE and MD simulations.

Finally, it is worthwhile to point out that MD simulations have been successful in simulating both equilibrium and nonequilibrium systems through methods that started out as ad-hoc methods and only later began to have a formal justification for their correctness. Coupling algorithms are in a similar state now, so the lack of justification or even correctness for a method at nonzero temperature does not have to be viewed as an impediment. Meaningful results can be obtained by ad-hoc methods provided that their correspondence with thermal equilibrium systems in the appropriate long time and large length scale limits is validated.

Chapter 5

Models of Heat Transfer

Principle Author: R.E. Jones

5.1 The Physics of Heat Transfer

In classical mechanics, heat is a primitive concept that lacks a basic definition and is expected to be understood at an axiomatic level. Physically speaking, see *e.g.* [97, 98], heat is thermal energy or kinetic energy that does not have a net momentum. Another interpretation is that heat energy is the energy in excess of the internal energy at equilibrium. There are a variety of particles that can be heat carriers, *e.g.* in metals electrons are significant carriers. Since atomistic models explicitly represent the atom as a single particle, the only heat carriers of interest are “phonons” or lattice vibrations. Kinetic theory implies that thermal conductivity k is proportional to $cv_g\ell$, where c is heat capacity, v_g is the group (or mean) phonon velocity and ℓ is the mean free path. Based on the mean free path, phonons transport thermal energy in two basic modes : ballistic, where the mean free path of a phonon is relatively large compared to the size of the object, and diffusive, where it is relatively short. The phonon mean free path ℓ can be estimated using perturbation theory as

$$\ell(\omega, \theta) = \frac{\mu a^3 v_g \omega_{Debye}}{2k_B \gamma^2 \theta \omega^2},$$

where ℓ is a function of phonon frequency ω , temperature θ , lattice constant a , shear modulus μ , the Debye frequency ω_{Debye} (mean) Gruneisen parameter γ and Boltzmann’s constant k_B .¹ In general, ℓ decreases with increasing temperature and/or phonon frequency.

In ballistic transport, the mean free path ℓ is large relative to the lattice spacing and consequently collisions between phonons occur infrequently. In the purely ballistic extreme,

¹This formula is in Int. J. Thermophys. 2(1) 55 but cites P.G. Klemens Thermal Conductivity, Vol 1, Academic Press 1969 pp 1-68.

the dominant wavelength in the phonon distribution is so long that the mean free path, which is temperature dependent in general, is limited only by the size of the crystal, therefore independent of temperature. These conditions occur below the Debye temperature, $\theta_{Debye} = \frac{\hbar}{k_B} \omega_{Debye} = \frac{\hbar}{k_B} v_g (6\pi^2 \eta)^{\frac{1}{3}}$,² which is related to the size of the lattice spacing through the parameter $\eta^{\frac{1}{3}} = (\frac{N}{V})^{\frac{1}{3}} \approx a$. Here \hbar is Planck's constant and N and V represent the particle count and volume of the system, respectively. In this case, phonon velocity is essentially constant, so heat conductivity, like heat capacity, is proportional to the cube of the temperature. At this extreme, also known as the Casimir limit, the heat flux \mathbf{q} is related to the temperature difference $\Delta\theta$ at the boundaries of a slab, $\|\mathbf{q}\| \propto \Delta\theta^4$, and is independent of the thickness of the slab. So, unlike a macroscopic rod or slab with a mean temperature below ω_{Debye} , *e.g.* room temperature, and a temperature difference between the ends, no temperature gradient can be established. Instead, jumps in temperature occur at the boundaries of a body experiencing ballistic heat transport. A harmonic model of a solid, *i.e.* particles connected by linear springs arising from an internal energy quadratic in the (nearest neighbor) inter-particle distances, exhibits this behavior since it lacks coupling between modes. This lack of coupling implies that there is no mechanism to model collisions and all heat transfer must be ballistic in nature. It should be noted that the harmonic solid is also a degenerate case in that it lacks a mechanism to attain equilibrium, and consequently is only valid for near-equilibrium states.

On the other hand, at high temperatures on the order of the Debye temperature, or greater, or at high frequency and large wave vectors, scattering due to geometric defects and collisions dominates heat transfer. It is this scattering process that gives rise to the classical diffusive behavior. For crystalline solids, (Umklapp) scattering dominates and determines the behavior observed in macroscopic solids. Under these conditions, the phonon mean free path ℓ is inversely proportional to temperature to a power greater than unity and the heat capacity c_v (at constant volume) is given by the Dulong-Petit constant $3\rho k_B$, where ρ is a number density of phonons. Consequently, thermal conductivity k decreases with increasing temperature. Umklapp scattering at the heart of this phenomenon is a third order process, *i.e.* involving three interacting phonons, where the wave vectors of the incoming phonons are related to that of the outgoing phonon by a reciprocal lattice vector \mathbf{G} ,

$$\mathbf{k}_1 + \mathbf{k}_2 = \mathbf{k}_3 + \mathbf{G} .$$

This process conserves energy but changes the phonon “momentum”, which moves the system closer to equilibrium. Note that phonon momentum is *not* the physical momentum associated with mass transport.

²For silicon $\theta_{Debye} = 625K$.

5.2 Models of Heat Transfer

Various models of heat transfer make different basic assumptions, *e.g.* kinetic theory assumes local thermodynamic equilibrium in space and time. These models can be roughly categorized by their applicability to a system of a particular size and duration relative to the intrinsic length-scale ℓ and timescale τ , respectively (see [98]). Note that the time and length-scales related to energy and momentum may be different.

5.2.1 The Boltzmann Transport Equation

The Boltzmann Transport Equation (BTE) is a general transport theorem applicable to non-equilibrium processes. Its derivation is quite simple and is based on the description of an ensemble of particles by a statistical distribution $f = f(\mathbf{x}, \mathbf{p}, t)$, where the variables \mathbf{x} , \mathbf{p} are particle position and momentum, respectively, and time t . The total time rate of change in the distribution is given by

$$\frac{d}{dt}f = \partial_t f + \partial_{\mathbf{x}}f \cdot \dot{\mathbf{x}} + \partial_{\mathbf{p}}f \cdot \dot{\mathbf{p}} = \partial_t f + \partial_{\mathbf{x}}f \cdot \frac{1}{m}\mathbf{p} + \partial_{\mathbf{p}}f \cdot \mathbf{F} , \quad (5.1)$$

after using Hamilton's equations, namely $\dot{\mathbf{x}} = \frac{1}{m}\mathbf{p} = \mathbf{v}$ and $\dot{\mathbf{p}} = \mathbf{F}$. As with all transport equations the time rate of change of a quantity is equal to the amount being generated, in this case

$$\frac{d}{dt}f = s_{scatter} \approx \frac{1}{\tau(\mathbf{x}, \mathbf{p})}(f_e - f) . \quad (5.2)$$

The source term on the right-hand side of (5.2)₁ is the mechanism which restores equilibrium. Without this dissipative term, f would remain unchanged along flow as required by the Liouville theorem. Physically, this would represent phonons propagating energy through the lattice undisturbed, as in purely ballistic transport. The relaxation time approximation (5.2)₂ is a linearization that assumes f will approach f_e , the equilibrium distribution, in a characteristic time τ , which is dependent on position and momentum. Roughly speaking, the relaxation time approximation leads to a linear differential equation $\dot{f} = \frac{1}{\tau}(f_e - f)$ which has the exponentially decaying solution $f - f_e \propto \exp(-\frac{t}{\tau})$.

For an isolated system $\mathbf{F} = \mathbf{0}$ and the BTE is simply

$$\partial_t f + \partial_{\mathbf{x}}f \cdot \mathbf{v} \approx \frac{1}{\tau(\mathbf{x}, \mathbf{p})}(f_e - f) \quad (5.3)$$

Furthermore, under quasi-equilibrium conditions, where (a) the system is steady $\partial_t f \approx 0$, *i.e.* $t \gg \tau$, and (b) large $L \gg \ell$ relative to $|f - f_e|$ so that $\partial_{\mathbf{x}}f \approx \partial_{\mathbf{x}}f_e$, it is also possible to solve the approximate BTE (5.3) with

$$f = f_e - \tau \partial_{\mathbf{x}}f_e \cdot \mathbf{v} \quad (5.4)$$

At equilibrium, the distribution $f = f_e$ is a function of temperature θ so that

$$\partial_{\mathbf{x}} f_e = \frac{d}{d\theta}(f_e) \partial_{\mathbf{x}} \theta .$$

Consequently, the heat flux defined as the transport of particle energy ϵ , *i.e.*

$$\mathbf{q} = \int \mathbf{v} f \epsilon d^3 \mathbf{p} = \int \mathbf{v} f \epsilon \rho_{\epsilon}(\epsilon) d\epsilon , \quad (5.5)$$

where $\rho_{\epsilon}(\epsilon)$ is the density of energy states, reduces to

$$\mathbf{q} = - \int \tau \mathbf{v} (\mathbf{v} \cdot \partial_{\mathbf{x}} \theta) \frac{d}{d\theta}(f_e) \epsilon \rho_{\epsilon}(\epsilon) d\epsilon = - \int \tau \mathbf{v} (\mathbf{v} \cdot \partial_{\mathbf{x}} \theta) \epsilon \rho_{\epsilon}(\epsilon) d\epsilon \frac{d}{d\theta}(f_e) . \quad (5.6)$$

Note that first term in (5.4) drops out when integrated over momentum space due to a conservation principle. The definition of the material property heat conductivity as

$$\mathbf{k} = \int \tau \mathbf{v} \otimes \mathbf{v} \frac{d}{d\theta} f_e \epsilon \rho_{\epsilon}(\epsilon) d\epsilon$$

assumes that (5.6) is in the form of Fourier's law *i.e.* that magnitude of the heat flux \mathbf{q} is proportional to the temperature gradient $\partial_{\mathbf{x}} \theta$ and in opposite direction. In the large system limit, \mathbf{k} is generally taken to be isotropic $\mathbf{k} = k \mathbf{l}$ where $k = \int \tau v_g^2 \frac{d}{d\theta} f_e \epsilon \rho_{\epsilon}(\epsilon) d\epsilon$.

Majumdar's "Equation of Phonon Radiative Transport" (EPRT) [99] is a reduction of the BTE based on phonon intensity per solid angle in direction of phonon propagation and frequency interval around ω

$$I_{\omega} = \sum_p \mathbf{v}_p f \hbar \omega_p \rho_{\omega} , \quad (5.7)$$

where ρ_{ω} is density of states in ω -space and p refers to the polarization of the phonons. The BTE for an isolated system can be manipulated to the EPRT, *i.e.*

$$\frac{1}{\|\mathbf{v}\|} \partial_t I_{\omega} + \mu \partial_t I_{\omega} = \frac{1}{\|\mathbf{v}\| \tau} (I_e - I_{\omega}) ,$$

where $I_e = \frac{1}{2} \int_{-1}^1 I_{\omega} d\mu$ and μ is the cosine of the angle around the propagation direction. This integro-differential form of the BTE achieves diffusive and ballistic limiting cases while reducing the complexity of the solution space.

G. Chen developed another reduction of the BTE [100] to overcome its apparent intractability. The Ballistic-Diffusive Heat Conduction Equation (BDHCE) is based on an additive decomposition of the phonon distribution as $f = f_b + f_m$, where f_b is the distribution of the ballistic component and f_m is the distribution of the remainder associated with diffusive

transport. Using Majumdar’s intensity variable (5.7), Chen finds a particular solution to a ballistic transport equation very similar to the EPRT

$$\frac{1}{\|\mathbf{v}\|} \partial_t I_{b\omega} + \mathbf{d} \partial_t I_{b\omega} = -\frac{1}{\|\mathbf{v}\| \tau} (I_{b\omega})$$

where \mathbf{d} is the direction of phonon propagation. The particular solution is based on the idea that the ballistic phonons emanate from the boundary of the body and therefore have a well-defined propagation direction. The diffusive transport is treated as an isotropic process and through manipulation is shown to be equivalent to

$$\tau \partial_t^2 u_m + \partial_t u_m = \partial_{\mathbf{x}} \left(\frac{k}{c} \partial_{\mathbf{x}} u_m \right) - \partial_{\mathbf{x}} \cdot \mathbf{q}_b$$

where the internal energy associated with the diffusive transport u_m is a function of temperature and the heat flux due to the ballistic transport \mathbf{q}_b is a function of I_b . This relationship, without the \mathbf{q}_b term, is essentially the Hyperbolic Heat Equation that will be discussed in the following section.

5.2.2 The Maxwell-Cattaneo Equation

For the case where time duration is on the order of the timescale $T \approx \tau$, but the system length is much greater than the characteristic length-scale $L \gg \ell$, the BTE can be simplified to the well-known Maxwell-Cattaneo equation (MCE). Multiplying (5.3) by $\mathbf{v} \epsilon \rho_\epsilon d\epsilon$, and integrating over the energy results in

$$\partial_t \mathbf{q} + \int \partial_{\mathbf{x}} f \cdot \mathbf{v} \mathbf{v} \epsilon \rho_\epsilon(\epsilon) d\epsilon = - \int \frac{1}{\tau} f \mathbf{v} \epsilon \rho_\epsilon(\epsilon) d\epsilon . \tag{5.8}$$

Now assume (a) relaxation time is constant for all positions, momenta and energies, (b) quasi-equilibrium conditions, to reduce (5.8)

$$\partial_t \mathbf{q} + \frac{1}{\tau} \mathbf{q} = -\frac{1}{\tau} k \partial_{\mathbf{x}} \theta \tag{5.9}$$

The Maxwell-Cattaneo equation (5.9) together with the balance of energy for a rigid conductor, $c_v \frac{\partial}{\partial t} \theta = -\partial_{\mathbf{x}} \mathbf{q}$, leads to the so-called “hyperbolic heat equation”

$$c_v \tau \partial_t^2 \theta + c_v \partial_t \theta = k \partial_{\mathbf{x}}^2 \cdot \theta , \tag{5.10}$$

which has attenuating wave-like solutions with the possibility of thermal shocks. The speed of propagation of these waves is typically slower than that of sound so that thermal waves are sometimes called “second sound”.

Gurtin and Pipkin [101] developed a similar model to the MCE based on an analogy to viscoelasticity, where a functional is used to model “fading memory”. Interestingly, in this theory the heat flux is directly related to the free energy.

5.2.3 Fourier's Law

Given the same restrictions to the BTE that resulted in the MCE, and now with the constraint that the relaxation time τ is very small compared to the time duration of the system (or the heat flux is essentially steady), the system will follow the classical Fourier's law

$$\mathbf{q} = -k \partial_{\mathbf{x}} \theta . \quad (5.11)$$

Using, again, the balance of energy for a rigid conductor, (5.11) reduces to

$$c_v \partial_t \theta = k \partial_{\mathbf{x}}^2 \theta . \quad (5.12)$$

Since (5.12) is parabolic in character many authors interpret Fourier's Law (FL) as having an infinite speed of propagation, which is rational given the limiting process at which it was obtained from the MCE. It also follows that the Fourier solution is the steady-state limit of the MCE.

5.3 Conclusions

With regard to coupling continuum to atomistic representations of a solid, it seems that the BTE and its approximations (*e.g.* EPRT and BDHCE) are too complex to be employed efficiently in the continuum side. In the sense that they statistically represent distributions of phonons, they are not “natural” to the concept of a classical continuum, whereas the MCE and FL are commonly employed for modeling heat transfer in continua. This limits the coupling scheme to (a) problems that would experience primarily diffusive heat transport *i.e.* application at or above the Debye temperature, (b) large system sizes and (c) near equilibrium, which are requirements for reducing the BTE to the MCE and FL.

The idea that phonons are lattice motions that have no net momentum, *i.e.* they are vibrations, is key to defining how a continuum will interpret the atomistic region's kinematics. This idea is embedded, at least in a local sense, in Hardy's decomposition of velocities

$$\mathbf{v}^\alpha = \mathbf{u}^\alpha + \bar{\mathbf{v}} ,$$

where \mathbf{v}^α is the velocity of an atom α , $\bar{\mathbf{v}}$ is the average velocity in the neighborhood defined by the radius of the localization function and \mathbf{u}^α is the velocity attributed to thermal motion. Other schemes, say based on RKPM or wavelet filtering or simply projection on to FE spaces, could be devised to separate the vibrations from the bulk motion but Hardy's idea seems to have the same basic qualities, easily implemented and therefore a good initial scheme. Localization functions leading to weighted averages will be needed in both space and time to “scale-up” the discrete atomistic quantities $\{\mathbf{x}^\alpha, \mathbf{v}^\alpha\}$ to continuum fields, *e.g.* θ , especially

if ensemble averages are needed in the process. The sizes of these localization functions relative to the intrinsic length and time scales, ℓ and τ , will need to be investigated, keeping in mind the computational limits imposed by the numerical discretization of the continuum, *e.g.* mesh size and stable time-step.

Some model problems that a coupling scheme would need to produce reasonable solutions are:

- An atomistic region overlapped with a continuum rigid heat conductor. The motions in the atomistic region would have to be controlled by the boundary conditions so that there is no net motion to be consistent with the rigidity constraint in the continuum. Heat should be able to be propagated in both directions in a manner that is indistinguishable from a completely atomistic region, at least at steady state.
- An atomistic region overlapped with a continuum deformable heat conductor. Here, the phonons would need to be in the diffusive range of wave vectors and temperatures. And, for convenience, the net motions should be small *i.e.* interpreted as infinitesimal by the continuum and therefore within the range of applicability of a linear model.

To determine if either of the continuum models, *e.g.* the MCE or FL, is applicable, it will be necessary to calculate the mean free path ℓ and a characteristic relaxation time τ for the generated phonons. A workable atomistic definition of either temperature or heat flux derived from statistical mechanics would be a prelude to “up-scaling” the atomistic information in a coupling scheme. A means of controlling the boundary temperature, *i.e.* a thermostat, or heat flux on the atomistic side will be the key ingredient in “down-scaling” the continuum information. Unfortunately, some of the obvious measures of consistency, *e.g.* energy conservation for the whole system, will not be applicable on the continuum side.

This page intentionally left blank.

Chapter 6

Evaluation of Temperature and Heat in Atomistic Simulation

Principle Authors: E.B. Webb III and J.A. Zimmerman

Expressions for temperature T and heat flux \mathbf{q} in atomistic systems derived from a continuum formalism developed by R.J. Hardy are compared with analogous expressions originating from statistical mechanics. While the former employ a consistent scheme of distributing these quantities throughout the system volume, the latter are only strictly defined at explicit atomic positions. We compare the volume and time averaging of T and \mathbf{q} for both methods of calculation and find that time averaging is required, regardless of calculation method and analysis volume, in order to realize reasonable convergence on continuum quantities. This result arises from the inherent dependence of these quantities on collective atomic motion rather than instantaneous structure and is similar to what was found for an evaluation of stress at finite temperature (discussed in Chapter 3). Furthermore, for a given analysis volume, the Hardy descriptions for T and \mathbf{q} converge as or more quickly than the corresponding explicit atomic expressions. We propose that the Hardy technique is more robust because, in a physically sound manner, it removes the discrete nature of atomic motion and interactions and effectively distributes them throughout the system volume. This provides a consistent manner of accounting for interactions that span the boundary of a sub-system analysis volume while also minimizing the influence of fluctuations about the local average.

6.1 Introduction

Atomistic simulation provides insight into material science phenomena at fundamental length and time scales. In contrast, physical experimentation typically quantifies material properties at the macroscopic level. A desire for direct relations between atomic phenomena, resultant

microstructure, and derived macroscopic properties motivates efforts to bridge length and time scales between the atomistic and the continuum. One benefit of this is a more accurate understanding of thermo-mechanical deformation processes including failure. To achieve coupling across length and time scales, it is essential that proper definitions for continuum variables such as stress, temperature and heat flux exist that can be evaluated within an atomistic framework.

Connections between continuum variables and microscopic quantities originate from long-wavelength elasticity theory or long-time, equilibrium ensemble averages giving rise to macroscopic balance equations. However, the instantaneous atomic contributions to these averages do not have the same physical interpretation as the corresponding point-wise continuum quantities. Although there have been many past efforts to develop definitions for stress and other variables in a manner consistent with the continuum mechanical balance laws for linear momentum and energy, one of the most notable has been by R.J. Hardy and co-workers [52, 53, 55]. Their formalism produces expressions for stress and heat flux that are defined from atomistic variables but satisfy the continuum mechanical balance laws. In a recent publication [102], Hardy and colleagues presented an expression for temperature developed by consideration of the equipartition theorem and the kinetic energy associated with atomic velocities relative to the velocity of the continuum at a spatial point. It is not rigorously defined within the context of the same balance laws as was done for stress and heat flux.

In this work, expressions for temperature and heat flux in atomistic systems derived by Hardy are compared with the expressions commonly used in atomistic simulation. An extension of Hardy's technique is presented that includes time averaging for finite temperature systems. We have performed molecular dynamics (MD) simulations to characterize the consistency of these expressions with continuum models of heat transport. We have also performed spatial and time averaging simulation studies to determine the limits at which fluctuations do not overwhelm the expectation values of continuum properties.

6.2 Hardy's Formalism Revisited

Hardy's formalism was presented in section 3.2. As stated in that section, Hardy's method enables him to derive expressions for the continuum variables of mechanical stress and heat flux by defining continuum fields for mass density (ρ), linear momentum density (\mathbf{p}) and internal energy density (e) that are based on atomic properties and using them within the spatial forms of the balance of mass, linear momentum and energy for a dynamic continuum [13]. For example, the balance of energy is

$$\frac{\partial e}{\partial t} = \partial_{\mathbf{x}} \cdot (\boldsymbol{\sigma} \cdot \mathbf{v} - e\mathbf{v} - \mathbf{q}). \quad (6.1)$$

where $\boldsymbol{\sigma}$ is the Cauchy stress tensor, \mathbf{v} is the material point velocity and \mathbf{q} is the heat flux vector. Using the density functions shown above within the balance equations, Hardy developed the following expressions for stress and heat flux at a spatial point,

$$\boldsymbol{\sigma}(\mathbf{x}, t) = - \left\{ \frac{1}{2} \sum_{\alpha=1}^N \sum_{\beta \neq \alpha}^N \mathbf{x}^{\alpha\beta} \otimes \mathbf{F}^{\alpha\beta} B^{\alpha\beta}(\mathbf{x}) + \sum_{\alpha=1}^N m^\alpha \mathbf{u}^\alpha \otimes \mathbf{u}^\alpha \psi(\mathbf{x}^\alpha - \mathbf{x}) \right\} \quad (6.2)$$

$$\mathbf{q}(\mathbf{x}, t) = - \sum_{\alpha=1}^N \left[\sum_{\beta \neq \alpha}^N \frac{\partial \phi^\beta}{\partial x^{\alpha\beta}} \frac{\mathbf{x}^{\alpha\beta} \otimes \mathbf{x}^{\alpha\beta}}{x^{\alpha\beta}} B^{\alpha\beta}(\mathbf{x}) \right] \cdot \mathbf{u}^\alpha + \sum_{\alpha=1}^N \left\{ \frac{1}{2} m^\alpha (u^\alpha)^2 + \phi^\alpha \right\} \mathbf{u}^\alpha \psi(\mathbf{x}^\alpha - \mathbf{x}). \quad (6.3)$$

In this relation, $\mathbf{F}^{\alpha\beta}$ is the interatomic force exerted on atom α by atom β , $B^{\alpha\beta}(\mathbf{x})$ is the bond function defined by the expression $B^{\alpha\beta}(\mathbf{x}) = \int_0^1 \psi(\lambda \mathbf{x}^{\alpha\beta} + \mathbf{x}^\beta - \mathbf{x}) d\lambda$, and $\mathbf{u}^\alpha \equiv \mathbf{v}^\alpha - \mathbf{v}$ where $\mathbf{v} \equiv \mathbf{p}/\rho$. Recall that the quantities $B^{\alpha\beta}$ and ψ are defined such that they are non-zero only within a limited-sized volume centered at the spatial point \mathbf{x} , and that both have units of inverse volume. When ψ is defined as a constant for the entire volume of the atomic system, equation (6.2) exactly reproduces the virial theorem, while equation (6.3) yields an analogous expression that has been used for heat flux,

$$\mathbf{q}(t) = \frac{1}{V} \left\{ \frac{1}{2} \sum_{\alpha=1}^N \left[\sum_{\beta \neq \alpha}^N \mathbf{F}^{\alpha\beta} \otimes \mathbf{x}^{\alpha\beta} \right] \cdot \mathbf{u}^\alpha + \sum_{\alpha=1}^N \left\{ \frac{1}{2} m^\alpha (u^\alpha)^2 + \phi^\alpha \right\} \mathbf{u}^\alpha \right\}. \quad (6.4)$$

where V denotes the total volume of the atomic system. Note that, while equation (6.3) is formulated with the notion of evaluating a sub-system volume region within an atomistic ensemble, equation (6.4) is properly used to analyze the entire system. However, equation (6.4) is often used to define heat flux within a sub-system volume. We will address implications of evaluating the atomic heat flux expression in this manner later in this chapter.

Hardy and colleagues recently presented [102] an expression for temperature within this same continuum mechanical framework that was derived by relating continuum temperature to the kinetic energy density associated with the relative atomic velocities \mathbf{u}^α . Their expression is given by

$$\mathbb{T}(\mathbf{x}, t) = \frac{1}{3k_B} \frac{\sum_{\alpha=1}^N m^\alpha (u^\alpha)^2 \psi(\mathbf{x}^\alpha - \mathbf{x})}{\sum_{\alpha=1}^N \psi(\mathbf{x}^\alpha - \mathbf{x})}. \quad (6.5)$$

Again, an analogous expression for temperature utilized in atomistic simulations can be identified as

$$\mathbb{T}(t) = \frac{1}{3Nk_B} \sum_{\alpha=1}^N m^\alpha (u^\alpha)^2. \quad (6.6)$$

This expression is also often modified to calculate temperature within a sub-system volume.

6.3 Equilibrium Temperature Simulations

An analysis of spatial and temporal averaging of temperature (T) as determined from the standard atomic expression, equation (6.6), was performed. This permitted us to establish minimum limits necessary to converge sub-system averages onto full system expectation values within an acceptable degree of error ($\sim 1\%$). This analysis was performed for an NVT ensemble where the volume used was determined by a separate NPT simulation such that, in the subsequent NVT simulation, the expectation value for pressure was less than 100 bar. A similarly equilibrated simulation cell was also run in an NVE ensemble for comparison purposes. Temperature in the NVE ensemble was 298 K (as compared to 300 K in the NVT ensemble). Note that this analysis is performed for systems in which an expectation value for T is clearly defined, *i.e.* the system is in thermal equilibrium. This would not be the case, for example, if temperature gradients existed through the simulation cell. Nonetheless, it is useful to quantify minimum analysis time and length scales for a given set of materials as represented by a given set of interatomic potential energy functions. For the simulations discussed in this and the following sections, we used the embedded atom method potential for Cu by Foiles, Baskes and Daw [32]. The system analyzed was composed of 4,000 atoms ($10 \times 10 \times 10$ unit cells). Temperature control was accomplished by exerting an atomic drag force proportional to both the difference between the current temperature and the desired temperature for the system and the atom's velocity [56].

Figure 6.1 shows average values of T as a function of analysis volume for a randomly chosen point in the simulation cell; additionally, data are shown for different averaging times. Similar

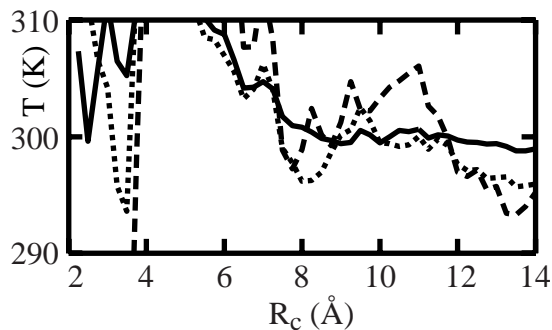


Figure 6.1: Average atomic temperature for an NVT ensemble as a function of analysis volume radius. Curves are shown for averaging times of 0.1 ps (dashed), 1 ps (dotted) and 5 ps (solid).

to what was found for stress, it is seen that a tradeoff exists between space and time averaging. For small analysis volumes, a significant degree of time averaging must be employed; in fact, for the longest time average shown, 5 ps, a reliable prediction of T is not obtained for $R_c \leq 8 \text{ \AA}$. For analysis volumes $R_c \geq 10 \text{ \AA}$, reasonable convergence is obtained within

a simulation duration of order 1 ps; however, our requirement of $\sim 1\%$ deviation is only achieved for the 5 ps time average data. Results for the corresponding analysis of stress in Chapter 3 demonstrated a somewhat less stringent requirement on time averaging. For instance, $1000 \delta t$ (2 ps) was sufficient to give a very reliable prediction of stress even for R_c as small as 4 Å. This difference is small, however, so, within the error of our calculations, we conclude that evaluating temperature in a sub-system analysis volume with good accuracy requires similar statistics to evaluating stress at finite temperature. For the system presented this is achieved for $R_c = 10$ Å with time averaging over a few ps. Similar results were obtained from the NVE simulation. This is not surprising given that the temperature control algorithm in the NVT ensemble has little effect on system dynamics since the system was pre-equilibrated to the set point temperature $T = 300$ K.

Given the knowledge obtained thus far, we focus on comparing the Hardy and atomistic expressions for T by using a single analysis volume ($R_c = 10$ Å) and perform similar time averaging within the analysis sub-volume. Figure 6.2 shows that the Hardy expression for temperature as given by equation (6.5), behaves quite similarly to the atomic expression in equation (6.6). Thus, the Hardy expression gives reliable predictions of local temperature

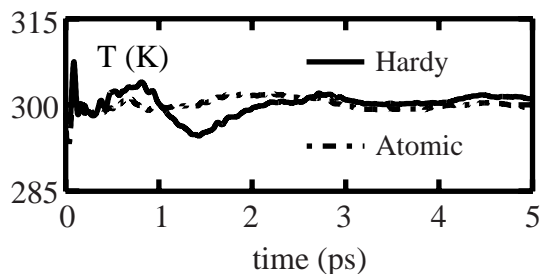


Figure 6.2: Hardy (solid curve) and atomic (broken) temperature as a function of sampling time for an NVT ensemble equilibrated to 300 K. The analysis volume is of size $R_c = 10$ Å.

within a few picoseconds of simulation. This analysis was repeated for a smaller sub-volume ($R_c = 6$ Å), and both Hardy and atomic expressions display greater variation. For both methods, sampling times greater than 5 ps were needed to converge on reasonable predictions of the expectation value.

6.4 Transient and Steady-State Heat Flow Simulations

We have investigated the non-uniform behavior of the expression for atomic temperature by performing MD simulations of steady-state, uni-directional heat flow. Although the concept of temperature is based in equilibrium theory, non-equilibrium definitions do exist and may

CHAPTER 6. EVALUATION OF TEMPERATURE AND HEAT IN ATOMISTIC SIMULATION

have physical significance as a measure of either kinetic or internal (kinetic plus potential) energy density for a sub-region in time and space.

Figures 6.3 and 6.4 show the atomic temperature distribution for an MD simulation configured to produce a constant heat flux. For this and the subsequent simulations, a constant heat flux algorithm (see Section 6.6) was used to specify heat flux boundary conditions. This was done within finite-sized cross-sectional slabs, the centers of which were separated by $\frac{L_x}{2}$ where L_x is the simulation box length in x (the heat flux direction). The simulation cell dimensions were 146 Å x 29 Å x 29 Å and cross-sectional analysis slabs for spatial averaging of temperature were approximately 10 Å wide along the long dimension. While the simulation cell as constructed has a symmetrical temperature gradient, we restrict our analysis to one half of the system. These simulations show temperatures reaching nearly

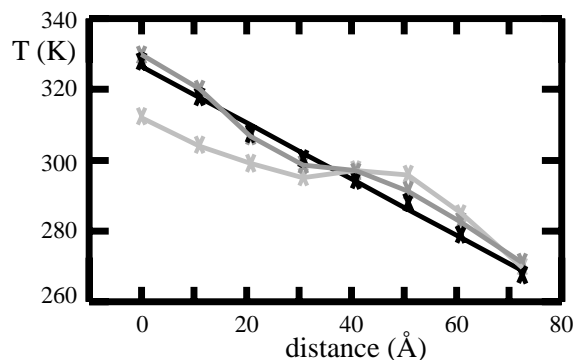


Figure 6.3: Temperature (T) as a function of length along the simulation cell. Data are shown at 10, 50, and 200 ps into the simulation. A least squares fit to the data at 200 ps is shown as the black line.

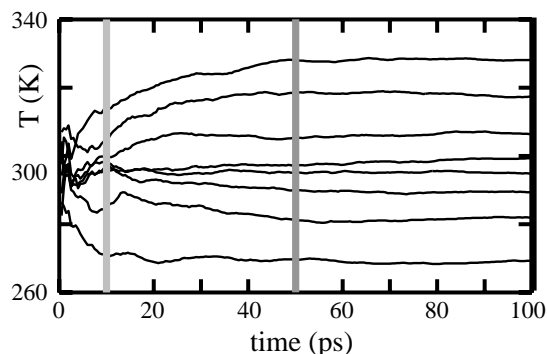


Figure 6.4: Temperature (T) as a function of time for constant heat flux simulations. The curves show T in successive analysis regions going from the heat injection region (top) to the heat extraction region (bottom). Vertical lines correspond to times at which T gradient data are presented in Figure 6.3

steady state values within 50 ps. After 200 ps, the temperature data is well fit to a linear relation. This linearity, although expected from continuum models of heat transport, is somewhat surprising given the extremely large magnitude of temperature gradient along with the small length and time scales over which temperature is being evaluated. Fig. 6.3 also displays the non-linear character of the transient regime. We are in the process of comparing this transient behavior with time-varying continuum models of heat transport, such as the Maxwell-Cattaneo equation [103].

We also analyzed the Hardy expressions for both temperature and heat flux for the steady-state heat flow scenario using a significantly larger system. MD simulations were done for a rectangular cross-section rod of copper, with dimensions $1453.102 \text{ \AA} \times 36.329 \text{ \AA} \times 36.326 \text{ \AA}$ containing 160,000 atoms. The initial temperature of the crystal was approximately 300 K. The cross-sectional slabs used for constant heat flux boundary conditions measured 36.325 \AA in the x (long) direction. Figure 6.5 displays the crystal composed of a *random* selection of 1600 spatial points, each colored according to its value of temperature. A value of $R_c = 10 \text{ \AA}$ was chosen and a normalized quartic function was used for ψ . For this figure, the entire system is shown, exhibiting the symmetry in temperature gradient mentioned earlier. Figure 6.5 shows a complex transient behavior that evolves to steady-state within

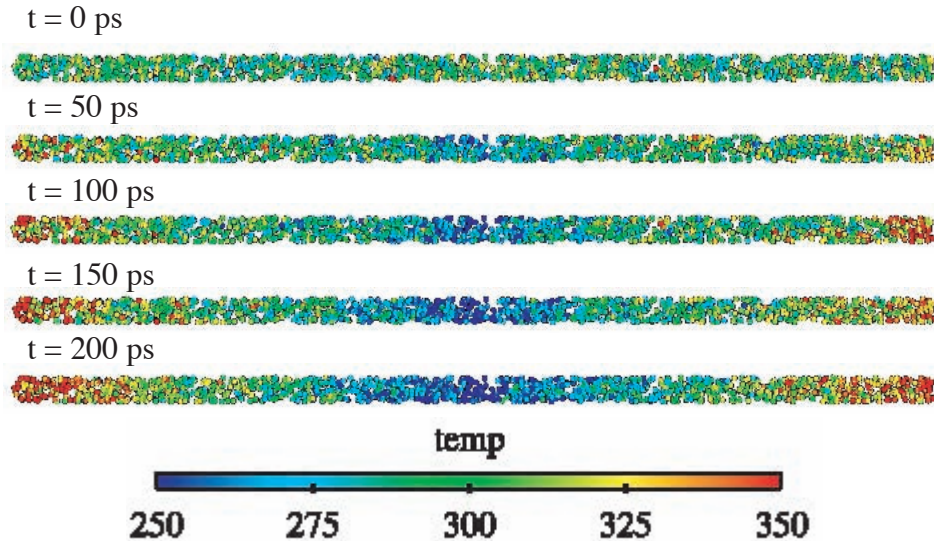


Figure 6.5: Hardy temperature (in units of K) for a random selection of spatial points. Frames correspond to the simulation times shown over which the transient heat flow evolves to steady-state.

~ 200 picoseconds. Accordingly, the final time frame depicted in Figure 6.5 qualitatively exhibits nearly linear distribution of temperature between the boundary condition regions.

The transient and steady-state behaviors of Hardy's temperature and heat flux expressions

CHAPTER 6. EVALUATION OF TEMPERATURE AND HEAT IN ATOMISTIC SIMULATION

can be better understood by examining their distributions along the long direction of the crystal. This is done by binning the observed values at the 1600 analysis spatial points along the x direction. The bin width in x is the same as that used for the thermal control regions, *i.e.* 36.325 Å. The results from this analysis are shown in Figures 6.6 and 6.7 for temperature (T) and heat flux in the x direction (q_x), respectively. Each of these figures displays the

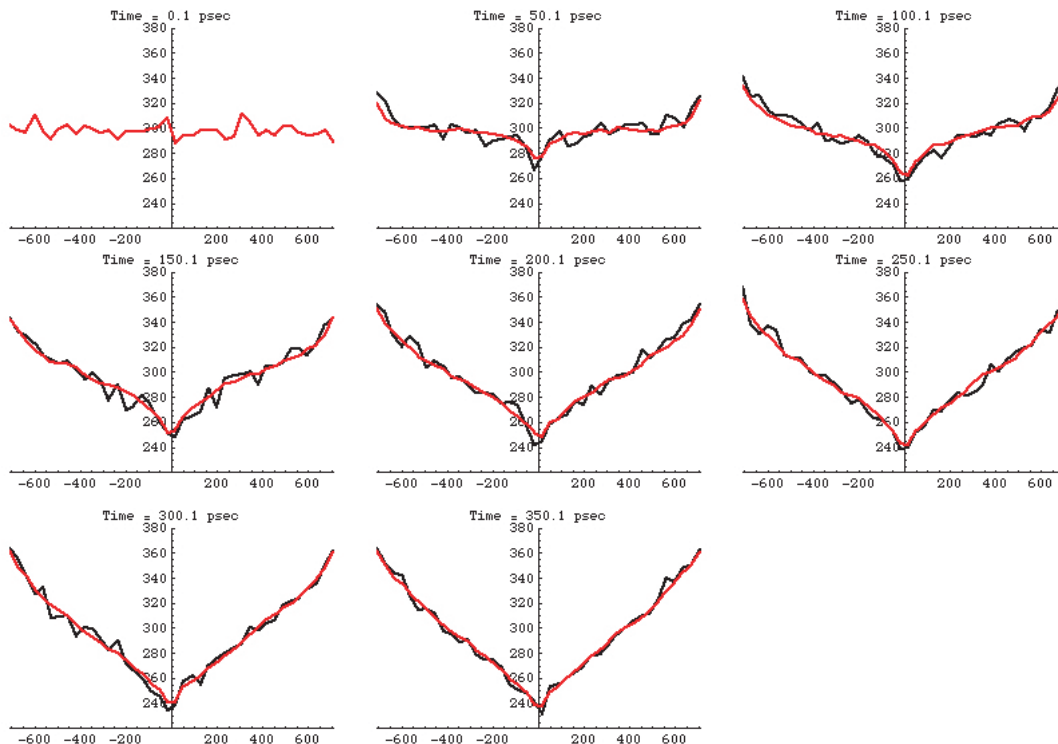


Figure 6.6: Distribution of temperature (in units of K) for binned regions along the length of the crystal shown in Figure 6.5. Each frame is labeled with the corresponding simulation time, and the black curve denotes the instantaneous distribution while the red curve denotes a time average of the distribution over a period of the 40 ps leading up to the time shown.

spatial distribution of either temperature or heat flux for several instances in time. For each time shown, a black curve is used to denote the instantaneous distribution while a red curve is used to denote the time averaged distribution over a period of 40 picoseconds leading up to the time displayed. While both the black and red curves in Figure 6.6 show an evolution to a linear distribution of temperature between the boundary condition regions, the spatial fluctuations are absent for the time averaged distribution. An estimate of the slope of the time averaged distribution in the long time limit is found to be 0.179 ± 0.002 K/Å. This quantity is an average of the absolute values of the slopes “measured” separately for both halves of the crystal, each of which lies within the uncertainty of the average value.

In Figure 6.7, it is observed that the fluctuations in heat flux greatly overwhelm the ex-

6.4. TRANSIENT AND STEADY-STATE HEAT FLOW SIMULATIONS

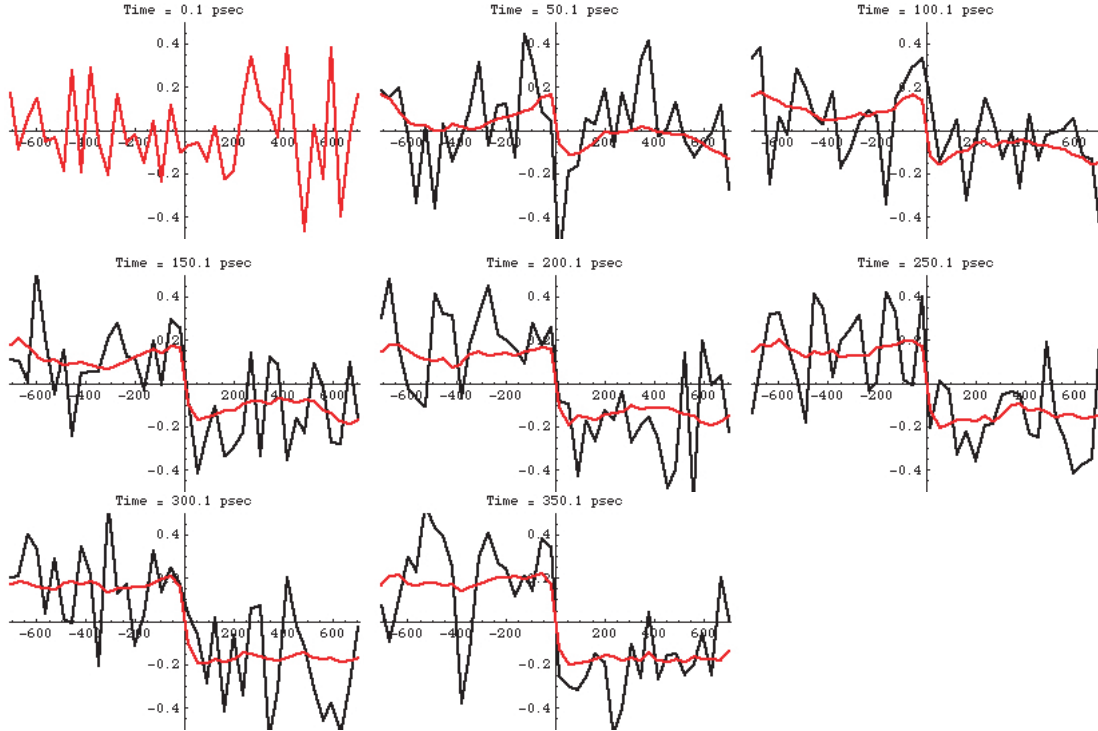


Figure 6.7: Distribution of heat flux component q_x (in units of $\text{nW}/\text{\AA}^2$) for binned regions along the length of the crystal shown in Figure 6.5. Each frame is labeled with the corresponding simulation time, and the black curve denotes the instantaneous distribution while the red curve denotes a time average of the distribution over a period of the 40 ps leading up to the time shown.

pectation value for the instantaneous calculation displayed by the black curves. However, computation of a time average of this distribution, shown by the red curves, reveals an evolution to a constant heat flux of nearly equal magnitude and opposite sign for the two halves of the crystal. An estimate of q_x after over 800,000 time steps is determined to be 0.20866 ± 0.01 nano-Watts/ \AA^2 , which is again an average of the magnitudes of q_x for the two halves of the crystal. This value is very close to, and within its uncertainty of, the prescribed heat flux of $0.20924 \text{ nW}/\text{\AA}^2$. Regarding thermal conductivity of the system, we assume Fourier's Law as the long-time behavior of the system. Thermal conductivity is then estimated by dividing q_x by the temperature gradient; this gives a value of $11.65 \pm 0.69 \text{ W}/(\text{m}\cdot\text{K})$, an uncertainty of approximately 6%.

In our simulations, we also observe the time evolution for the transverse heat flux component, q_y , shown in Figure 6.8. It is seen that while the instantaneous calculation of transverse heat flux can reach values nearly as large as those observed for q_x , the time average of this distribution quickly converges to much smaller values and deviates around a mean close to

CHAPTER 6. EVALUATION OF TEMPERATURE AND HEAT IN ATOMISTIC SIMULATION

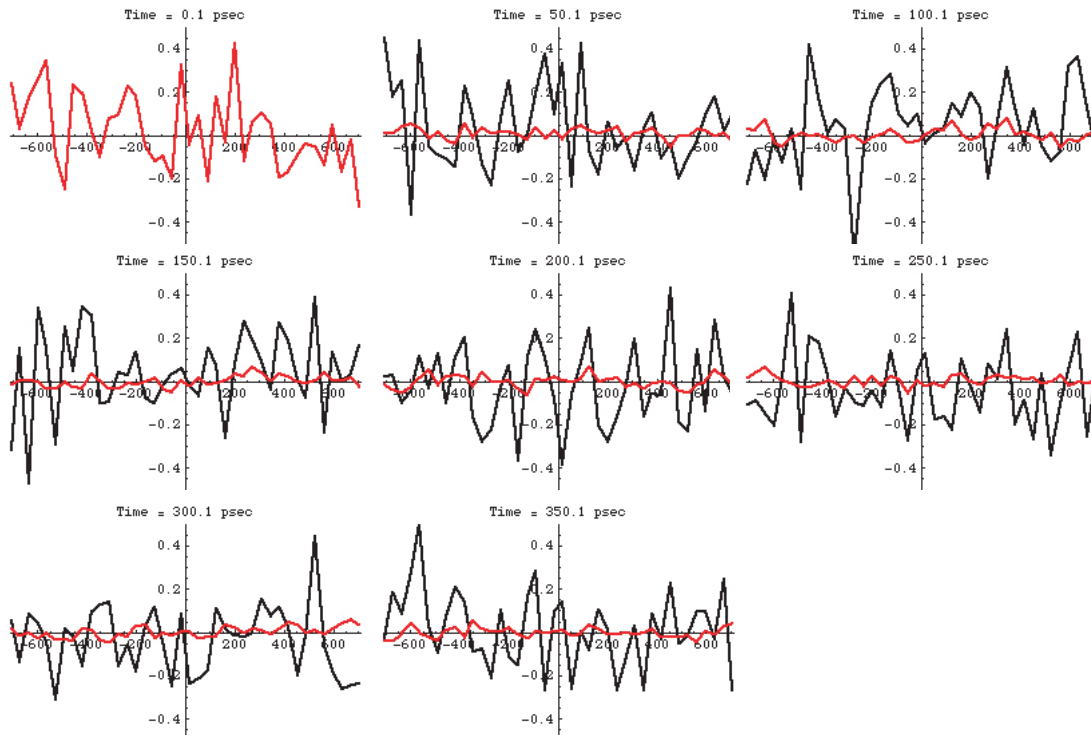


Figure 6.8: Distribution of heat flux component q_y (in units of $\text{nW}/\text{\AA}^2$) for binned regions along the length of the crystal shown in Figure 6.5. Each frame is labeled with the corresponding simulation time, and the black curve denotes the instantaneous distribution while the red curve denotes a time average of the distribution over a period of the 40 ps leading up to the time shown.

zero. The estimate for q_y after 800,000 time steps is determined to be $-0.00478 \text{ nW}/\text{\AA}^2$. Similarly, an estimate for q_z is determined to be $0.01398 \text{ nW}/\text{\AA}^2$.

We can compare these results with those obtained using a similar analysis that employs the atomistic expression for heat flux given by equation (6.4). As discussed earlier, this expression is typically evaluated for an entire equilibrium ensemble of atoms. Unlike Hardy's formalism for heat flux, there is no rule for handling interactions which span the analysis volume boundaries. They can be omitted from the calculation, included fully, or included to some degree. This, however, is what Hardy's formalism handles in a very physically reasonable sense. That is, the degree of inclusion of the contribution from an interaction that spans the analysis volume boundary is a weighted function of the percentage of the interaction distance which is included in the analysis volume. As a comparison, we have selected a single bin used in the Hardy heat flux averaging above and evaluated using equation (6.4) within that sub-system volume. This is done after the system has reached a steady-state condition, starting from $t = 700 \text{ ps}$. Presented in Figure 6.9 is the single bin running average for

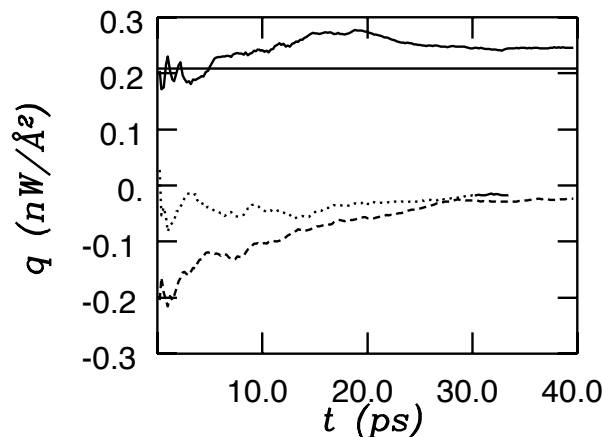


Figure 6.9: Heat flux (\mathbf{q}) given by the standard atomistic expression as a function of time for constant heat flux simulations. The curves show \mathbf{q} in the x (solid), y (dashed), and z (dotted) directions within one analysis bin used in Figure 6.7. A horizontal solid line shows the expectation value for q_x for the system.

heat flux in the x, y, and z directions over a simulation duration of 40 ps; this is the same averaging time used to obtain each bin data point in Figure 6.7. In this duration, the heat flux in y and z converge to a reasonable estimate of the expectation value (the calculated values are both $-0.02 \text{ nW}/\text{\AA}^2$ whereas the expectation value is zero). However, the value for heat flux calculated in the x direction, $0.245 \text{ nW}/\text{\AA}^2$, overestimates the expectation value, approximately $0.209 \text{ nW}/\text{\AA}^2$ as stated previously, by $\sim 17\%$. By this measure, the Hardy method appears superior over the standard atomistic expression, an expected result given the more reasonable way that the Hardy formalism handles interaction inclusion. Assuming Fourier’s Law as the long-time behavior of the system, we estimate the value of thermal conductivity to be $11.2 \pm 0.038 \text{ W}/(\text{m}\cdot\text{K})$. Richardson and Clancy [104] previously calculated a value of $5.66 \text{ W}/(\text{m}\cdot\text{K})$ for the same interatomic potential we employ herein. The origin for the discrepancy of the factor of 2 is unclear as details of how heat flux was quantified in those simulations are unknown. However, it is reassuring that the atomic and Hardy values of thermal conductivity are very similar, and that the heat flux is equally similar between the different expressions and the expectation value. In addition, our values come very close to a calculation of $9.6 \text{ W}/(\text{m}\cdot\text{K})$ done by Heino and Ristolainen [105] using an alternative EAM-type potential. Of course, since classical potentials have been used that ignore electronic degrees of freedom, only phonon modes of heat transfer are included. As such, the calculated values of thermal conductivity are orders of magnitude less than the experimentally measured value for Cu, approximately $385 \text{ W}/(\text{m}\cdot\text{K})$ [104]¹.

We are currently performing further analysis of the Hardy expressions for \mathbf{q} and T in order

¹In [104], the experimental value for thermal conductivity is misprinted. The surrounding text within the article was used to determine its correct value.

to compare their behavior with established continuum models of transient heat transport such as the Maxwell-Cattaneo equation.

6.5 Conclusions

We performed simulations examining the expression for atomic temperature and Hardy's expressions for both temperature and heat flux. The results from these simulations further supports the conclusion that Hardy's expressions accurately represent continuum-scale behavior once appropriate spatial and time-averaging has been performed. Future work will involve using these expressions to correlate continuum models of heat transport, such as the Maxwell-Cattaneo equation, with spatial and time averaged behavior in atomistic systems.

6.6 Appendix: Constant Heat Flux Algorithm

This section reviews the derivation of a velocity scaling algorithm for adding a constant amount of kinetic energy, per time step, to an atomistic region while not altering the total linear momentum of that same set of atoms. This derivation appears in an article by Ikeshoji and Hafskjold [106], however, those authors make some simplifying assumptions that actually make the derivation messier than it needs to be. The method was used by Lukes *et al.* [107] to prescribe a constant heat flux for a 3-D MD simulation of a rectangular region with a "hot" region at one end, where a constant amount of kinetic energy is added per time step, and a "cold" region at the other, where that same amount of kinetic energy is subtracted per time step. The derivation of this scaling method is as follows:

Suppose we select a sub-region of an atomistic system for which, at every time step, each atom's velocity will be scaled by some amount R and a constant velocity \mathbf{v}_{sub} is subtracted:

$$\mathbf{v}^\alpha \rightarrow (\mathbf{v}^\alpha)' = R\mathbf{v}^\alpha - \mathbf{v}_{\text{sub}} \quad \alpha \in \mathcal{N} \quad (6.7)$$

In the equation above, \mathcal{N} denotes the set of atoms within this controlled sub-region. The quantities of R and \mathbf{v}_{sub} can be determined by 2 conditions:

1. The total kinetic energy of the sub-region \mathcal{N} , $E_k = \frac{1}{2} \sum_{\alpha \in \mathcal{N}} m^\alpha (\mathbf{v}^\alpha)^2$, changes by a prescribed amount ΔE_k . Thus, $E'_k = E_k + \Delta E_k$.
2. The total linear momentum of the sub-region, $\mathbf{P} = \sum_{\alpha \in \mathcal{N}} m^\alpha \mathbf{v}^\alpha$ does not change. Thus, $\mathbf{P}' = \sum_{\alpha \in \mathcal{N}} m^\alpha (\mathbf{v}^\alpha)' = \mathbf{P}$.

If we enforce condition 2. and use the expression in equation (6.7),

$$\begin{aligned}
 \mathbf{P}' &= \mathbf{P} \\
 \sum_{\alpha \in \mathcal{N}} m^\alpha (\mathbf{v}^\alpha)' &= \mathbf{P} \\
 \sum_{\alpha \in \mathcal{N}} m^\alpha (R\mathbf{v}^\alpha - \mathbf{v}_{\text{sub}}) &= \mathbf{P} \\
 R \sum_{\alpha \in \mathcal{N}} m^\alpha \mathbf{v}^\alpha - \mathbf{v}_{\text{sub}} \sum_{\alpha \in \mathcal{N}} m^\alpha &= \mathbf{P} \\
 R\mathbf{P} - M\mathbf{v}_{\text{sub}} &= \mathbf{P}.
 \end{aligned}$$

Thus,

$$\mathbf{v}_{\text{sub}} = \frac{(R-1)\mathbf{P}}{M} = \frac{(R-1) \sum_{\alpha \in \mathcal{N}} m^\alpha \mathbf{v}^\alpha}{\sum_{\alpha \in \mathcal{N}} m^\alpha}. \quad (6.8)$$

We now enforce condition 1. and use the expressions in both equations (6.7) and (6.8):

$$\begin{aligned}
 E'_k &= \frac{1}{2} \sum_{\alpha \in \mathcal{N}} m^\alpha (\mathbf{v}^\alpha)' \cdot (\mathbf{v}^\alpha)' \\
 &= \frac{1}{2} \sum_{\alpha \in \mathcal{N}} m^\alpha \left(R\mathbf{v}^\alpha - \frac{(R-1)\mathbf{P}}{M} \right) \cdot \left(R\mathbf{v}^\alpha - \frac{(R-1)\mathbf{P}}{M} \right) \\
 &= \frac{1}{2} \sum_{\alpha \in \mathcal{N}} m^\alpha \left(R^2 \mathbf{v}^\alpha \cdot \mathbf{v}^\alpha - 2R \frac{(R-1)}{M} \mathbf{P} \cdot \mathbf{v}^\alpha + (R-1)^2 \frac{\mathbf{P} \cdot \mathbf{P}}{M^2} \right) \\
 &= R^2 E_k - R(R-1) \frac{\mathbf{P}^2}{M} + \frac{1}{2} (R-1)^2 \frac{\mathbf{P}^2}{M} \\
 &= R^2 E_k - \frac{1}{2} (2R^2 - 2R - R^2 + 2R - 1) \frac{\mathbf{P}^2}{M} \\
 &= R^2 E_k - \frac{1}{2} (R^2 - 1) \frac{\mathbf{P}^2}{M},
 \end{aligned}$$

where $\mathbf{P}^2 = \mathbf{P} \cdot \mathbf{P}$. We can re-arrange this equation to isolate the R-terms,

$$E'_k - \frac{1}{2} \frac{\mathbf{P}^2}{M} = R^2 \left(E_k - \frac{1}{2} \frac{\mathbf{P}^2}{M} \right),$$

and then solve for R,

$$R^2 = \frac{\left(E'_k - \frac{1}{2} \frac{\mathbf{P}^2}{M} \right)}{\left(E_k - \frac{1}{2} \frac{\mathbf{P}^2}{M} \right)}.$$

Thus,

$$R = \sqrt{\frac{E'_k - \frac{1}{2} \frac{\mathbf{P}^2}{M}}{E_k - \frac{1}{2} \frac{\mathbf{P}^2}{M}}} = \sqrt{\frac{E_k + \Delta E_k - \frac{1}{2} \frac{\mathbf{P}^2}{M}}{E_k - \frac{1}{2} \frac{\mathbf{P}^2}{M}}}. \quad (6.9)$$

This end result makes perfect sense. We are simply doing a velocity scaling by multiplying each velocity times the square-root of the ratio of desired kinetic energy to original kinetic energy. However, since we are not guaranteed that the sub-region being scaled has net zero linear momentum, we must subtract the “macroscopic kinetic energy” from both terms in the ratio R , and subtract a small amount of velocity, \mathbf{v}_{sub} , from each atom to ensure conservation of momentum. In the limit that the sub-region has net zero momentum, $\mathbf{v}_{\text{sub}} = \mathbf{0}$ and $R = \sqrt{E'_k/E_k}$, the “normal” velocity scaling method. It is also obvious that for the addition of kinetic energy ($\Delta E_k > 0$), $R > 1$ and $\mathbf{v}_{\text{sub}} \cdot \mathbf{P} > 0$, while for the subtraction of kinetic energy ($\Delta E_k < 0$), $R < 1$ and $\mathbf{v}_{\text{sub}} \cdot \mathbf{P} < 0$.

Both references listed above apply this method to a long, rectangular box for which a few atomic layers on one end is deemed “hot” and has a constant $\Delta E_k = \Delta_H > 0$ for every time step while at the other end, a few atomic layers are deemed “cold” and $\Delta E_k = \Delta_C = -\Delta_H < 0$. Once the system attains a steady-state, the 1-dimensional heat flux is quantified as

$$q = \frac{\Delta_H}{2A\Delta t}, \quad (6.10)$$

where A is the cross-sectional area of the box perpendicular to the long direction and Δt is the time step.

Chapter 7

Thermo-mechanical Coupling of Atomistic and Continuum Systems

Principle Authors: R.E. Jones, C.J. Kimmer and G.J. Wagner

7.1 The Continuum Initial-Boundary Value Problem

The motion $\mathbf{x} = \chi(\mathbf{X}, t)$ and (absolute) temperature $\theta = \Theta(\mathbf{X}, t)$ fields of a continuum body are functions of positions \mathbf{X} in a reference state and time t . They need to satisfy balances of mass, linear momentum, angular momentum and energy of the form:

$$\frac{d}{dt} \int_{\Omega} \phi \rho \, dv = B_{\phi} + S_{\phi} , \quad (7.1)$$

which states that the time rate of change of the quantity ϕ in any material region Ω is equal to the external body sources B_{ϕ} and surface sources S_{ϕ} . In the generic balance equation (7.1), ρ is the mass density. For instance, the balance of energy

$$\frac{d}{dt} \int_{\Omega} \left(\epsilon + \frac{1}{2} \dot{\mathbf{x}} \cdot \dot{\mathbf{x}} \right) \rho \, dv = \int_{\Omega} (\mathbf{b} \cdot \dot{\mathbf{x}} + r) \rho \, dv + \int_{d\Omega} \mathbf{t} \cdot \dot{\mathbf{x}} - \mathbf{q} \cdot \mathbf{n} \, da , \quad (7.2)$$

relates the time rate of change of the internal energy ϵ and kinetic energy to the work done by mechanical sources, \mathbf{b} being the external body force and \mathbf{t} the surface traction, and the heat supplied by external generation r and flux \mathbf{q} . The outward unit normal to $d\Omega$ is denoted by \mathbf{n} .

For a classical continuum that has no external couples and satisfies mass continuity, the four balances reduce to a local balance of linear momentum

$$\rho \ddot{\mathbf{x}} = \partial_{\mathbf{x}} \cdot \mathbf{T} + \rho \mathbf{b} , \quad (7.3)$$

where \mathbf{T} is the (symmetric) Cauchy stress and \mathbf{b} is a body force, and a local balance of energy

$$\rho \dot{\epsilon} = \mathbf{T} \cdot \mathbf{L} + \rho r - \partial_{\mathbf{x}} \cdot \mathbf{q} , \quad (7.4)$$

where ϵ is internal energy, $\mathbf{L} = \partial_{\mathbf{x}} \dot{\mathbf{x}}$ is the velocity gradient, r is external heat supply, and \mathbf{q} is heat flux. When referred back to the reference configuration these local balances become

$$\rho_0 \ddot{\mathbf{x}} = \partial_{\mathbf{X}} \cdot \mathbf{P} + \rho_0 \mathbf{b} , \quad (7.5)$$

and

$$\rho_0 \dot{\epsilon} = \mathbf{P} \cdot \dot{\mathbf{F}} + \rho_0 r - \partial_{\mathbf{X}} \cdot \mathbf{h} , \quad (7.6)$$

where $\mathbf{F} = \partial_{\mathbf{X}} \chi$ is the deformation gradient, $\rho_0 = \det(\mathbf{F})\rho$ is the reference mass density, and the referential heat flux \mathbf{h} is given by $\mathbf{h} = \det(\mathbf{F})\mathbf{F}^{-T}\mathbf{q}$. The relationship between the Cauchy stress \mathbf{T} , the first Piola-Kirchoff stress \mathbf{P} and second Piola-Kirchoff stress \mathbf{S} is

$$\det(\mathbf{F})\mathbf{T} = \mathbf{P}\mathbf{F}^T = \mathbf{F}\mathbf{S}\mathbf{F}^T . \quad (7.7)$$

Note that the stress power term $\mathbf{P} \cdot \dot{\mathbf{F}}$ in (7.6) is equivalent to $\mathbf{S} \cdot \dot{\mathbf{E}}$, where $\mathbf{E} = \frac{1}{2}(\mathbf{F}^T\mathbf{F} - \mathbf{I})$ is the Lagrange strain.

The usual boundary conditions for the deformation-heat flux problem are prescribed fields or fluxes (in this case, in the current configuration)

$$\begin{cases} \mathbf{x} = \bar{\mathbf{x}}(t) \\ \mathbf{t} = \bar{\mathbf{t}}(t) \end{cases} \quad \text{and} \quad \begin{cases} \theta = \bar{\theta}(t) \\ \mathbf{q} = \bar{\mathbf{q}}(t) \end{cases} \quad \text{on } d\Omega \quad (7.8)$$

and the initial conditions are given by functions $\mathbf{x}(\mathbf{X}, t = 0) = \mathbf{x}_0(\mathbf{X})$, $\dot{\mathbf{x}}(\mathbf{X}, t = 0) = \mathbf{v}_0(\mathbf{X})$ and $\theta(\mathbf{X}, t = 0) = \theta_0(\mathbf{X})$ over the entire domain Ω .

Solution of equations (7.3) and (7.4) requires additional constitutive relations between the kinematic and kinetic variables. The constitutive response of the body is determined by stress and heat flux behavior and typically requires a certain degree of smoothness from $\{\chi, \Theta\}$. Commonly, stress is given by a phenomenological based function of kinematic quantities derived from $\{\chi, \Theta\}$. In certain cases, stress is derivable from the free energy Ψ via

$$\mathbf{S} = \rho_0 \partial_{\mathbf{E}} \Psi|_{\theta} . \quad (7.9)$$

The (Helmholtz) free energy $\Psi(\mathbf{E}, \theta)$ ¹ is a Legendre transform of the internal energy $\epsilon(\mathbf{E}, \eta)$

$$\Psi = \Psi(\mathbf{E}, \theta) = \epsilon - \theta\eta \quad (7.10)$$

¹The assumption that Ψ is solely dependent on \mathbf{E} and θ is tantamount to assuming thermoelastic behavior, as will be shown in subsequent developments.

where $\theta = \partial_\eta \epsilon|_{\mathbf{E}}$, and is interpreted as the amount of energy available for work at constant temperature. So given an internal energy ϵ a prescription for determining entropy η is necessary to determine stress in this fashion.

The Clausius integral, which measures the influx of heat over temperature,

$$\mathcal{C} = \int \int_{\Omega} \frac{r}{\theta} dv - \int_{d\Omega} \mathbf{h} \cdot \mathbf{N} da dt = \int \int_{\Omega} \frac{r}{\theta} - \frac{1}{\rho_0} \partial_{\mathbf{X}} \cdot \frac{\mathbf{h}}{\theta} dv dt \quad (7.11)$$

is key to the concept of entropy and the second law of thermodynamics (here \mathbf{N} is the outward unit normal to the reference configuration). A version of the second law states that for a cyclic processes

$$\mathcal{C} \leq 0. \quad (7.12)$$

For a reversible cyclic process the value of \mathcal{C} must not decrease regardless of the sense of the cycle, so \mathcal{C} must be zero and therefore the integrand of (7.11) is a function of the (initial) state. For processes that maintain zero heat flux,² the Clausius integral is path independent in $\{\mathbf{E}, \theta\}$ -space. Consequently, it provides a means of constructing a state function, entropy η ,

$$\eta - \eta_0 = \mathcal{C}|_{\mathbf{h}=0} = \int \frac{r}{\theta} dt = \int \frac{1}{\theta} (\dot{\epsilon} - \frac{1}{\rho_0} \mathbf{S} \cdot \dot{\mathbf{E}}) dt. \quad (7.13)$$

For the same processes, the balance of energy (7.6) and the definitions (7.10) and (7.13) gives

$$(\rho_0 \partial_{\mathbf{E}} \Psi - \mathbf{S}) \cdot \dot{\mathbf{E}} + \rho_0 (\partial_\theta \Psi + \eta) \cdot \dot{\theta} = \mathbf{0}, \quad (7.14)$$

from which the Gibb's relations

$$\mathbf{S} = \rho_0 \partial_{\mathbf{E}} \Psi|_{\theta} \quad \text{and} \quad \eta = - \partial_\theta \Psi|_{\mathbf{E}} \quad (7.15)$$

can be deduced by arguing that the rates $\dot{\mathbf{E}}$ and $\dot{\theta}$ are arbitrary and the quantities in parenthesis do not depend on $\dot{\mathbf{E}}$ and $\dot{\theta}$. Two other processes that are clearly reversible, although more trivial, are: a) processes that are adiabatic and isentropic and b) isothermal processes with reversible heat transfer. For an adiabatic and isentropic process, the definition $\epsilon = \epsilon(\mathbf{E}, \eta)$ and the balance of energy gives

$$\begin{aligned} \rho_0 \dot{\epsilon}(\mathbf{E}, \eta) &= \rho_0 \partial_{\mathbf{E}} \epsilon \cdot \dot{\mathbf{E}} + \rho_0 \partial_\eta \epsilon \dot{\eta} \\ &= \mathbf{S} \cdot \dot{\mathbf{E}} + \rho_0 r - \partial_{\mathbf{X}} \cdot \mathbf{h}. \end{aligned} \quad (7.16)$$

Since the process is adiabatic $\rho_0 r - \partial_{\mathbf{X}} \cdot \mathbf{h} = 0$, which also implies $\dot{\eta} = 0$, so, in this case, $\mathbf{S} = \partial_{\mathbf{E}} \epsilon = d_{\mathbf{E}} \epsilon|_{\eta}$ and ϵ is the potential for stress at constant entropy. For an isothermal process with reversible heat transfer

$$\begin{aligned} \rho_0 \dot{\Psi} &= \rho_0 \partial_{\mathbf{E}} \Psi \cdot \dot{\mathbf{E}} - \rho_0 \partial_\theta \Psi \dot{\theta} \\ &= \mathbf{S} \cdot \dot{\mathbf{E}} + \rho_0 r - \partial_{\mathbf{X}} \cdot \mathbf{h} - (\rho_0 \dot{\eta} \theta + \rho_0 \eta \dot{\theta}). \end{aligned} \quad (7.17)$$

²For certain materials, non-trivial processes that satisfy these conditions may require complex \mathbf{r} fields.

A process being isothermal gives $\dot{\theta} = 0$ and reversible heat transfer implies that

$$\dot{\eta} = \frac{1}{\theta} \left(r - \frac{1}{\rho_0} \partial_{\mathbf{x}} \cdot \mathbf{h} \right), \quad (7.18)$$

so Ψ is the potential for stress at constant temperature, as was shown in (7.15).³

Due to second law considerations, the heat flux depends on the temperature gradient $\partial_{\mathbf{x}}\theta$, as well as deformation and temperature,

$$\mathbf{q} = \mathbf{q}(\mathbf{F}, \theta, \partial_{\mathbf{x}}\theta), \quad (7.19)$$

where $\mathbf{q}(\mathbf{F}, \theta, \partial_{\mathbf{x}}\theta = \mathbf{0}) = \mathbf{0}$ on physical grounds. The process $\{\chi, \Theta\}$ is not only governed by (7.3) and (7.4) but by the second law, which in (local) Clausius-Duhem form is

$$\rho_0 \theta \dot{\eta} \geq \rho_0 r - \partial_{\mathbf{x}} \cdot \mathbf{h} + \frac{1}{\theta} \mathbf{h} \cdot \partial_{\mathbf{x}} \theta. \quad (7.20)$$

A direct consequence of (7.20) is simply $\mathbf{h} \cdot \partial_{\mathbf{x}} \theta \leq 0$. This result is clearly seen after use in (7.20) of the (local) balance of energy in the form

$$\rho_0 \theta \dot{\eta} = \rho_0 r - \partial_{\mathbf{x}} \cdot \mathbf{h}, \quad (7.21)$$

which results from (7.15), (7.10) and (7.6).

7.1.1 Examples

For the specific example of the thermoelastic fluid called an ‘ideal’ gas, the Cauchy stress is given by

$$\mathbf{T} = \mathbf{T}(\mathbf{F}, \theta) = \bar{R} \rho \mathbf{I}, \quad (7.22)$$

where \bar{R} is a constant, $\rho = \rho_0 \det^{-1}(\mathbf{F})$, and $\epsilon = \epsilon(\theta)$ is not a function of \mathbf{F} since the gas particles do not interact. Applying (7.13) results in

$$\eta - \eta_0 = \int \frac{\dot{\epsilon}(\theta)}{\theta} dt - \int \bar{R} \frac{\dot{\rho}}{\rho} dt = c_v \ln \frac{\theta}{\theta_0} - \bar{R} \ln \frac{\rho}{\rho_0}, \quad (7.23)$$

which is clearly integrable for the special case where $c_v = \partial_{\theta} \epsilon$ is constant. The free energy Ψ consistent with this entropy gives the interesting result that stress for an ideal gas $\mathbf{P} = -\theta \partial_{\mathbf{F}} \eta$

³There is a slight but important inconsistency between (7.18) and the definitions (7.11) and (7.12) in the case of non-uniform temperature distributions. It stems from the continuum interpretation of $\int \frac{dQ}{\theta}$, where Q is the heat added at temperature θ . Some interpretations bring the heat flux into the volume integral then divide by temperature and others do the reverse. These statements are not equivalent, i.e. $\frac{1}{\rho_0} \partial_{\mathbf{x}} \cdot \frac{\mathbf{h}}{\theta} \neq \frac{1}{\rho_0 \theta} \partial_{\mathbf{x}} \cdot \mathbf{h}$, unless the region is homothermal, $\partial_{\mathbf{x}} \theta = \mathbf{0}$. The definition (7.13) side-steps this issue by eliminating the surface heat flux \mathbf{h} .

is directly related to entropy change (and not dependent on internal energy as it would be in an elastic solid). To pose the full thermodynamic problem a heat flux relation would need to be given.

On the other hand, starting with a quadratic free energy⁴

$$\Psi = \frac{1}{2}\epsilon \cdot \mathbb{C}\epsilon - \epsilon \cdot \mathbf{M}\vartheta - \frac{1}{2}\frac{c}{\theta_0}\vartheta^2 \quad (7.24)$$

in terms of the small strain measure ϵ (the linearization of \mathbf{E} about a strain-free reference configuration) and the relative temperature $\vartheta = \theta - \theta_0$ (θ_0 being the reference temperature), the equations of linear thermoelasticity

$$\rho\ddot{\mathbf{x}} = \partial_{\mathbf{x}} \cdot (\mathbb{C}\epsilon - \mathbf{M}\vartheta) \quad (7.25)$$

$$\frac{c}{\theta_0}\dot{\vartheta} = \partial_{\mathbf{x}} \cdot \left(\frac{1}{\theta_0}\mathbf{K}\partial_{\mathbf{x}}\vartheta\right) - \mathbf{M} \cdot \partial_{\mathbf{x}}\dot{\mathbf{x}} \quad (7.26)$$

result from (7.3), (7.21), (7.15) and Fourier's Law $\mathbf{q} = -\mathbf{K}\partial_{\mathbf{x}}\theta$.⁵ Note that the free energy determines the stress and the entropy but only the Clausius-Duhem inequality puts any constraints on what the heat flux can be. In (7.24), the elasticity tensor $\mathbb{C} = \partial_{\mathbf{E}}^2\Psi(\mathbf{0}, \theta_0)$, the thermo-mechanical coupling tensor \mathbf{M} , and the conductivity tensor \mathbf{K} are constants. For an isotropic body, the constants reduce to well-known quantities: $\mathbb{C} = \lambda\mathbf{I} \otimes \mathbf{I} + 2\mu\mathbb{I}$ where λ and μ are Lamé constants, $\mathbf{K} = k\mathbf{I}$ where k is the usual heat conductivity, and $\mathbf{M} = 3(\lambda + \frac{2}{3}\mu)\alpha\mathbf{I}$ where α is the coefficient of linear thermal expansion.

A third example, the Maxwell-Cattaneo rigid heat conductor, does not quite fall into the thermoelastic class of materials since its behavior depends on $\{\mathbf{E} = \mathbf{0}, \theta, \mathbf{h}\}$ not $\{\mathbf{E}, \theta, \partial_{\mathbf{x}}\theta\}$. From its constitutive relations for heat flow

$$\mathbf{C}\dot{\mathbf{h}} + \mathbf{h} = \mathbf{K}\partial_{\mathbf{x}}\theta, \quad (7.27)$$

where \mathbf{K} is positive definite and $\mathbf{Z} = \mathbf{K}^{-1}\mathbf{C}$ is symmetric, and internal energy

$$\epsilon = \epsilon(\theta, \mathbf{h}) = e_0(\theta) - \frac{1}{2}\mathbf{h} \cdot \theta^2 \frac{d}{d\theta} \left(\frac{1}{\theta^2}\mathbf{Z}(\theta) \right) \mathbf{h}, \quad (7.28)$$

and the balance of energy (7.6) with $\dot{\mathbf{E}} = \mathbf{0}$, an entropy

$$\eta = \eta_0(\theta) - \frac{1}{2}\mathbf{h} \cdot \frac{d}{d\theta} \left(\frac{1}{\theta}\mathbf{Z}(\theta) \right) \mathbf{h} \quad (7.29)$$

⁴This quadratic form of the free energy leads to an internal energy $\epsilon = \frac{1}{2}\epsilon \cdot \mathbb{C}\epsilon + \frac{1}{2}\frac{c}{\theta_0}\vartheta^2$, and both energies are consistent with the idea that the "strain energy" for an isothermal, infinitesimally deforming solid should be convex.

⁵Fourier's law can be seen as the analogue to linear elasticity for heat conduction, i.e. a first order constitutive relation. It also leads to the concept of temperature being the potential for heat flow.

and a free energy

$$\Psi = e_0(\theta) - \theta\eta_0(\theta) + \frac{1}{2}\mathbf{h} \cdot \frac{1}{\theta}\mathbf{Z}(\theta)\mathbf{h} \quad (7.30)$$

can be derived. The constitutive relations and the balance of energy need to be solved simultaneous,

$$\mathbf{C}\dot{\mathbf{h}} = \mathbf{K}\partial_{\mathbf{x}}\theta - \mathbf{h} \quad (7.31)$$

$$\rho_0\left(\frac{d}{d\theta}e_0(\theta) - \frac{d}{d\theta}\left(\frac{1}{2}\mathbf{h} \cdot \theta^2 \frac{d}{d\theta}\left(\frac{1}{\theta^2}\mathbf{Z}\right)\mathbf{h}\right)\right)\dot{\theta} = \rho_0 r - \partial_{\mathbf{x}} \cdot \mathbf{h} + \rho_0 \frac{1}{2}\mathbf{h} \cdot \frac{d}{d\theta}\left(\frac{1}{\theta^2}\mathbf{Z}\right)\mathbf{C}^{-1}(\mathbf{K}\partial_{\mathbf{x}}\theta - \mathbf{h})$$

and are considerably more complex than (7.26) with $\epsilon = \mathbf{0}$, even when reduced to their simplest form

$$\begin{aligned} \dot{\mathbf{h}} &= \frac{k}{c}\partial_{\mathbf{x}}\theta - \frac{1}{c}\mathbf{h}, \\ \dot{\theta} &= \frac{1}{\epsilon\theta - \frac{c}{k}\mathbf{h} \cdot \mathbf{h}}\left(-\frac{1}{\rho_0}\partial_{\mathbf{x}} \cdot \mathbf{h} - \frac{1}{\theta^3}\mathbf{h} \cdot (\partial_{\mathbf{x}}\theta - \frac{1}{k}\mathbf{h})\right), \end{aligned} \quad (7.32)$$

where $\mathbf{K} = k\mathbf{I}$, $\mathbf{C} = c\mathbf{I}$, $e_0 = \frac{\epsilon}{2}\theta^2$ and $r = 0$. Also, this system of equations does not have the clearly parabolic character of the classical heat equation. This ‘relaxation’ model of heat conduction gives a finite speed of propagation to a heat pulse, as opposed to the infinite propagation speed modeled by the heat equation based on Fourier’s law.

7.2 The Atomistic Initial-Boundary Value Problem

The atomistic system of particles $\alpha = 1..N$ is governed solely by Newton’s law

$$m^\alpha \ddot{\mathbf{x}}^\alpha = \mathbf{f}^\alpha \quad (7.33)$$

where m^α is the particle mass, \mathbf{x}^α is the particle position and f^α is the external force on the particle. Typically the force \mathbf{f}^α on the particles is derived from a (global) potential energy $\Phi(\mathbf{x}^\alpha)$ via

$$\mathbf{f}^\alpha = \partial_{\mathbf{x}^\alpha}\Phi, \quad (7.34)$$

and, in this case, the system is conservative with a Hamiltonian or total energy \mathcal{H}

$$\mathcal{H} = \sum_{\alpha} \left(\frac{1}{2} m^\alpha \dot{\mathbf{x}}^\alpha \cdot \dot{\mathbf{x}}^\alpha \right) + \Phi(\mathbf{x}^\alpha). \quad (7.35)$$

The constitutive behavior of the system is directly related to the form of $\Phi(\mathbf{x}^\alpha)$ since it relates deformation to internal forces. The solution $\mathbf{x}^\alpha = \chi^\alpha(t)$ to (7.33), subject to appropriate initial and boundary conditions, is assumed to be C^2 .

From the solution $\chi^\alpha(t)$ it is possible to compute *a posteriori* thermodynamic measures for sets of particles using concepts from statistical mechanics. For instance, a kinetic definition of temperature is

$$\theta_S = \left(\frac{3}{2}k_B \sum_{\alpha \in S} m^\alpha\right)^{-1} \left\langle \frac{1}{2} \sum_{\alpha \in S} m^\alpha \dot{\mathbf{x}}^\alpha \cdot \dot{\mathbf{x}}^\alpha \right\rangle, \quad (7.36)$$

where $\langle \bullet \rangle$ represents a long time or ensemble average and k_B is Boltzmann's constant.

7.3 Coupling Molecular Dynamics with Continuum Finite Elements

Fundamental to the coupling problem is the fact that the motion of the atoms χ^α is interpreted as motion of mass χ and temperature Θ by the continuum. Naively, the continuum motion is related to long wavelength elastic waves in the atomic crystal and the temperature comprises the remaining short wavelength atomic motion. The heat-bulk motion transition

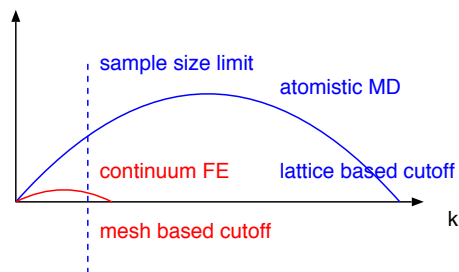


Figure 7.1: Generic dispersion curves for MD and FE

length-scale maybe on the order of the lattice parameter. There are other length-scales to consider which result from the dispersion curves illustrated in Figure 7.1. The small wavelength limit for an atomistic simulation is on the order of the lattice parameter. While there is theoretically no large wavelength limit, the use of numerical simulation methods result in an upper wavelength limit determined by the size of the sample in the simulation. The finite element method of representing a linear elastic medium has a similar dispersion curve artificially induced by the algorithm and dependent on the mesh size. Clearly, a finite element representation of a continuum is opaque to shorter wavelengths than the mesh size. So inevitably the mesh size of the finite element representation will determine the smallest wave that is interpreted as bulk motion and this lower limit must be greater than the highest wavelength that can be represented in the atomistic region to have non-trivial coupling.

The concept of thermodynamic equilibrium, which is assumed by classical continuum mechanics, leads to the idea that the atomistic and continuum simulations run at different

timescales. A thermometer is a good illustration of why there are different timescales to the two models. A thermometer takes an ensemble average (or time average if ergodicity is assumed) of the kinetic energy of the fluid’s atoms near the thermometer. The mean-time between impacts of atoms is a measure of the atomistic timescale which is extremely small when compared to the response time of the thermometer measuring the continuum temperature.⁶

So there is a need to bring atomistic kinematic quantities up to the continuum length and time scales. Hardy’s method [52] for spatial homogenization can be extended to temporal homogenization. The kinetic fields need a similar treatment. It is not clear whether it is more convenient to use energy or energy duals to primary fields e.g. stress is the dual to strain and entropy is the dual to temperature. The energy approach is attractive since it allows for different sources of energy, e.g. particle kinetic energy versus continuum thermal energy, to be accounted for without bothering with the details. It does not, however, provide a means of deriving the form of the continuum heat flux, as noted previously. Also, total energy, kinetic plus potential, is natural to atomistic systems and for small motions, with no change in association, atomistic systems are conservative. Whereas, in a continuum, the free energy is usually the basis for thermoelastic materials since free energy is minimized at equilibrium.⁷ Unfortunately, free energy can only be derived from atomistic simulations by complex post-processing based on statistical mechanics. Another issue to consider is what domains in the simulation need atomistic representation and what domains can be represented by continuum and where do they interact: on an interface, over an overlap of finite size or should one region be a (proper) subset the other.

7.4 A Model Problem

To begin with, a model problem should be as simple as possible. A one-dimensional geometry reduces the complexity of the waves that are possible and simplifies the boundary to a point. (There are some costs for this choice, not the least of which is the potential for behavior that is not typical of larger three-dimensional systems [108]). To study the flow of heat, an atomistic representation coupled to a continuum rigid conductor is ideal since the motion-temperature split becomes unambiguous. In order to maintain the validity of this pairing, the atomistic region needs to be limited to small wavelength ‘thermal’ motions.

The first test to validate the method should be a verification of basic consistency between a homogenized version of the atomistic system and the continuum, i.e. does the kinetic tem-

⁶Whether the (local) equilibrium assumed by continuum mechanics is equivalent to requiring reversible thermodynamics is too involved to discuss here.

⁷Also, Gibbs variational principle states that entropy is maximized at equilibrium subject to the constraint of constant energy.

perature calculated from molecular dynamics look like the empirical temperature calculated by finite elements for a corresponding initial-boundary value problem. As Figure 7.2 shows,

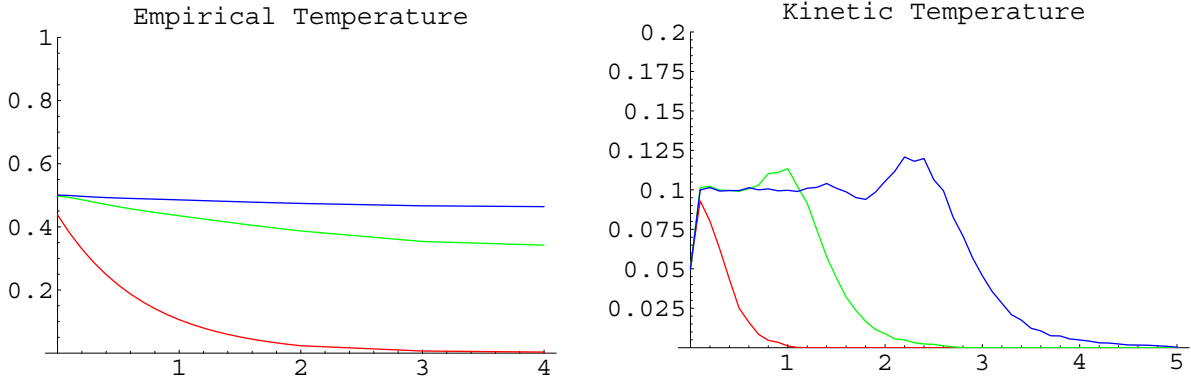


Figure 7.2: Empirical Temperature versus Kinetic Temperature

the empirical temperature calculated by the classical heat equation based on Fourier's law and constant end temperature does not correlate well with the kinetic temperature derived from a molecular dynamics simulation of atoms interacting with a linear force relation and input of a constant frequency wave. The main difference between the parabolic heat equation's solution and the post-processed hyperbolic solution to the atomistic simulation is the infinite versus finite speed of propagation. The instant after the initiation time, the far end of the classical conductor experiences a rise in temperature. In the atomistic system the heat wave takes a finite amount of time to transverse the domain and this energy travels at the group velocity of the displacement waves. Clearly, to make a correspondence between the parameters of the two systems is futile and a rigid-heat conductor with a finite propagation speed, such as the Maxwell-Cattaneo conductor, would be more appropriate for these conditions.

A second test consists of seamlessly passing information from the atomistic region to the continuum and vice versa. In this case, it would mean atomistic waves passing into the continuum as heat and heat passing into the atomistic region as small wavelength energy. A simple means of coupling a one-dimensional molecular dynamics simulation to a one-dimensional finite element representation of a heat conductor was tried with limited success. The interface between the two regions was taken to be a single point and the kinetic temperature

$$\theta^k = \frac{1}{KN\Delta t_{MD}} \sum_{t \in (t_i, t_i + N\Delta t_{MD})} m^\alpha \mathbf{v}^\alpha \cdot \mathbf{v}^\alpha$$

was applied to the finite element region. Here Δt_{MD} is the time-step of the molecular dynamics simulation and $\Delta t_{MD} = N\Delta t_{MD}$ is the time-step of the finite element simulation (N is a natural number). To provide coupling of the dynamics of the boundary atoms to

the conditions in the finite element region the (average) energy lost through conduction was applied to the atomistic region via

$$\mathbf{f}^\alpha \cdot \mathbf{v}^\alpha N \Delta t_{MD} = \mathbf{q} \Delta t_{FEM} .$$

It is interesting to note that despite the boundary condition being an energy balance it is more convenient to phrase in terms of energetic duals e.g. \mathbf{f}^α and \mathbf{v}^α . A number of difficulties were encountered: a) to solve for \mathbf{f}^α involves dividing by \mathbf{v}^α which is undefined in some cases and ill-conditioned in others b) if an implicit integration scheme is used in the atomistic region, simultaneous satisfaction of the two boundary conditions is not trivial.

7.5 Coarse-graining and fine-scale energy

One of the first tasks in designing an atom-continuum coupling scheme is extracting continuum behavior from atomistic simulation. The basic premise is that physical events occur on two scales so that the displacement, for instance, can be decomposed into the sum of a coarse and a fine scale :

$$\mathbf{u} = \bar{\mathbf{u}} + \mathbf{u}'$$

Let the characteristic length-scales be denoted ℓ_f and ℓ_c and the time-scales be τ_f and τ_c . With the exception of linear systems, the time and length-scales are coupled through a dispersion relationship, i.e. waves with high frequency will typically have short wavelengths and small group velocities. Following the notation in [12]:

SYMBOL	DEFINITION
\mathbf{d}	nodal displacements, $\dim \mathbf{d} = 3n_c$
\mathbf{q}	atomic displacements, $\dim \mathbf{q} = 3n_f$
\mathbf{N}	coarse-scale interpolants, $\mathbf{N} : \mathbb{R}^{3n_c} \mapsto \mathbb{R}^{3n_a}$
\mathbf{M}_A	atomic mass matrix $\mathbf{M}_A = \text{diag}_{\mathcal{G}_\alpha}(m_\alpha)$

where the number of spatial dimensions is assumed to be three. Note that the coarse scale interpolants can also be interpreted as mapping continuous functions onto discrete atomic displacements.

In order to coarse-grain atomistic information where the single primary unknown is a discrete set of particle trajectories, a coarse-scale mass matrix is defined as:

$$\mathbf{M} = \mathbf{N}^T \mathbf{M}_A \mathbf{N} .$$

This is a projection, which has other special properties if the interpolants are a partition of unity. In the limit of $n_c \rightarrow n_a$ with nodes located at atoms, \mathbf{M} is identical to \mathbf{M}_A . In order to get $\bar{\mathbf{u}}$ from \mathbf{u} , construct a fine-to-coarse (spatial) projection \mathbf{P} is such that

$$\mathbf{P} : \mathbb{R}^{3n_a} \mapsto \mathbb{R}^{3n_a}$$

and $\mathbf{P}\mathbf{P} = \mathbf{P}$. For instance, the L2 projection used in [12]

$$\mathbf{P} = \mathbf{N}(\mathbf{N}^T \mathbf{M}_A \mathbf{N})^{-1} \mathbf{N}^T \mathbf{M}_A$$

where typically, $\mathbf{M}_A = m\mathbf{I}$ so $\mathbf{P} = \mathbf{N}(\mathbf{N}^T \mathbf{N})^{-1} \mathbf{N}^T$. With this \mathbf{P} a fine-scale displacement can be defined

$$\mathbf{u}' = (\mathbf{I} - \mathbf{P})\mathbf{q} = \mathbf{Q}\mathbf{q}$$

where $\mathbf{Q} = \mathbf{I} - \mathbf{P}$ is the complementary projection. This implies $\mathbf{N}\mathbf{d} = \mathbf{P}\mathbf{q}$ and ultimately

$$\mathbf{d} = (\mathbf{N}^T \mathbf{M}_A \mathbf{N})^{-1} \mathbf{N}^T \mathbf{M}_A \mathbf{q} .$$

(If the interpolants used in \mathbf{N} have the Kronecker delta property, then $\mathbf{d} = \mathbf{P}\mathbf{q}$ at the nodes.) Note that it is possible, via a change of basis, to put the projection in the form: $\mathbf{P} = \sum_{I=1}^{n_c} \mathbf{e}_I \otimes \mathbf{e}_I$.

The kinetic energy for the system has the usual quadratic form

$$K = \frac{1}{2} \dot{\mathbf{u}}^T \mathbf{M}_A \dot{\mathbf{u}} = \frac{1}{2} (\mathbf{N}\dot{\mathbf{d}})^T \mathbf{M}_A (\mathbf{N}\dot{\mathbf{d}}) + \frac{1}{2} (\mathbf{Q}\dot{\mathbf{q}})^T \mathbf{M}_A (\mathbf{Q}\dot{\mathbf{q}}) + (\mathbf{N}\dot{\mathbf{d}})^T \mathbf{M}_A (\mathbf{Q}\dot{\mathbf{q}})$$

If the orthogonality condition $\mathbf{N}^T \mathbf{M}_A (\mathbf{I} - \mathbf{P}) = \mathbf{0}$ holds, then the coarse and fine-scale kinetic energies decouple $K = K_f + K_c$ and the evolution of the two scales with time is given by

$$\mathbf{M}\ddot{\mathbf{d}} = \partial_{\mathbf{d}} U = \mathbf{N}^T \partial_{\mathbf{u}} U \quad (7.37)$$

$$\mathcal{M}\ddot{\mathbf{q}} = \partial_{\mathbf{q}} U = \mathbf{Q}^T \partial_{\mathbf{u}} U \quad (7.38)$$

$$(7.39)$$

where a fine-scale mass matrix can be defined as

$$\mathcal{M} = \mathbf{Q}^T \mathbf{M}_A \mathbf{Q}$$

and U is the total potential energy or strain energy which couples the evolution of the two scales together. The ensemble average of the kinetic energy

$$\begin{aligned} \langle K \rangle &= \frac{\int \int K(\dot{\mathbf{d}}, \dot{\mathbf{q}}) \exp\left(\frac{1}{\kappa_b T} \left(\frac{1}{2} (\mathbf{N}\dot{\mathbf{d}})^T \mathbf{M}_A (\mathbf{N}\dot{\mathbf{d}}) + \frac{1}{2} (\mathbf{Q}\dot{\mathbf{q}})^T \mathbf{M}_A (\mathbf{Q}\dot{\mathbf{q}})\right)\right) d\mathbf{q} d\dot{\mathbf{q}}}{\int \int \exp\left(\frac{1}{\kappa_b T} \left(\frac{1}{2} (\mathbf{N}\dot{\mathbf{d}})^T \mathbf{M}_A (\mathbf{N}\dot{\mathbf{d}}) + \frac{1}{2} (\mathbf{Q}\dot{\mathbf{q}})^T \mathbf{M}_A (\mathbf{Q}\dot{\mathbf{q}})\right)\right) d\mathbf{q} d\dot{\mathbf{q}}} \\ &= \frac{1}{2} \dot{\mathbf{d}}^T \mathbf{M} \dot{\mathbf{d}} + \frac{1}{2} \kappa_b T \text{rank } \mathbf{Q} \end{aligned}$$

CHAPTER 7. THERMO-MECHANICAL COUPLING OF ATOMISTIC AND CONTINUUM SYSTEMS

where κ_b is Boltzmann's constant and $\text{rank } \mathbf{Q} = 3(n_a - n_c)$. So clearly the (equilibrium, kinetic) temperature T depends on the rank of the coarse scale i.e. the larger the dimensionality of the coarse scale, the larger the portion of the kinetic energy attributed to the coarse scale and the lower the temperature. There is some question whether the coarse scale is physically motivated or merely a numerical artifice. If there is a continuum limit with mesh and time window size then the split can be considered physically motivated, but for non-uniform systems this can be hard to establish.

With a coarse-scale projection in hand, a fine-scale kinetic energy for each atom can be defined as

$$\mathbf{k}_f = \frac{1}{2} \mathbf{M}_A (\mathbf{Q}\dot{\mathbf{q}})^2 ,$$

where $(\mathbf{Q}\dot{\mathbf{q}})^2$ is a vector of squares of the fine-scale velocity components, such that $K_f = \sum_{\alpha} (\mathbf{k}_f)_{\alpha}$. The projection $\mathbf{P}\mathbf{k}_f$ is interpreted as the fine-scale kinetic energy representable on the coarse grid and is related to a continuum temperature(-like) field $\Theta(\mathbf{X}, t)$ via

$$\Theta = \frac{2}{\kappa_b} \mathbf{P}\mathbf{k}_f .$$

A nodal temperature can be defined in much the same way as \mathbf{d} ,

$$\boldsymbol{\theta} = (\mathbf{N}^T \mathbf{M}_A \mathbf{N})^{-1} \mathbf{N}^T \mathbf{M}_A \Theta ,$$

through the relation $\Theta = \mathbf{N}\boldsymbol{\theta}$. Obviously, some of the kinetic energy cannot be represented on the coarse-scale grid which provides the spatial scale ℓ .

In addition to the spatial filtering, temporal coarse-graining is used in the sense of a causal (backwards-looking) time filter

$$\bar{\boldsymbol{\theta}}(t) = \int_{-\infty}^t G_{\tau}(s - t) \boldsymbol{\theta}(s) ds$$

to approximate the ensemble average. The filter kernel must be of the form $G_{\tau}(s) = \frac{1}{\tau} g(\frac{t}{\tau})$ where $g(s) \geq 0$, $\int_{-\infty}^0 g(s) ds = 1$, $g(0) = 1$ and τ is the filter width and the time scale. As in [109], two obvious choices for $G_{\tau}(s)$ are : (a) the Heaviside function $G_{\tau}(s) = \frac{1}{\tau} H(t + \tau)$ and (b) the exponential $G_{\tau}(s) = \frac{1}{\tau} \exp(\frac{t}{\tau})$ lead to the two smoothed versions of $\boldsymbol{\theta}$

$$\bar{\boldsymbol{\theta}}(t) = \frac{1}{\tau} \int_{t-\tau}^t \boldsymbol{\theta}(s) ds$$

and

$$\bar{\boldsymbol{\theta}}(t) = \frac{1}{\tau} \int_{-\infty}^t \exp(\frac{s-t}{\tau}) \boldsymbol{\theta}(s) ds$$

respectively. To avoid having to store the history of the previous configurations, Pruett et al. [109] employed the differential form of the integral equation representing the time filtering. Applying this idea to the Heaviside filter results in

$$\partial_t \bar{\boldsymbol{\theta}}(t) = \frac{1}{\tau} (\boldsymbol{\theta}(t) - \boldsymbol{\theta}(t - \tau))$$

and for the exponential filter

$$\partial_t \bar{\boldsymbol{\theta}}(t) = \frac{1}{\tau} (\boldsymbol{\theta}(t) - \bar{\boldsymbol{\theta}}(t))$$

which can easily be integrated with standard quadrature rules. Although the atoms' trajectories are continuous in time, they are integrated with a time-step which is given by a stability condition. This must be taken into account when choosing the width of the filter, τ .

With an algorithmic temperature ($\bar{\theta}$), it is possible to identify components of the total energy in the atomistic representation

$$\mathcal{H} = U + K_f + K_c$$

with those on the continuum side.

$$\mathcal{H} = \epsilon + \kappa$$

First of all, the coarse-scale kinetic energy K_f is identified with the continuum kinetic energy κ . This leaves the continuum internal energy $\epsilon = \epsilon(\partial_{\mathbf{x}} \bar{\mathbf{u}}, \bar{\theta})$ to be correlated with the potential and fine-scale kinetic energies $U + K_f$ of the atomistic domain. As noted earlier, not all of this energy is representable on the coarse-scale grid employed for the continuum simulation. Furthermore, on the continuum domain, an energy balance in a local form

$$\rho \dot{\epsilon} = \mathbf{T} \cdot \partial_{\mathbf{x}} \dot{\mathbf{x}} + \rho r - \partial_{\mathbf{x}} \cdot \mathbf{h}$$

or an integral form

$$\frac{d}{dt} \int_{\Omega} \left(\epsilon + \frac{1}{2} \dot{\mathbf{x}} \cdot \dot{\mathbf{x}} \right) \rho dv = \int_{\Omega} (\mathbf{b} \cdot \dot{\mathbf{x}} + r) \rho dv + \int_{d\Omega} \mathbf{t} \cdot \dot{\mathbf{x}} - \mathbf{q} \cdot \mathbf{n} da, \quad (7.40)$$

needs to be solve simultaneously with the momentum balance. For example, the equations of linear thermoelasticity

$$\begin{aligned} \rho \ddot{\mathbf{x}} &= \partial_{\mathbf{x}} \cdot (\mathbb{C} \partial_{\mathbf{x}} \mathbf{u} - \mathbf{M} \vartheta) \\ \frac{c}{\theta_0} \dot{\vartheta} &= \partial_{\mathbf{x}} \cdot \left(\frac{1}{\theta_0} \mathbf{K} \partial_{\mathbf{x}} \vartheta \right) - \mathbf{M} \cdot \partial_{\mathbf{x}} \dot{\mathbf{u}} \end{aligned}$$

(see [110] for computational implementation)

There are many further questions to be answered, which range from the numerical, e.g. how should the the gradients of the atomistic quantities be calculated, to the physical, e.g. what are appropriate constitutive models for the stress and heat flux? How to pass information between the two computational representations is still a work in progress.

This page intentionally left blank.

Chapter 8

Publications

The following publications have been produced as a result of the work for this project, and have either been published or are awaiting publication:

“Continuum Definitions for Stress in Atomistic Simulations”, J.A. Zimmerman, R.E. Jones, P.A. Klein, D.J. Bammann, E.B. Webb III and J.J. Hoyt, Technical Report - SAND2002-8608, December, 2002.

“Evaluation of continuum stress in atomistic simulation”, J.A. Zimmerman, E.B. Webb III, J.J. Hoyt, R.E. Jones, P.A. Klein and D.J. Bammann, **Computational Fluid and Solid Mechanics 2003**, Proceedings of the Second MIT Conference on Computational Fluid and Solid Mechanics, pp. 804-807, 2003.

“Formulation for Quasi-Static, Coupled, Atomistic-Continuum Simulation”, P.A. Klein and J.A. Zimmerman, **Multiscaling in Applied Science and Emerging Technology: Fundamentals and Applications in Mesomechanics**, Proceedings of the Sixth International Conference for Mesomechanics, pp. 514-521, 2004.

“Evaluating Thermo-Mechanical Continuum Variables in Atomistic Simulation”, J.A. Zimmerman and E.B. Webb III, **Multiscaling in Applied Science and Emerging Technology: Fundamentals and Applications in Mesomechanics**, Proceedings of the Sixth International Conference for Mesomechanics, pp. 530-537, 2004.

“Calculation of stress in atomistic simulation”, J.A. Zimmerman, E.B. Webb III, J.J. Hoyt, R.E. Jones, P.A. Klein and D.J. Bammann, *Modelling and Simulation in Materials Science and Engineering*, **12**, pp. S319-S332, 2004.

“Coupled Atomistic-Continuum Simulation using Arbitrary Overlapping Domains”, P.A. Klein and J.A. Zimmerman, In review, 2004.

CHAPTER 8. PUBLICATIONS

“Coupled Atomistic-Continuum Analysis of Nanowires and Nanofilms”, J.A. Zimmerman and P.A. Klein, To be presented at the 11th International Conference on Fracture in Turin, Italy in March of 2005.

Bibliography

- [1] P.A. Klein and J.A. Zimmerman. Formulation for quasi-static, coupled, atomistic-continuum simulation. In Multiscaling in Applied Science and Emerging Technology: Fundamentals and Applications in Mesomechanics, Proceedings of the Sixth International Conference for Mesomechanics, pages 514–521. University of Patras, 2004.
- [2] J.A. Zimmerman, R.E. Jones, P.A. Klein, D.J. Bammann, E.B. Webb III, and J.J. Hoyt. Continuum definitions for stress in atomistic simulations. Technical Report SAND2002-8608, Sandia National Laboratories, December 2002.
- [3] J.A. Zimmerman, E.B. Webb III, J.J. Hoyt, R.E. Jones, P.A. Klein, and D.J. Bammann. Evaluation of continuum stress in atomistic simulation. In Computational Fluid and Solid Mechanics 2003, volume 1 of Proceedings of the Second MIT Conference on Computational Fluid and Solid Mechanics, pages 804–807. MIT, 2003.
- [4] J.A. Zimmerman, E.B. Webb III, J.J. Hoyt, R.E. Jones, P.A. Klein, and D.J. Bammann. Calculation of stress in atomistic simulation. Modelling and Simulation in Materials Science and Engineering, 12:S319–S332, 2004.
- [5] J.A. Zimmerman and E.B. Webb III. Evaluating thermo-mechanical continuum variables in atomistic simulation. In Multiscaling in Applied Science and Emerging Technology: Fundamentals and Applications in Mesomechanics, Proceedings of the Sixth International Conference for Mesomechanics, pages 530–537. University of Patras, 2004.
- [6] T. Díaz de la Rubia and V.V. Bulatov. Materials research by means of multiscale computer simulation. Bulletin, Materials Research Society, March 2001.
- [7] Stephen Kohlhoff and Siegfried Schmauder. A new method for coupled elastic-atomistic modelling. In V. Vitek and D.J. Srolovitz, editors, Atomistic Simulation of Materials: Beyond Pair Potentials, pages 411–418. Plenum Press, New York, 1989.
- [8] S. Kohlhoff, P. Gumbsch, and H.F. Fischmeister. Crack propagation in BCC crystals studied with a combined finite-element and atomistic model. Phil. Mag. A, 64:851–78, 1991.

BIBLIOGRAPHY

- [9] E.B. Tadmor, M. Ortiz, and R. Phillips. Quasicontinuum analysis of defects in solids. Philosophical Magazine A, 73(6):1529–1563, 1996.
- [10] R.E. Rudd and J.Q. Broughton. Coarse-grained molecular dynamics and the atomic limit of finite elements. Physical Review B, 58:R5893–R5896, 1998.
- [11] J.Q. Broughton, F.F. Abraham, N. Bernstein, and E. Kaxiras. Concurrent coupling of length scales: Methodology and application. Physical Review B, 60:2391–2403, 1999.
- [12] Gregory J. Wagner and Wing Kam Liu. Coupling of atomistic and continuum simulations using a bridging scale decomposition. Journal of Computational Physics, 190:249–274, 2003.
- [13] L.E. Malvern. Introduction to the Mechanics of a Continuous Medium. John Wiley & Sons, Inc., New York, 1969.
- [14] K. Huang. On the atomic theory of elasticity. Proc. Roy. Soc. London, A203:178–94, 1950.
- [15] M. Born and K. Huang. Dynamical Theories of Crystal Lattices. Clarendon Press, Oxford, 1956.
- [16] R.E. Rudd. Coarse-grained molecular dynamics:dissipation due to internal modes. In Thin Films: Stresses and Mechanical Properties IX, volume 695 of Materials Research Society Symposium Proceedings, pages 499–504. Materials Research Society, 2002.
- [17] H.S. Park, E.G. Karpov, P.A. Klein, and W.K. Liu. The bridging scale for two-dimensional atomistic/continuum coupling. Philosophical Magazine, 2004. In review.
- [18] S.P. Xiao and T. Belytschko. A bridging domain method for coupling continua with molecular dynamics. Computer Methods in Applied Mechanics and Engineering, 193:1645–1669, 2004.
- [19] J.R. Shewchuk. An introduction to the conjugate gradient method without the agonizing pain, 1994.
- [20] W.K. Liu, Y. Chen, S. Jun, J.S. Chen, T. Belytschko, C. Pan, R.A. Uras, and C.T. Chang. Overview and applications of the reproducing kernel particle methods. Archives of Computational Methods in Engineering: State of the art reviews, 3:3–80, 1996.
- [21] W.K. Liu and Y. Chen. Reproducing kernel particle methods. International Journal for Numerical Methods in Fluids, 20:1081–1106, 1995.
- [22] B. Nayroles, G. Touzot, and P. Villon. Generalizing the finite element method: Diffuse approximation and diffuse elements. Computational Mechanics, 10:307–318, 1992.

-
- [23] Huajian Gao and Patrick Klein. Numerical simulation of crack growth in an isotropic solid with randomized internal cohesive bonds. Journal of the Mechanics and Physics of Solids, 46(2):187–218, 1998.
- [24] P. Klein and H. Gao. Crack nucleation and growth as strain localization in a virtual-bond continuum. Engineering Fracture Mechanics, 61:21–48, 1998.
- [25] T.J.R. Hughes. The Finite Element Method: Linear Static and Dynamic Finite Element Analysis. Prentice-Hall, Inc., Englewood Cliffs, New Jersey, 1987.
- [26] H. Engl, M. Hanke, and A. Neubauer. Regularization of Inverse Problems. Kluwer Academic Publishers, 1996.
- [27] Tahoe, Sandia National Laboratories: <http://tahoe.ca.sandia.gov>, 2004.
- [28] E. Hinton, T. Rock, and O.C. Zienkiewicz. A note on mass lumping and related processes in the finite element method. Earthquake Engineering and Structural Dynamics, 4:245–249, 1976.
- [29] J.E. Lennard-Jones. The determination of molecular fields I. From the variation of the viscosity of a gas with temperature. Proceedings of the Royal Society (of London), 106A:441, 1924.
- [30] J.E. Lennard-Jones. The determination of molecular fields II. From the equation of state of a gas. Proceedings of the Royal Society (of London), 106A:463, 1924.
- [31] J.M. Haile. Molecular Dynamics Simulation Elementary Methods. John Wiley & Sons, Inc., New York, 1992.
- [32] S.M. Foiles, M.I. Baskes, and M.S. Daw. Embedded-atom-method functions for the fcc metals cu, ag, au, ni, pd, pt, and their alloys. Phys. Rev. B, 33:7983–7991, 1986.
- [33] F.H. Stillinger and T.A. Weber. Computer simulation of local order in condensed phases of silicon. Physical Review B, 31:5262–5271, 1985.
- [34] R.J.E. Clausius. On a mechanical theorem applicable to heat. Philosophical Magazine, 40:122–127, 1870.
- [35] J.C. Maxwell. On reciprocal figures, frames and diagrams of forces. Transactions of the Royal Society Edinburgh, XXVI:1–43, 1870.
- [36] J.C. Maxwell. Van der waals on the continuity of the gaseous and liquid states. Nature, pages 477–480, 1874.
- [37] K.S. Cheung and S. Yip. Atomic-level stress in an inhomogeneous system. Journal of Applied Physics, 70(10):5688–5690, 1991.

BIBLIOGRAPHY

- [38] R.W. Smith and D.J. Srolovitz. Void formation during film growth: A molecular dynamics simulation study. J. Appl. Phys., 79(3):1448–1457, 1996.
- [39] S.Y. Hu, Y.L. Li, and K. Watanabe. Calculation of internal stresses around cu precipitates in the bcc fe matrix by atomic simulation. Modelling and Simulation in Materials Science and Engineering, 7:641–655, 1999.
- [40] M.F. Horstemeyer and M.I. Baskes. Atomistic finite deformation simulations: A discussion on length scale effects in relation to mechanical stresses. Journal of Engineering Materials and Technology / Transactions of the ASME, 121:114–119, 1999.
- [41] G. Marc and W.G. McMillan. The virial theorem. Advances in Chemical Physics, 58:209–361, 1985.
- [42] J.H. Irving and J.G. Kirkwood. The statistical mechanical theory of transport processes. iv. the equations of hydrodynamics. Journal of Chemical Physics, 18(6):817–829, 1950.
- [43] P. Schofield and J.R. Henderson. Statistical mechanics of inhomogeneous fluids. Proceedings of the Royal Society of London A, 379:231–240, 1982.
- [44] D.H. Tsai. The virial theorem and stress calculation in molecular dynamics. J. Chem. Phys., 70:1375–1382, 1979.
- [45] A. Machová. Stress calculations on the atomistic level. Modelling and Simulation in Materials Science and Engineering, 9:327–337, 2001.
- [46] J.S. Rowlinson and B. Widom. Molecular Theory of Capillarity. Clarendon Press, Oxford, 1989.
- [47] J.F. Lutsko. Stress and elastic constants in anisotropic solids: Molecular dynamics techniques. Journal of Applied Physics, 64(3):1152–1154, 1988.
- [48] J. Cormier, J.M. Rickman, and T.J. Delph. Stress calculation in atomistic simulations of perfect and imperfect solids. Journal of Applied Physics, 89(1):99–104, 2001.
- [49] M. Zhou. A new look at the atomic level virial stress: on continuum-molecular system equivalence. Proceedings of the Royal Society of London, Series A, 459:2347–2392, 2003.
- [50] M. Zhou. The virial stress is no stress. Physical Review B, 2003. In Review.
- [51] M. Zhou and D.L. McDowell. Equivalent continuum for dynamically deforming atomistic particle systems. Philosophical Magazine A, 82:2547–2574, 2002.
- [52] R.J. Hardy. Formulas for determining local properties in molecular-dynamics simulations: Shock waves. Journal of Chemical Physics, 76(1):622–628, 1982.

-
- [53] R.J. Hardy and A.M. Karo. Stress and energy flux in the vicinity of a shock front. In Shock Compression of Condensed Matter, Proceedings of the American Physical Society Topical Conference, pages 161–164. American Physical Society, 1990.
- [54] R.J. Hardy. Draft of a manuscript. Unpublished., 2002.
- [55] R.J. Hardy, S. Root, and D.R. Swanson. Continuum properties from molecular simulations. In 12th International Conference of the American-Physical-Society-Topical-Group on Shock Compression of Condensed Matter, volume 620, Pt. 1 of AIP Conference Proceedings, pages 363–366. American Institute of Physics, 2002.
- [56] M.P. Allen and D.J. Tildesley. Computer Simulation of Liquids. Clarendon Press, Oxford, 1987.
- [57] P. Lancaster and K. Salkauskas. Surfaces generated by moving least squares methods. Mathematics of Computation, 37:141–158, 1981.
- [58] T. Belytschko, Y.Y. Lu, and L. Gu. Element-free Galerkin methods. International Journal for Numerical Methods in Engineering, 37:229–256, 1994.
- [59] W.K. Liu and Y. Chen. Reproducing kernel particle methods. International Journal for Numerical Methods in Fluids, 20:1081–1106, 1995.
- [60] Vivek Shenoy, Vijay Shenoy, and Rob Phillips. Finite temperature quasicontinuum methods. Mat. Res. Soc. Symp. Proc., 538:465–471, 1999.
- [61] R. Kubo, M. Toda, and N. Hashitsume. Statistical Physics II: Nonequilibrium Statistical Mechanics. Springer-Verlag, New York, 1978.
- [62] D. Zubarev. Nonequilibrium Statistical Thermodynamics. Consultants Bureau, New York, 1974.
- [63] D. J. Evans and G. P. Morriss. Statistical Mechanics of Nonequilibrium liquids. Academic Press, London, 1990. Out of print. PDF version courtesy of authors at <http://rsc.anu.edu.au/~evans/evansmorrissbook.htm>.
- [64] J.-P. Hansen and I. R. McDonald. Theory of Simple Liquids. Academic Press, San Diego, 1990.
- [65] P.M. Chaikin and T.C. Lubensky. Principles of Condensed Matter Physics. Cambridge University Press, Cambridge, 1995.
- [66] D. Jou, J. Casas-Vázquez, and G. Lebon. Extended irreversible thermodynamics. Springer, Berlin, 3rd edition, 1993.

BIBLIOGRAPHY

- [67] R. Zwanzig. Memory effects in irreversible thermodynamics. Phys. Rev., 124(4):983–992, 1961.
- [68] H. Mori. Transport collective motion and brownian motion. Prog. Theor. Phys., 33:423, 1965.
- [69] G. Frenkel and M. Schwartz. The structure of Langevin’s memory kernel from Lagrangian dynamics. Europhys. Lett., 50(5):628–634, 2000.
- [70] W.C. Kerr and A.J. Graham. Generalized phase space version of Langevin equations and associated Fokker-Planck equations. Eur. Phys. J. B, 15:305–311, 2000.
- [71] M. Grant and R. C. Desai. Generalized Langevin theory for inhomogeneous fluids: the equations of motion. Phys. Rev. A., 25(5):2727–2743, 1982.
- [72] M. G. McPhie, P. J. Daivis, I. K. Snook, J. Ennis, and D. J. Evans. Generalized Langevin equation for nonequilibrium systems. Physica A, 299:412–426, 2001.
- [73] Joan-Emma Shea and Irwin Oppenheim. Fokker-Planck equation and Langevin equation for one Brownian particle in a nonequilibrium bath. J. Phys. Chem., 100:19035–19042, 1996.
- [74] R. Biswas and D. R. Hamann. Simulated annealing of silicon atom clusters in Langevin molecular dynamics. Phys. Rev. B, 34(2):895–901, 1986. And references therein.
- [75] G. Zhang and T. Schlick. The Langevin implicit-Euler/normal-mode scheme for molecular dynamics at large time steps. J. Chem. Phys., 101(6):4995–5012, 1994.
- [76] Eirik G. Flekkoy 1 and Peter V. Coveney. From molecular dynamics to dissipative particle dynamics. Phys. Rev. Lett., 83(9):1775–1778, 1999.
- [77] S. Reich. Smoothed Langevin dynamics of highly oscillatory systems. Physica D, 138:210–224, 2000.
- [78] P. C. Martin, O. Parodi, and P. S. Pershan. Unified hydrodynamic theory for crystals, liquid crystals, and normal fluids. Phys. Rev. A., 6(6):2401–2420, 1972.
- [79] J. H. Irving and J. G. Kirkwood. The statistical mechanical theory of transport processes. IV. the equations of hydrodynamics. J. Chem. Phys., 18(6):817–829, 1950.
- [80] J.L. Lebowitz, J. K. Percus, and L. Verlet. Ensemble dependence of fluctuations with application to machine computations. Phys. Rev., 153(1):250–254, 1967.
- [81] Andraás Baranyai and Peter T. Cummings. Fluctuations close to equilibrium. Phys. Rev. E, 52(3):2198–2203, 1995.
- [82] C. Truesdell. Rational Thermodynamics. Springer, New York, 2nd edition, 1984.

- [83] H. Mori. Statistical mechanical theory of transport in fluids. Phys. Rev., 112(6):1829–1842, 1958.
- [84] H. Mori. Correlation function method for transport phenomena. Phys. Rev., 115(2):298–300, 1959.
- [85] Werner Loose and Giovanni Ciccotti. Temperature and temperature control in nonequilibrium-molecular-dynamics simulations of the shear flow of dense liquids. Phys. Rev. A., 45(6):3859–3866, 1992.
- [86] K. Aoki and D. Kusnezov. Non-equilibrium steady states and transport in the classical lattice ϕ^4 theory. Phys. Lett. B, 477:348–354, 2000.
- [87] K. Aoki and D. Kusnezov. Violations of local equilibrium and linear response in classical lattice systems. Phys. Lett. A, 309(5-6):377–381, 2003.
- [88] K. Aoki and D. Kusnezov. On the violations of local equilibrium and linear response. arXiv:nlin.CD/0105063 v1, 2001.
- [89] D. Jou, J. Casas-Vázquez, and G Lebon. Extended irreversible thermodynamics. Rep. Prog. Phys., 51:1105–1179, 1988.
- [90] J. Casas-Vázquez and D. Jou. Nonequilibrium temperature versus local-equilibrium temperature. Phys. Rev. E, 49(2):1040–1048, 1994.
- [91] Byung Chan Eu and L. S. Garcia-Colín. Irreversible processes and temperature. PRE, 54(3):2501–2512, 1996.
- [92] V. A. Golovko. A thermodynamically self-consistent statistical theory of the crystalline state. Physica A, 300:195–224, 2001.
- [93] R. A. Guyer and J. A. Krumhansl. Solution of the linearized phonon Boltzmann equation. Phys. Rev., 148(2):766–778, 1966.
- [94] J. Camacho. Third law of thermodynamics in the presence of a heat flux. Phys. Rev. E, 51(1):220–225, 1995.
- [95] Reese Jones. Models of heat transfer. Internal Document, 2003.
- [96] Harold S. Park, Eduard G. Karpov, and Wing Kam Liu. A temperature equation for coupled atomistic/continuum simulations. Comput. Meth. Appl. Mech. Engrg., 193:1713–1732, 2004.
- [97] D.D. Joseph and L. Preziosi. Heat waves. Rev. Modern Physics, 61(1):41–73, 1989.
- [98] A. Majumdar. Microscale energy transport in solids., pages 3–94. Taylor and Francis, Washington, D.C., 1998.

BIBLIOGRAPHY

- [99] A.A. Joshi and A. Majumdar. Transient ballistic and diffusive phonon heat transport in thin films. Journal of Applied Physics, 74(1), 1993.
- [100] G. Chen. Ballistic-diffusive equations for transient heat conduction from nano to macroscales. Transactions of the ASME - Journal of Heat Transfer, 124:320–328, 2002.
- [101] M.E. Gurtin and A.C. Pipkin. A general theory of heat conduction with finite wave speeds. Arch. Ration. Mech. Anal., 31:113, 1968.
- [102] S. Root, R.J. Hardy, and D.R. Swanson. Continuum predictions from molecular dynamics simulations: Shock waves. Journal of Chemical Physics, 118(7):3161–3165, 2003.
- [103] J. Casas-Vázquez and D. Jou. Nonequilibrium temperature versus local-equilibrium temperature. Physical Review E, 49(2):1040–1049, 1994.
- [104] C.F. Richardson and P. Clancy. Contribution of thermal conductivity to the crystal-regrowth velocity of embedded-atom-method-modeled metals and their alloys. Physical Review B, 45(21):12260–12268, 1992.
- [105] P. Heino and E. Ristolainen. Thermal conduction at the nanoscale in some metals by md. Microelectronics Journal, 34:773–777, 2003.
- [106] T. Ikeshoji and B. Hafskjold. Non-equilibrium molecular dynamics calculation of heat conduction in liquid and through liquid-gas interface. Molecular Physics, 81(2):251–261, 1994.
- [107] J.R. Lukes, D.Y. Li, X.-G. Liang, and C.-L. Tien. Molecular dynamics study of solid thin-film conductivity. Transactions of the ASME - Journal of Heat Transfer, 122:536–543, 2000.
- [108] R. Livi and S. Lepri. Heat in one dimension. Nature, 421:327, 2003.
- [109] C.D. Pruett, T.B. Gatski, C.E. Grosch, and W.D. Thacker. The temporally filtered Navier-Stokes equations: Properties of the residual stress. Physics of Fluids, 15(8):2127–2140, 2003.
- [110] F. Armero and J.C. Simo. A new unconditionally stable fractional step method for nonlinear coupled thermomechanical problems. International Journal for Numerical Methods in Engineering, 35(4):737–766, 1992.

Chapter 9

DISTRIBUTION:

1	MS 0123	D.L. Chavez, 1011
1	MS 0310	J.B. Aidun, 9235
1		P.S. Crozier, 9235
1		C.D. Lorenz, 9235
1		M.G. Martin, 9235
1		P.A. Schultz, 9235
1		A. Slepoy, 9235
1		A.P. Thompson, 9235
1	MS 0384	H.S. Morgan, 9140
1	MS 0825	C.W. Peterson, 9100
1	MS 0825	W.L. Hermina, 9110
1	MS 0839	P.J. Ballou, 9103
1	MS 0893	J. Pott, 9123
1		P.M. Chaplya, 9123
1		J.V. Cox, 9123
1		D.C. Hammerand, 9123
1		E.D. Reedy, 9123
1		W.M. Scherzinger, 9123
1	MS 1110	A.E. Mattsson, 9235

CHAPTER 9. DISTRIBUTION

1	MS 1110	S.J. Plimpton, 9212
1		L.J.D. Frink, 9212
1	MS 1411	H.E. Fang, 1834
1		C.C. Battaile, 1834
1		M.V. Braginsky, 1834
1		S.M. Foiles, 1834
1		E.A. Holm, 1834
10		J.J. Hoyt, 1834
1		M.J. Stevens, 1834
10		E.B. Webb III, 1834
1	MS 1415	J.E. Houston, 1114
1	MS 9001	M.E. John, 8000
		Attn:
		R.H. Stulen, 8100, MS 9004
		D.R. Henson, 8200, MS 9007
		W.J. McLean, 8300, MS 9054
		K.E. Washington, 8900, MS 9003
1	MS 9014	D.M. Kwon, 8242
1	MS 9042	P.A. Spence, 8774
1		M.L. Chiesa, 8774
1		Y. Ohashi, 8774
10	MS 9042	G.J. Wagner, 8752
1	MS 9108	R.D. Monson, 8243
1		S.L. Robinson, 8243
1		G.C. Story, 8243
1	MS 9161	E.P. Chen, 8763
10		C.J. Kimmer, 8763
10		P.A. Klein, 8763
1		T.D. Nguyen, 8763
1		H.S. Park, 8763
30		J.A. Zimmerman, 8763
1	MS 9161	D.L. Medlin, 8761
1		N.C. Bartelt, 8761

1		J.C. Hamilton, 8761
1		F. Leonard, 8761
1		E. Marquis, 8761
1		K.F. McCarty, 8761
1		D.J. Siegal, 8761
1		R.R. Stumpf, 8761
1	MS 9161	W.R. Even Jr., 8760
1	MS 9402	D.F. Cowgill, 8772
1		D.K. Balch, 8772
1		R. Causey, 8772
1		K.L. Hertz, 8772
1		B.P. Somerday, 8772
1	MS 9403	T.J. Shepodd, 8762
1	MS 9405	J.M. Hruby, 8700
		Attn:
		G.D. Kubiak, 8750, MS 9404
		J.E.M. Goldsmith, 8751, MS 9401
		C.D. Moen, 8752, MS 9042
		G.F. Cardinale, 8753, MS 9401
		J.R. Garcia, 8754, MS 9409
		C.H. Cadden, 8772, MS 9402
		J.C.F. Wang, 8773, MS 9403
1	MS 9405	K.L. Wilson, 8770
10	MS 9405	S. Aubry, 8763
10		D.J. Bammann, 8763
1		A.A. Brown, 8763
1		G.R. Feijoo, 8763
1		J.W. Foulk, 8763
1		D.A. Hughes, 8763
10		R.E. Jones, 8763
1		E.B. Marin, 8763
1		R.A. Regueiro, 8763
2	MS 0899	Technical Library, 9616
1	MS 9018	Central Technical Files, 8945-1
1	MS 9021	Classification Office, 8511